Evaluation and Analysis of Commercially Available Electrochemical Carbon Monoxide Sensors for Aircraft Applications

by

John Richard Andress

A thesis submitted to the Graduate Faculty of
Auburn University
in partial fulfillment of the
requirements for the Degree of
Master of Science

Auburn, Alabama
August 4, 2012

Keywords: airline cabin environment research (ACER), fume event, carbon monoxide sensor, air quality, cabin pressure

Approved by

Ruel A. Overfelt, Chair, Professor of Materials Engineering
Jeffrey Fergus, Professor of Materials Engineering
Bart Prorok, Professor of Materials Engineering

Abstract

Commercial airline flight in the United States of America is under the oversight of the Federal Aviation Administration (FAA) which has set standards for the amount of harmful or unpleasant compounds onboard aircraft to improve occupant safety and comfort. Carbon monoxide (CO), one of these regulated compounds, is of particular interest to the FAA in addition to sensors that are able to properly detect CO inside the airline cabin. In this study, a total of ten commercially available CO sensors were tested and evaluated. The sensors were operated in an environmentally sealed chamber where the total pressure and CO gas concentration were controlled. The sensors were primarily tested in known concentrations of CO in nitrogen, while additional experiments were performed to study the effect of oxygen (O_2) on the sensors. The sensors' steady state and transient responses were analyzed. The repeatability of the sensors' measurements was also investigated with and without O_2.

Acknowledgments

I would like to express my deepest gratitude to Dr. Ruel A. Overfelt for his support and encouragement throughout my collegiate career. Under his leadership I have learned, developed and applied engineering principles that will be invaluable throughout my professional career. His patience and guidance were crucial in my technical training for which I am very grateful. I would also like to thank Dr. Jeffrey Fergus and Dr. Bart Prorok for serving on my committee. Their guidance and insight were paramount in this research project and allowed me to learn more through its completion.

I would also like to acknowledge my fellow colleagues for their collaboration with me and for their friendship. I would like to thank Lance Haney for his patience and understanding as he taught me about infrared spectroscopy, and Amanda Neer for always being willing to discuss and critique my ideas throughout this project. I extend my sincere gratitude to Naved Siddiqui for his efforts in assisting with the completion of the experimentation in this study, and Wil Kilpatrick for providing me with a better understanding of the chemistry involved in this project. I would also like to thank L.C. Mathison for his invaluable technical expertise and support throughout this project. In addition, I would like to thank Mike Crumpler, Shawn Yang, Briana McCall, Amy Baldwin, Chan Kang and Hassan Sk for their thoughts and assistance in the completion of this research effort.

Most importantly, I would like to thank my wonderful wife, Katie, for her unwavering love and encouragement of me as I pursued my degree. Without her constant love and understanding I would not have been able to complete this research project. The support of our family, parents and grandparents was very encouraging, as well.

Finally, this project was funded by the U.S. Federal Aviation Administration (FAA) Office of Aerospace Medicine through the National Air Transportation Center of Excellence for Research in the Intermodal Transport Environment (RITE), Cooperative Agreement 07-C-RITE-AU. Although the FAA has sponsored this project, it neither endorses nor rejects the findings of this research.

Table of Contents

List of Tables

List of Figures

Nomenclature

ACER	Airline Cabin Environment Research
ACI	Automation Components, Inc.
APU	Auxiliary Power Unit
°C	Degrees Centigrade
CFM	Cubic Feet per Minute
COHb	Carboxyhemoglobin
CO	Carbon Monoxide
CO_2	Carbon Dioxide
Cs	Carbon Monoxide Test Gas Source Concentration
DTGS	Deuterated Triglycine Sulfate
°F	Degrees Fahrenheit
FAA	Federal Aviation Administration
FT	Feet
FTIR	Fourier Transform Infrared Spectrometer/Spectroscopy
H_2O	Water or Water Vapor
Hb	Hemoglobin
HEPA	High Efficiency Particulate Air
IR	Infrared
K	Kelvin

kPa	Kilopascal
MFC	Mass Flow Controller(s)
MOS	Metal Oxide Semiconductor
MPa	Megapascal
N_2	Nitrogen
O_2	Oxygen
O_3	Ozone
PPM	Parts per Million
PSI	Pound per Square Inch
σ	Standard Deviation
SCCM	Standard Cubic Centimeter per Minute
SLE	Sea Level Equivalent
SnO_2	Tin Oxide
STP	Standard Temperature and Pressure
T	Time Constant
USA	United States of America
VOC	Volatile Organic Compound(s)

Chapter 1: Introduction

Commercial air travel has become a way of life for many people in the United States of America (USA). In fact, there were over 630 million passenger enplanements on domestic, commercial airline flights in 2011 [1]. This number is expected to grow resulting in one billion commercial passenger enplanements combined from both domestic and international flights by 2023 according to a Federal Aviation Administration (FAA) forecast model [2]. With so many passengers and crew members flying in the USA and abroad, it is important to evaluate and understand any health and safety risks associated with commercial airline flight.

One potential risk, poor aircraft air quality, has gained a large amount of interest in recent years from the pilot and flight attendant unions, the FAA and the flying public. Commercial airliners supply cabin air from the compression stages of the aircraft engine and, in addition, the air treatment and ventilation systems have been well designed to supply clean, healthy air to the cabin occupants. However, there are rare, but documented cases, called fume events, of unclean air entering the commercial airline cabin [3–6]. Fume events are characterized by any of the following phenomena: a reduction of the visibility inside the cabin, foul or unusual odors inside the cabin, and occupant physiological symptoms such as drowsiness, headache and nausea. In a few isolated cases, this unclean air is attributed by some to be the cause of certain illnesses contracted by passengers and crew.

Because these fume events are so rare it is unknown exactly what compounds are present in the contaminated air as well as the source of the contamination. However, it is suspected that the unclean air enters the cabin via the bleed air system and is the result of the burning of certain aircraft working fluids such as de-icing fluid, hydraulic fluid, jet fuel or jet engine lubricants (oils). As a result, possible air contaminants inside the airline cabin include carbon monoxide (CO), ozone (O_3), carbon dioxide (CO_2), unburned hydrocarbons and tricresyl phosphate (TCP) which is an anti-wear additive used in aircraft engine oil [7, 8].

CO has been identified in this study as the contaminant of interest. CO is an odorless, tasteless and colorless gas that is a byproduct of incomplete combustion and is well known to be hazardous to human health. Typical physiological symptoms of CO poisoning include nausea, headache, vomiting, loss of consciousness and even death if the person is not removed from the CO environment [9]. In light of these serious health concerns, it is important to be able to properly identify the presence of CO in the airline cabin.

One possible solution is to use existing, commercially available CO sensors to detect the presence of CO inside the airline cabin. These CO sensors are inexpensive and readily available which makes them attractive for integration into an aircraft sensor package. Most of these sensors, however, were developed and designed to operate in a home or office building where the environmental conditions are predictable and stable. However, the airline cabin environment is quite different from these environments with variations in the ambient air temperature, relative humidity and the total pressure. In light of this, the performance of the commercially available CO sensors must be

evaluated in these conditions in order that proper judgments can be made concerning their efficacy in the airline cabin.

This study was performed in an effort to advance the understanding of commercially available CO sensors' performance in environmental conditions representative of the aircraft cabin. This study will add to the growing amount of information concerning the efficacy of commercially available sensors to monitor the air quality in a reduced pressure environment such as might be encountered onboard an aircraft. A total of ten commercially available, electrochemical CO sensors from eight different manufacturers were tested and evaluated in this study. The sensors were operated in an environmentally sealed chamber where the total pressure and CO gas concentration were controlled. The CO gas concentration was supplied by purchased, premixed tanks of gas. The sensors were primarily evaluated in a gas mixture of a known CO gas concentration in nitrogen (N_2) to study the effects of an oxygen (O_2) free environment on the sensors; however, some testing was accomplished with O_2 added to this gas mixture for the sake of comparison. The concentration of the CO inside the sensor evaluation chamber was monitored by a Perkin-Elmer Spectrum GX Fourier Transform Infrared spectrometer (FTIR).

Chapter 2: Literature Review

Commercial Aircraft Systems and Environment Overview

One of the main goals of this research is to determine a method by which CO levels can be properly measured inside a commercial airliner. When detecting a gas of any kind, it is important to be familiar with the environment in which the gas is to be detected and quantifiably measured, therefore, the airline cabin environment becomes of significant interest.

The airline cabin is a dynamic environment which changes during the various stages of flight and ground operations. The FAA has regulatory standards which set the maximum allowable amounts of harmful or unpleasant compounds onboard the aircraft, however, there is no regulation that requires sensors be placed onboard to ensure that the regulations are met [10]. The equipment and systems onboard the aircraft have been carefully designed to control this environment to the fullest extent and to be able to meet the FAA standards. Knowledge of the role and operation of these systems is important for understanding the environment in which sensors could operate and is also important for designing and building an experimental setup that can adequately reproduce the needed aspects of this environment.

Bleed Air System

All of the breathable air onboard most commercial aircraft comes from the bleed air system. The one exception is the Boeing 787 Dreamliner which uses electrical compressors instead of the jet engines to pressurize the cabin and operate the environmental control system (ECS) [11]. In addition to breathable air, the bleed system also provides air at the proper temperature and pressure necessary to pressurize the airline cabin and to meet all of the requirements of the pneumatic systems onboard the aircraft [12]. The bleed system, as shown in Figure 2.1, starts by extracting pressurized air from the compression stages of the turbofan engine. This air typically comes from one of two bleed ports. The first is the low pressure port (~eighth compressor stage) where the air has a temperature of approximately 204 °C (400 °F) and a pressure of more than 207 kPa (32 psi) [12]. The second is the high pressure port (~fifteenth compressor stage) and commonly has an air temperature of 650 °C (1200 °F) and a pressure of 2.96 MPa (430 psi) [12]. The bleed system automatically selects which port to draw air based on the needs of the aircraft systems at any given time. In fact, the bleed air system is completely automatic except for a shutoff switch available to the pilots [12].

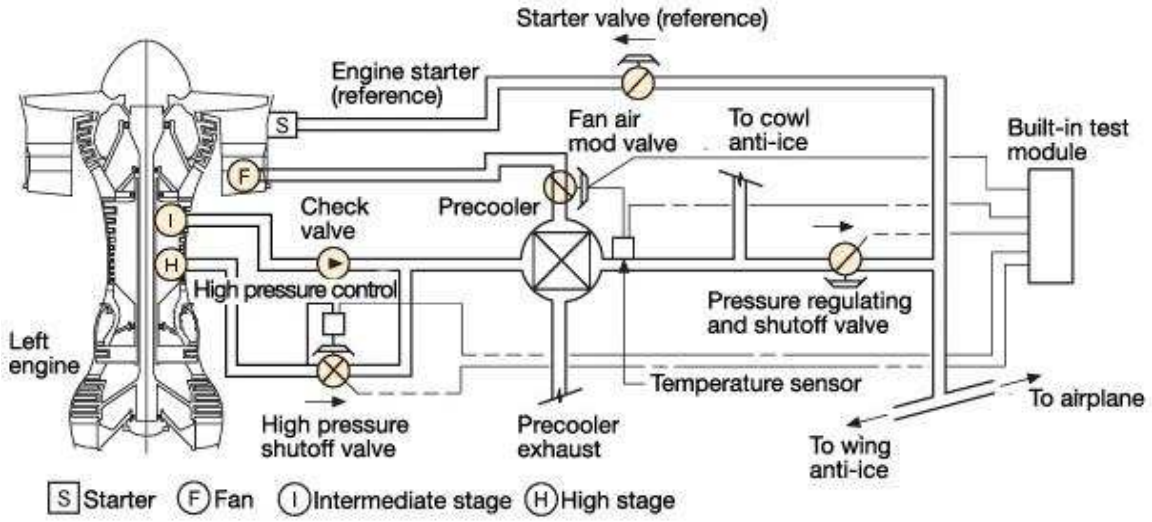

Figure 2.1: Schematic of the bleed air system commonly found in commercial aircraft [12].

Once the air leaves the bleed system it is then treated to remove O_3 by an ozone converter. The ozone converter, shown in Figure 2.2, directs the air through a honeycomb core containing a noble metal catalyst such as palladium where the O_3 dissociates into O_2. Thus, the O_3 is converted into O_2 which results in the concentration of O_3 in the air stream being reduced.

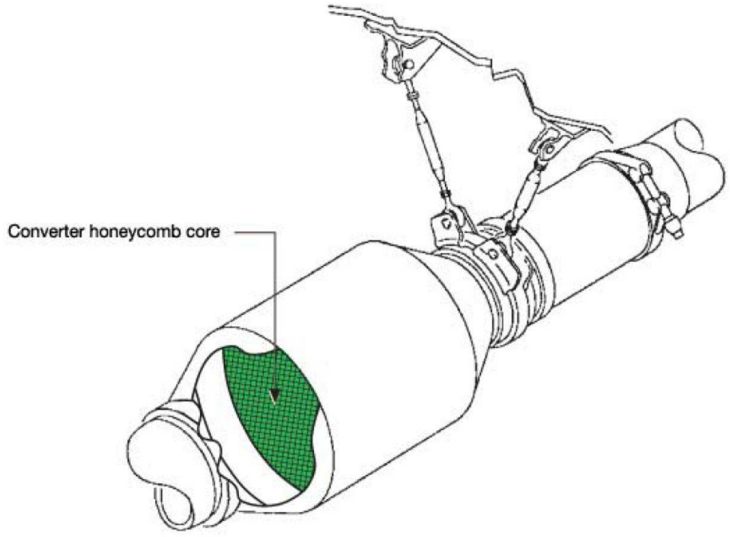

Figure 2.2: Ozone converter showing honeycomb core [12].

After the air leaves the ozone converter it is then cooled using air conditioner packs to 16 °C (60 °F) while the pressure is reduced to 81 kPa (11.8 psi) [12]. This air, which is now at the proper temperature and pressure to enter the aircraft cabin, is then mixed in the mixing manifold with a similar amount of recirculated air from the aircraft cabin [12, 13]. Therefore, the air inside the mixing manifold that eventually enters the airline cabin is typically 50% fresh air, as provided by the bleed air system, and 50% recirculated air from the aircraft cabin.

Generally for wide body aircraft, the air that is recirculated from inside the cabin is filtered with a HEPA-type filter which is in contrast to single isle aircraft which do not have a HEPA-type filtration system. This HEPA filtration system is similar to those used in critical wards of hospitals which removes 99.9% of all bacteria and viruses [12, 13]. Additionally, the HEPA-type filters remove any particle from the air which is 0.003 micrometers or larger [13]. However, HEPA-type filters do not remove gasses

such as CO, volatile organic compounds (VOC) or excess CO_2. During normal operation the amounts of these contaminants are assumed to be kept below FAA regulatory standards, which are shown in Table 2.1, by dilution of the cabin air with large amounts of air from outside the aircraft. The output flow rate of the recirculation system is approximately 20 cubic feet per minute (cfm) per person (10 cfm recirculated air and 10 cfm outside/fresh air) which results in the air inside the cabin being completely exchanged 10 to 15 times every hour [12, 14]. By comparison the number of outside air changes onboard an aircraft is higher than that of sensitive areas in a hospital or a typical building as shown in Figure 2.3 [13].

Table 2.1
FAA and EPA Regulatory Standards for Air Quality [15]

Pollutant	Ambient Standard	Agency	Aircraft Standard	Agency
Ozone	0.12 ppm 1 –hr 0.08 ppm 8-hr	EPA NAAQS	0.1 ppm (sea level equivalent, time weighed average over 3-hr at >27,000 ft altitude) 0.25 ppm (sea level equivalent, at any time >32,000 ft altitude)	FAA(14 CFR 25.832)
Carbon monoxide	35 ppm 1-hr 9 ppm 8-hr	EPA NAAQS	50 ppm	FAA(14 CFR 25.831)
PM_{10}	150 $\mu g/m^3$ 24-hr	EPA NAAQS	None established	
$PM_{2.5}$	65 $\mu g/m^3$ 24-hr	EPA NAAQS	None established	
Nitrogen dioxide	0.05 ppm annual	EPA NAAQS	None established	
CO_2	None		5,000 ppm (sea level equivalent)	FAA (14 CFR 25.831)

ppm = parts per million by volume
PM_{10} = particulate matter less than 10 microns in diameter
$PM_{2.5}$ = particulate matter less than 2.5 microns in diameter
$\mu g/m^3$ = microgram per cubic meter

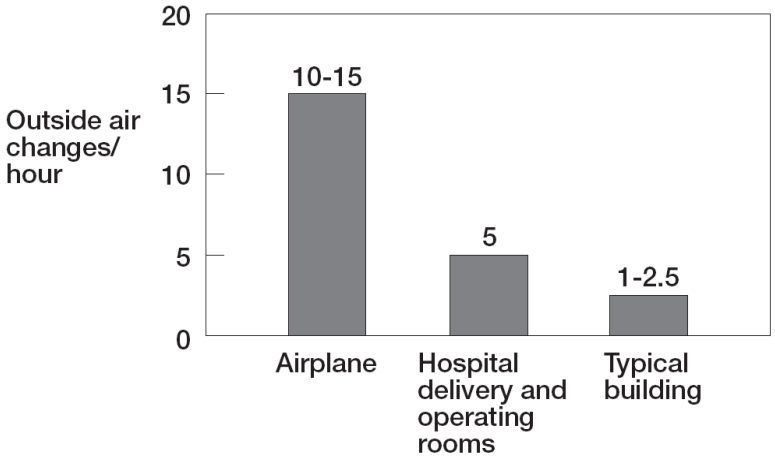

Figure 2.3: Comparison of the number of outside air changes per hour in different environments [13].

From the mixing manifold and the recirculation system the air is then distributed to the passengers via the ventilation system. The ventilation system, as shown in Figure 2.4, supplies air from the top of the cabin through an overhead air distribution system that extends the entire length of the aircraft cabin [12]. Typically, this air is approximately 20 to 30 °C (68 to 86 °F) [12, 14] with a relative humidity range of approximately 10 to 20% [12, 16]. Once the air leaves the overhead air distribution system the air flows generally downward, as shown in Figure 2.4, and is designed so that air that enters at a particular seat row will also exit the cabin at approximately that same seat row [12]. This minimizes fore and aft drafts which improves passenger comfort and minimizes the propagation of passenger borne contaminants should they become airborne [12]. The air is removed from the cabin by vents in the sidewalls that run along the entire length of the floor of the cabin. Once the air leaves the cabin, 50% is exhausted to the outside of the aircraft and 50% is retained and recirculated.

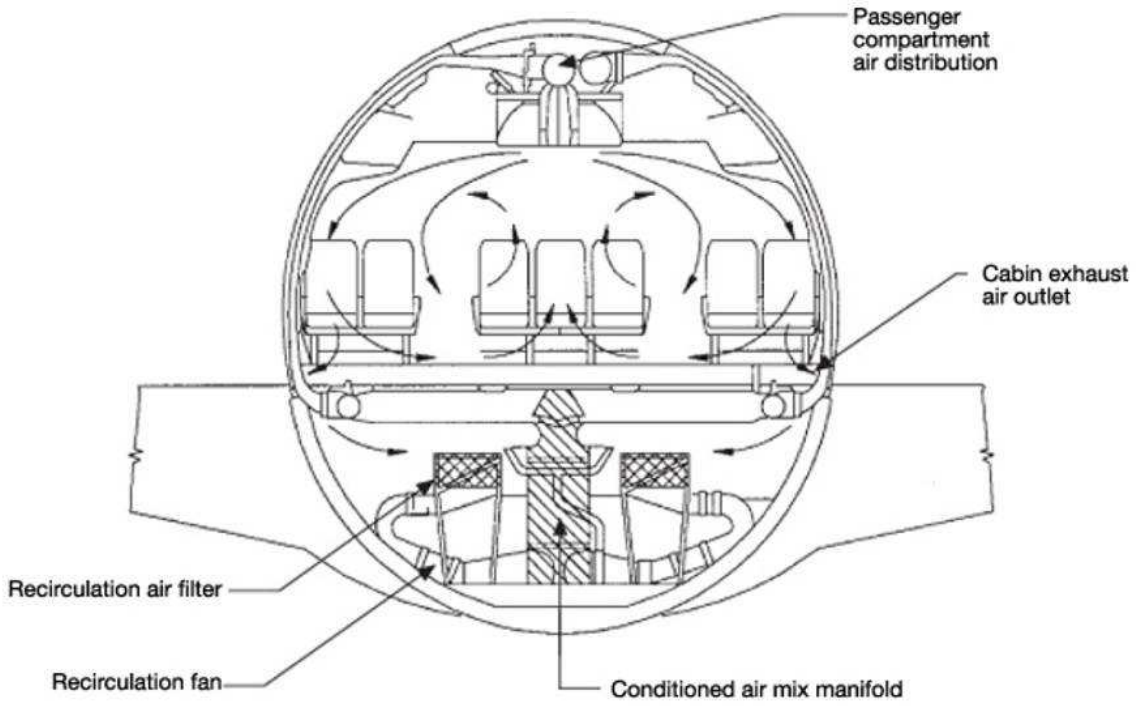

Figure 2.4: Diagram showing air flow inside the aircraft cabin. Air enters the cabin from the center of the ceiling and is exhausted near the floor by vents in the sidewall [12].

One of the aspects that set the commercial airline cabin environment apart from other environments is the variation in pressure. The pressure in most residences and office buildings is relatively constant with a value close to atmospheric pressure. Inside the aircraft cabin, however, the pressure varies in different stages of flight. The level to which the cabin can be pressurized is limited by that fact that the cabin-to-outside pressure difference cannot exceed 59.3 kPa (0.585 atm) [12]. Therefore, as the altitude of the aircraft changes, the cabin air pressure will change as well, as is shown in Figure 2.5. Typically, commercial aircraft have a cruising altitude of 35,000 to 39,000 ft (23.8 to

19.6 kPa) which means that the cabin is pressurized to approximately 5,400 to 7,000 feet altitude equivalent (83.1 to 78.2 kPa) [12, 13].

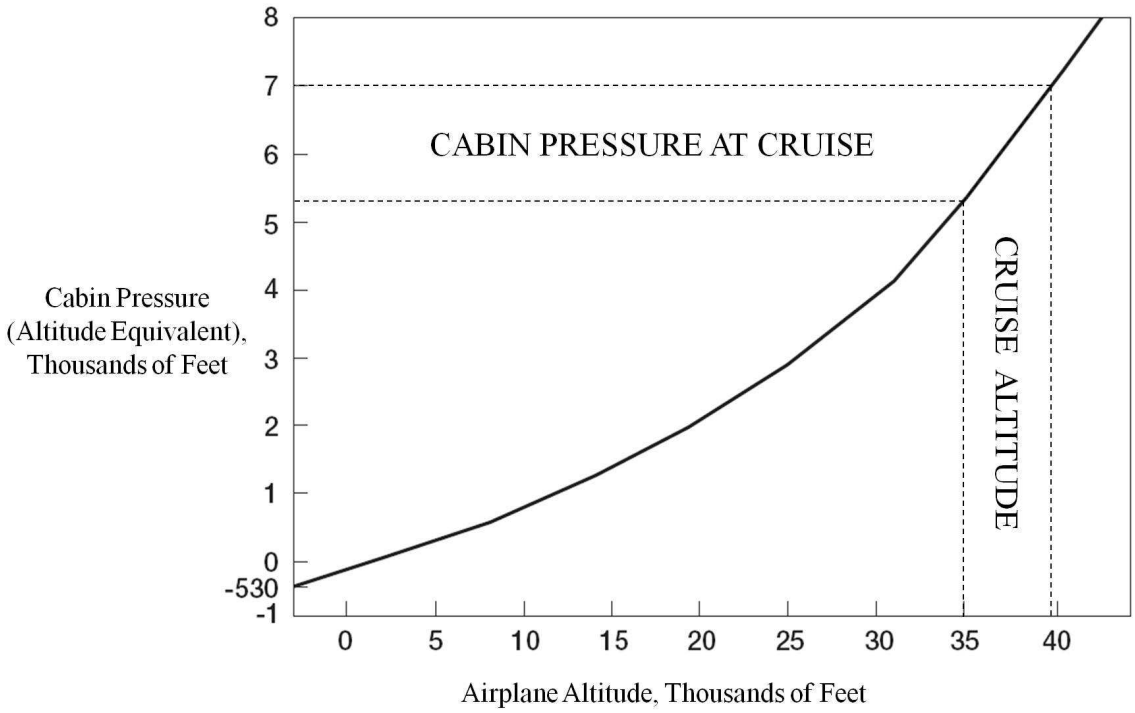

Figure 2.5: Cabin Pressure (Altitude Equivalent) versus Aircraft Altitude [13].

The total pressure inside the cabin can be related to the partial pressures of each gas species present inside the cabin by Dalton's Law of Partial Pressures which is given in Equation 2.1.

$$P_T = \sum_{i=1}^{n} p_i$$
$$p_i = X_i \; P_T \tag{2.1}$$

where:

p_i = Partial pressure of the i-th gas mixture component (kPa)
X_i = Mole fraction of the i-th gas mixture component (Unit-less)
P_T = Total pressure of the gas mixture (kPa)
n = number of components in the gas mixture

According to Dalton's Law, in a gas mixture, for a given mole fraction of a specific gas, X_i, as the total pressure, P_T, decreases the partial pressure of the specific gas, p_i, also decreases. The CO sensors (electrochemical) used in this study are dependent on the partial pressure of CO present at the time of the measurement. This is a potentially important factor in consideration of 14 CFR 25.831 which only states that 50 ppm CO must not be exceeded inside the aircraft cabin while leaving the detection method up to the user [10]. If the operator and designer of the sensor do not adjust the sensor's output based on the total pressure present when the measurement was made, then passengers and crew could potentially be exposed to CO levels higher than the required 50 ppm CO before the sensor alarms.

Fume Event

A large amount of effort is involved both in the design of the aircraft ventilation system and in its maintenance to ensure that the air onboard a commercial aircraft is safe to breathe. Occasionally, the bleed air system or the auxiliary power unit (APU) malfunctions or is improperly maintained, resulting in the presence of foul odors and smoke inside the airline cabin [15, 17–22]. The presence of foul odors and/or smoke in the aircraft cabin is called a fume event or an exposure event.

Although rare, fume events potentially contain harmful and toxic components from the pyrolized aircraft engine oil which is believed to be the source of the odor and smoke [23, 24]. It has been suggested that exposure to the contaminated air of a fume event is the primary cause of short-term and chronic illness, and, as a result, fume events have gained the attention of both pilot and flight attendant unions and the FAA [25–27].

Effects of Carbon Monoxide on Humans

CO is an odorless, tasteless and colorless gas that is harmful to human health. It is unclear exactly how many CO related deaths there are every year but some estimate that nearly one-half of the fatal poisonings in industrialized countries is the result of CO poisoning [28, 29]. Additionally, jet engine oils and other aircraft working fluids commonly used in the airline industry are known to contain harmful chemicals [30, 31] that when burned or pyrolized can create significant amounts of CO and CO_2 [7, 32, 33]. These facts underline the importance of understanding the effect of CO on the human body, especially when considering the fact that the engine oil and humans are in close proximity onboard aircraft.

When CO is breathed into the lungs it is easily absorbed into the bloodstream where it attaches with hemoglobin (Hb) to form carboxyhemoglobin (COHb). This has two effects: First, Hb has four sites where O_2 can bind with it. CO also binds to these same Hb sites, which reduces the number of O_2 binding sites, thus decreasing the amount of O_2 that the blood can carry [28]. Second, CO binds very strongly with Hb due to its high affinity to Hb, and, in fact, the affinity of COHb is 240 times higher than that of O_2 [28, 29, 34]. In addition, when CO is bound to at least one of the four O_2 binding sites

of Hb, the affinity of O_2 to the altered Hb complex is increased. This results in Hb being unable to release the O_2 when it comes time to deliver it to the bodily tissues [28]. Thus, COHb affects Hb's capacity to carry O_2 and to deliver O_2 to the body. The higher the percentage of COHb in the blood, the less O_2 is supplied to the body's tissues, resulting in hypoxia which leads to neurobehavioral and cardiovascular symptoms [29, 34, 35].

CO poisoning, which results from COHb saturation in the blood of 10 to 30%, includes the following symptoms: headache, dizziness, weakness, nausea, vomiting, confusion, disorientation and visual disturbances [29, 34]. In more severe cases with COHb blood saturation of 30 to 50% and above, symptoms include shortness of breath, increases in pulse and respiratory rates, loss of conscience, and eventually permanent brain damage, heart attack and death [9, 34, 35]. However, CO poisoning and the accompanying symptoms do not occur instantaneously in a person whom is exposed to CO. It takes time for COHb to form and to reach toxic levels inside the human body. Logic follows that the higher the CO concentration, the faster the COHb percentage in the blood will increase, making the duration of exposure a key factor in CO poisoning [34]. Figure 2.6 shows how long a person must be exposed to a given, constant CO concentration before the indicated COHb blood saturations are reached. These COHb blood saturation levels correspond to certain adverse physiological symptoms. Selected CO concentration data from Figure 2.6 is also tabulated in Table 2.2 in order to aid the analysis of CO poisoning. As can be seen from Figure 2.6 and Table 2.2, a person exposed to 50 ppm CO for four hours or less will not experience any noticeable symptoms of CO poisoning due to the fact that COHb levels will be between 0 to 10% [9]. COHb levels in this range do not usually produce noticeable, medical

symptoms [34]; in fact, current research suggests that COHb levels of 15 to 20% must be reached before a 10% reduction in behavioral or visual impairment can be measured [35]. On the other hand, for a constant exposure to 800 ppm CO, a person will experience a headache after 10 to 15 min, nausea and drowsiness after 20 to 30 min and unconsciousness and death after 30 to 45 min [9].

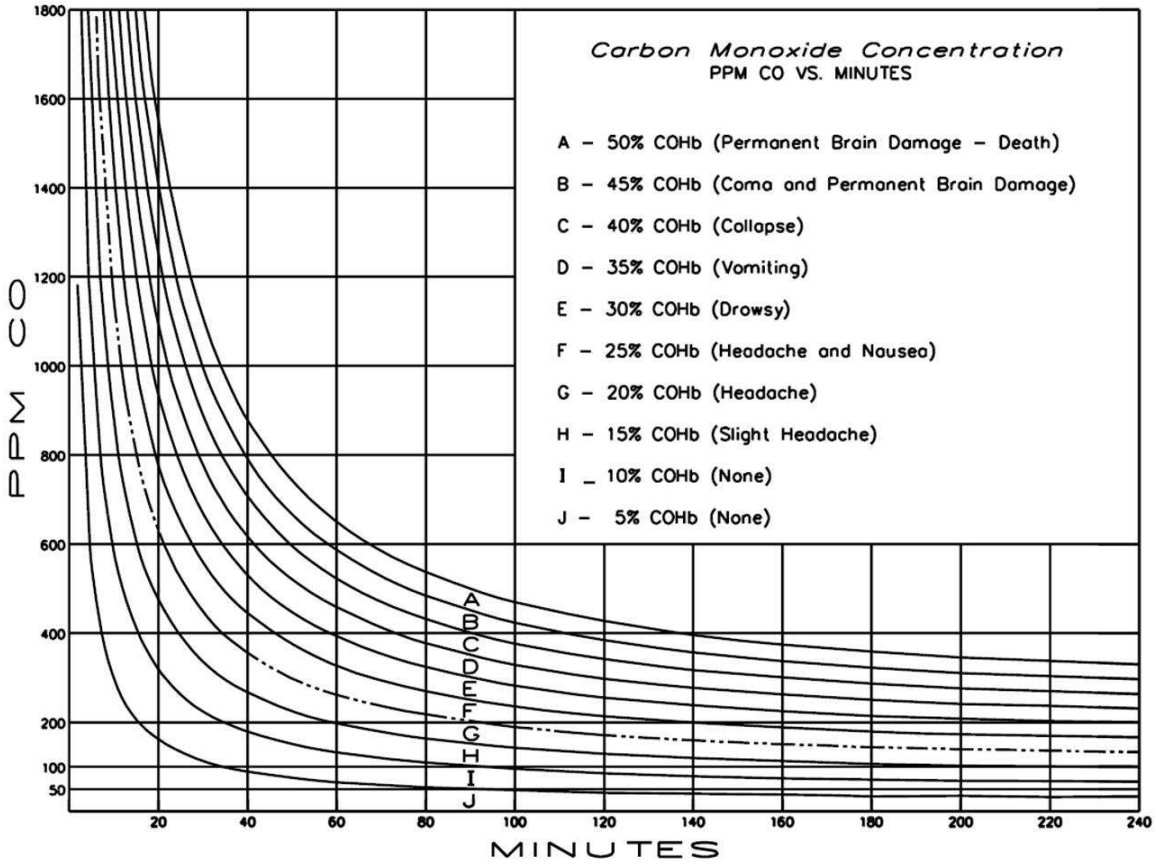

Figure 2.6: Carbon monoxide concentration (ppm CO) versus time (min). Plot is overlaid with a set of curves with each curve representing a constant carboxyhemoglobin (COHb) percentage in the human blood. This plot presents the approximate amount of time a human can be exposed to a certain CO concentration before the COHb percentages in the blood reach a given level. Also included are the physiological symptoms associated with the different COHb percentages in the blood [9].

Table 2.2
CO Poisoning Symptoms Correlated to Concentration and Duration of Exposure[†‡] [9]

	Carbon Monoxide Steady-State Exposure Concentration (ppm CO)					
Symptom(s)	50	100	200	400	800	1600
Slight Headache		3 to 4 hr	60 min	25 min	10 min	6 min
Headache			90	35	15	8
Headache & Nausea			140	45	20	10
Drowsy			240	60	25	12
Vomiting				75	30	14
Collapse				90	35	16
Coma & Brain Damage				110	40	18
Brain Damage – Death				135	45	20

[†] Tabulated data from Figure 2.6 [9].
[‡] All times are approximate and given in minutes except where noted.

CO poisoning is treatable even for someone who is unconscious as long as they are removed from the environment that contains CO and are given fresh air to breathe prior to the onset of permanent brain damage [28]. Although the strong bond that CO makes with Hb is reversible, dissociation is slow and can take a long time [29, 34]. Treatments are available to help revive a person with CO poisoning and usually involve administering 100% O_2 at sea level pressure [29, 36, 37] or at a pressure slightly above sea level (usually 2 to 3 atm absolute pressure) [38–41]. However, treatment can vary depending on the nature of the exposure and the overall age and health condition of the patient.

Fourier Transform Infrared Spectroscopy (FTIR) Overview

Principle of Operation

Fourier Transform Infrared Spectroscopy (FTIR) is an analysis technique by which infrared (IR) radiation is transmitted through a material sample in order to determine the sample's composition and quantity. The key to this method is the interaction between the IR radiation and the molecules in the sample. Every polyatomic or heteronuclear diatomic molecule absorbs IR radiation of some frequency or set of frequencies that are specific to that molecule. When the radiation or photon is absorbed by the molecule it undergoes a quantized rotational or vibrational energy transition, as shown in Figure 2.7, which increases the overall energy of the molecule and results in an asymmetrical shift or change of the electric dipole of the molecule [42]. Consequently, homonuclear, diatomic molecules do not absorb IR since there is no shift in the electronic dipole of the molecule as a result of its symmetrical vibration [43]. Thus, when a photon of the proper frequency is incident on a molecule the photon is absorbed and the overall energy of the molecule increases while the energy at the given frequency in the IR beam decreases. This frequency specific loss of energy is measured by the detector and the result is an IR spectra showing how much of each frequency the sample absorbed [43].

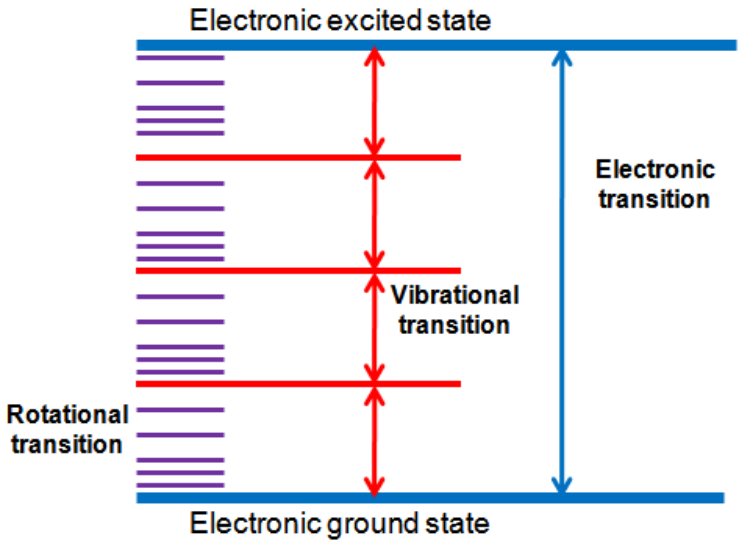

Figure 2.7: Diagram showing the relationship between rotational, vibrational and electronic transitions. IR spectroscopy primarily utilizes the rotational and the vibrational transitions [44].

In order for the FTIR to distinguish between the energy lost at different frequencies it monitors only a single frequency at a time [45]. This means that the FTIR does not expose the sample to all of the frequencies all at once. Rather, the FTIR uses a monochromator to isolate only one frequency and detects the energy lost in the sample for that frequency before moving on to the next one [43, 46]. Also, the standard convention in IR spectroscopy is to use wavenumber instead of frequency to describe which radiation is absorbed and which is transmitted. Wavenumber is defined as the reciprocal of the wavelength of a given frequency and has units of cm^{-1} [43]. Equation 2.2 shows the relationship between wavenumber, frequency and wavelength [46]. All of the FTIR analysis in this study was done in the mid-infrared region which is defined as 4000 to 400 cm^{-1} [43].

$$W = \frac{1}{\lambda} = \frac{\nu}{c} \tag{2.2}$$

where:

W = Wavenumber (cm^{-1})
λ = Wavelength (cm)
ν = Frequency (Hz)
c = Speed of light in a vacuum (cm/s)

The IR spectrum that is obtained from the FTIR is typically plotted in absorbance (unit-less) versus wavenumber (cm^{-1}). This is very useful for determining the concentration of a molecule present in the sample. Quantitative analysis is based on the Beer-Lambert Law which is given in Equation 2.3 [43].

$$A = \log_0\left(\frac{1}{T}\right) = \log_0\left(\frac{I_0}{I}\right) = \varepsilon l c \tag{2.3}$$

where:

A = Absorbance (Unit-less)
T = Transmittance (Unit-less)
I_0 = Intensity measured with no sample in the beam (reference/source intensity)
I = Intensity measured with a sample in the beam (transmitted intensity)
ε = Absorptivity (ppm/m)
l = Pathlength (m)
c = Concentration (ppm)

Analysis of the parameters used in Equation 2.3 shows that the absorbance, A, is measured by the FTIR and the pathlength, *l*, is set by the user, therefore, both of these quantities are known. The absorptivity, ε, is a known proportionality constant given a specific molecule vibrating at a specific wavenumber. This leaves the concentration, c, as the only unknown variable in Equation 2.3 which can be determined based on the knowledge of the other parameters. Thus, using the Beer-Lambert Law the concentration of a specific molecule can be determined by analyzing the IR spectrum obtained from the FTIR.

Interpretation of IR spectra can be very challenging even with simple sample compositions. Historically, FTIR users were required to manually interpret the spectrum by visually comparing spectra of known sample compositions and concentrations to the unknown spectrum. Today, computers and accompanying software are able to provide a much faster, more reliable and more repeatable method for determining molecular concentrations for IR spectra [45].

IR Absorption Properties

As discussed previously, IR spectra are the result of quantized rotational or vibrational energy changes among the molecules of the sample [42]. In addition, there is only a finite number of ways that a molecule can move. These are given by the number of degrees of freedom and are dependent on the geometry of the molecule. In general, a molecule with N atoms has $3N$ degrees of freedom [42, 45]. Three of these degrees of freedom represent translational motion in the three mutually perpendicular directions while an additional three represent rotational motion about the same three directions [45]. The remaining $3N - 6$ degrees of freedom are the fundamental vibrational modes of the molecule [45]. The number of vibrational modes for a linear molecule are $3N - 5$ since rotation about the bonding axis results in no atomic displacement which reduces the inherent degrees of freedom from six to five [45]. It is these vibrational modes that determine which frequencies will be absorbed by the molecule and, thus, ultimately determine its unique IR spectrum.

Carbon Monoxide (CO)

CO is a heterogeneous, diatomic, linear molecule and its spectrum from the QASoft® database is shown in Figure 2.8. CO (N = 2) has only one vibrational mode as given by 3*2-5 = 1 [42, 45] which has a characteristic vibrational frequency of $k_1 = 2138 cm^{-1}$ [42, 47]. As the carbon and oxygen atoms of the CO molecule vibrate they move along the bonding axis which, as described above, results in IR absorption, and Figure 2.9 gives a visual representation of the motion of the atoms while they vibrate.

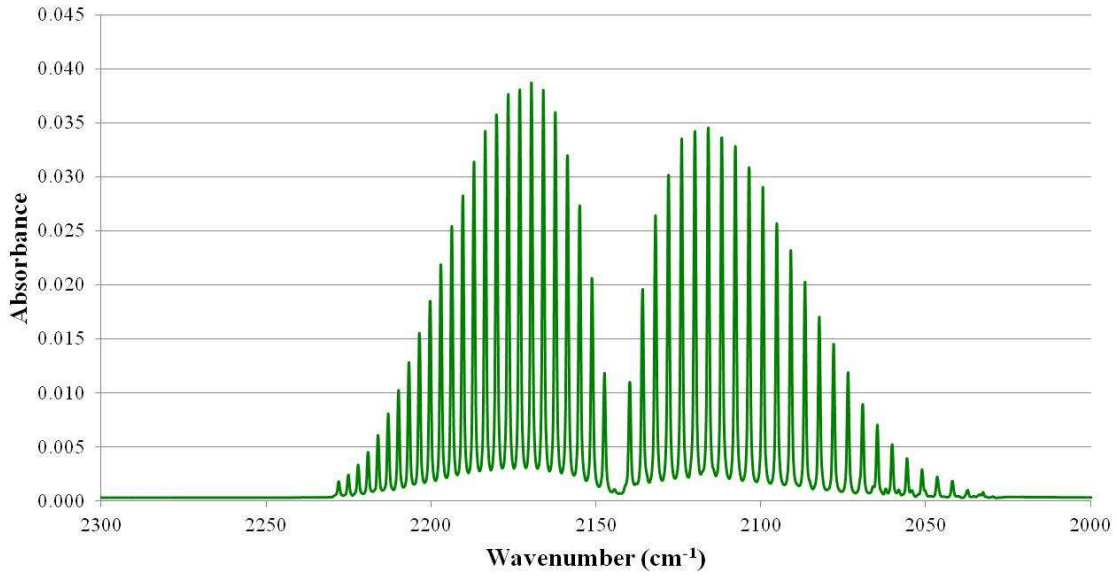

Figure 2.8: The IR spectrum of CO from the QASoft® database. Spectrum of 100 ppm-meters CO in 101.3 kPa (1 atm) air.

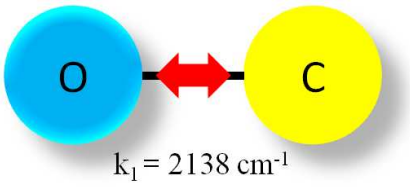

Figure 2.9: The fundamental vibrational mode for CO $k_1 = 2138cm^{-1}$. [44]

Detection of CO gas is the focus of this research and it is very important that the FTIR be able to properly detect it. However, CO is a relatively weak IR absorbing species and its spectrum can be distorted by other, stronger species. It is important to understand the possible factors that can contribute to this error.

Atmospheric Gases

CO_2 and water vapor (H_2O) are two very common species that exist in large quantities in the atmosphere. Ironically, both CO_2 and H_2O have vibrational modes with IR absorption bands that are very close to, and potentially overlap, that of CO. This makes it necessary to investigate the IR absorption properties of CO_2 and H_2O to ensure that their influence on the measurement of CO by the FTIR is understood and properly taken into account.

CO_2 is a heterogeneous, linear, tri-atomic molecule and has three characteristic vibrational modes given by 3*3 – 6 = 3 [42, 45] with wavenumbers of $k_1 = 1337cm^{-1}$, $k_2 = 667cm^{-1}$ and $k_3 = 2349cm^{-1}$, respectively [42, 48]. The spectrum of CO_2 is shown in Figure 2.10. The CO_2 k_1 mode produces no spectral peak due to the oxygen atoms vibrating symmetrically about the carbon atom which results in no shift of its electric

dipole. The CO_2 k_2 mode is far away from the CO vibrational mode and has no effect in the measurement of the CO spectrum. The CO_2 k_3 vibrational mode, however, is only 206 cm^{-1} wavenumbers higher than that of CO placing them close enough together that the IR absorption bands of the CO_2 and the CO might overlap resulting in an incorrect measurement of the CO spectrum.

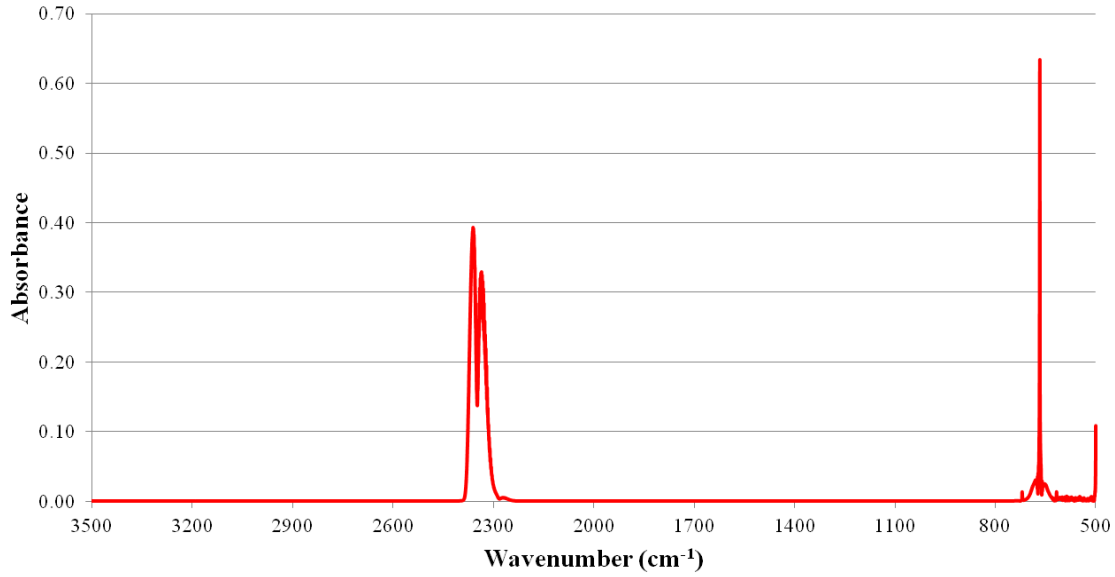

Figure 2.10: The IR spectrum of CO_2 from the QASoft® database. Spectrum of 100 ppm-meters CO_2 in 1 atm. N_2 at 25 °C.

H_2O is a heterogeneous, bent, tri-atomic molecule that also has three characteristic vibrational modes as given by 3*3 – 6 = 3 [42, 45] with wavenumbers of k_1 = 3657 cm^{-1}, k_2 = 1595 cm^{-1} and k_3 = 3756 cm^{-1}, respectively [42, 49]. The spectrum of H_2O is shown in Figure 2.11. H_2O vibrational modes k_1 and k_3 have much higher wavenumbers than the vibrational mode of CO and do not affect the measurement of the CO spectrum by the FTIR. On the other hand, the H_2O k_2 mode is a very large mode covering a broad range of wavenumbers. It is so broad, in fact, that IR absorption bands

from the k_2 mode of H_2O encroach on the absorption bands of CO providing potential overlap of the two spectra.

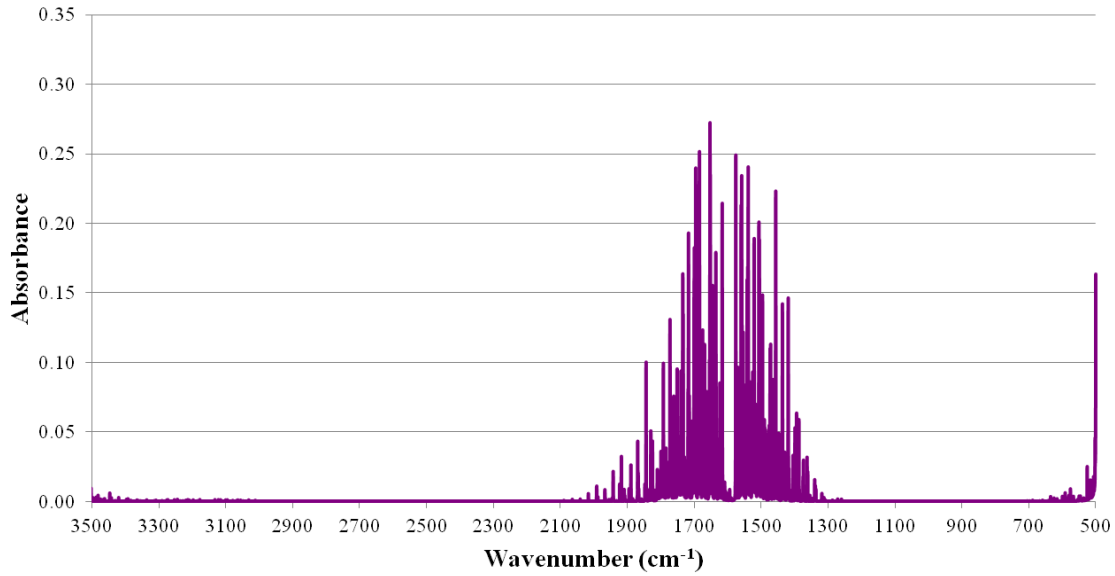

Figure 2.11: The IR spectrum of H_2O from the QASoft® database. Spectrum of 1000 ppm-meters H_2O in 101.3 kPa (1 atm) N_2 at 25 °C.

In reality, the overlap of the CO spectrum with that of CO_2 and H_2O is small. However, the overlap could cause significant error in the measurement of CO especially at lower CO concentrations due to the fact that the IR cross-section of CO is small in comparison to that of CO_2 and H_2O. For example, if CO_2 and CO were to absorb IR at a given frequency, the CO_2 absorption would dominate over the CO absorption making it impossible to analyze that frequency for CO. Chapter 3 of this thesis will provide the procedure by which the interference due to the spectral overlap of CO_2 and H_2O with CO was accommodated.

Carbon Monoxide Sensor Technology Overview

There are two technologies commonly used in commercially available CO sensors: electrochemical and metal oxide semiconductor (MOS). Only electrochemical sensors were selected for evaluation in this study. There are performance requirements for CO sensors [9] and even standards for testing CO sensors [50], but little research has been published on the ability of the CO sensors to meet the anticipated requirements at lower pressures onboard aircraft.

One study was done by L. A. Gundel et al. (2010) where the effects of pressure, humidity and temperature on select CO sensors were studied [51]. The study included two electrochemical sensors and one MOS sensor where the pressure was varied stepwise over the pressure range of 1 to 0.7 atm, the relative humidity was varied from 10 to 65% and the temperature was varied between 65 to 85 °F. All of the pressure, humidity and temperature experiments were done independently of each other and the sensors were evaluated in known amounts of CO mixed with room air. The results showed poor reproducibility and significant hysteresis for both the electrochemical and MOS CO sensors, and it was recommended that the next step be to achieve a reproducible and predictable CO sensor response to changes in pressure, humidity and temperature. This study ultimately concluded that none of the tested sensors (CO or otherwise) were well suited for widespread deployment to monitor the air quality onboard aircraft.

Electrochemical

The electrochemical CO sensors that were evaluated in this study were amperometric sensors, meaning that the amount of electrical current generated by the

sensor is proportional to the concentration of CO to which the sensor is exposed [52]. These sensors use a H_2O based electrolyte to facilitate the oxidation/reduction reaction that governs the sensors operation. Figure 2.12 gives a schematic representation of the operating principle of the Figaro 5042 electrochemical CO sensor, while the basic oxidation/reduction reaction on which their operation is based is presented in Equation 2.4. In this process there are two half reactions that occur [53–55]. The first half reaction generates electrons at the working electrode when CO is oxidized by H_2O, and, as Equation 2.4a suggests, the number of electrons generated is twice the number of oxidized CO molecules which creates an electron concentration proportional to the CO concentration. The second half reaction sinks the electrons at the counter electrode when ambient O_2 inside the sensor is reduced to form H_2O, shown in Equation 2.4b [54, 55]. Thus, when the working and the counter electrodes are electrically connected a current is created that is proportional to the amount of CO present at the sensor and the components of the H_2O based electrolyte are replenished allowing the sensor to have a longer lifetime [56]. The overall reaction of the electrochemical cell is given in Equation 2.4c.

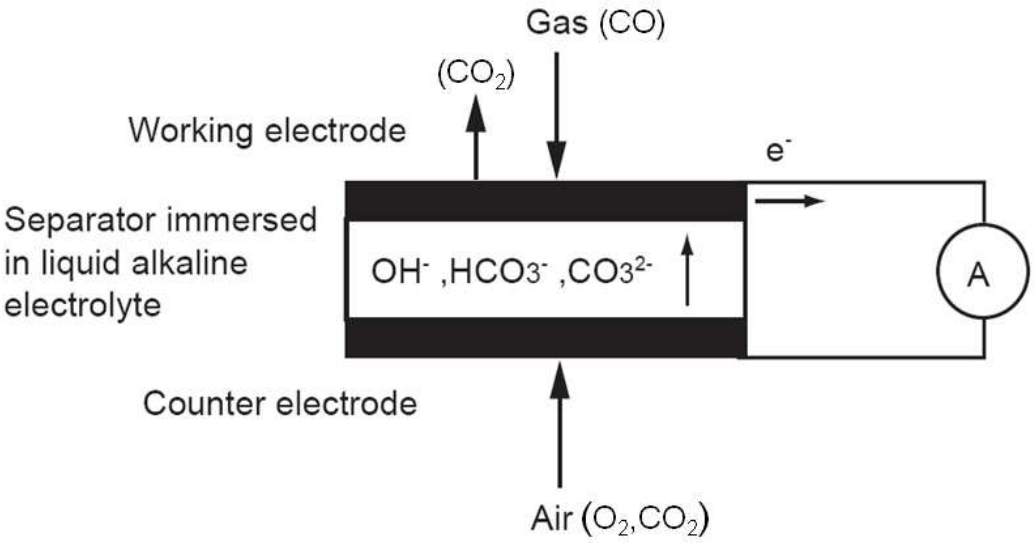

Figure 2.12: Adapted schematic diagram which demonstrates the operation principle of the Figaro 5042 electrochemical CO gas sensor [56].

Working Electrode: (Oxidation Reaction)
$$CO + H_2O \rightarrow CO_2 + 2H^+ + 2e^- \quad (2.4a)$$

Counter Electrode: (Reduction Reaction)
$$\frac{1}{2}O_2 + 2H^+ + 2e^- \rightarrow H_2O \quad (2.4b)$$

Overall Reaction:
$$CO + \frac{1}{2}O_2 \rightarrow CO_2 \quad (2.4c)$$

The specific ions contained in the electrolyte and that are involved in the oxidation/reduction reaction for the Figaro 5042 are hydroxide (OH^-), bicarbonate (HCO_3^-) and carbonate (CO_3^{2-}), as shown in Figure 2.12. Each ion has its own oxidation/reduction reaction that the sensor uses to generate its output signal. The oxidation/reduction reaction involving OH^- is given in Equation 2.5 [56].

Working Electrode: (Oxidation Reaction)
$$CO + 2OH^- \rightarrow CO_2 + H_2O + 2e^- \quad (2.5a)$$

Counter Electrode: (Reduction Reaction)
$$\frac{1}{2}O_2 + H_2O + 2e^- \rightarrow 2OH^- \quad (2.5b)$$

OH^- is generated at the counter electrode when O_2 is reduced and is then transported to the working electrode where it oxidizes CO to form CO_2 and electrons. The oxidation/reduction reaction involving HCO_3^- is given in Equation 2.6 [56].

Working Electrode: (Oxidation Reaction)
$$CO + 2HCO_3^- \rightarrow 3CO_2 + H_2O + 2e^- \quad (2.6a)$$

Counter Electrode: (Reduction Reaction)
$$\frac{1}{2}O_2 + 2CO_2 + H_2O + 2e^- \rightarrow 2HCO_3^- \quad (2.6b)$$

In this reaction, the HCO_3^- is a product of the reduction reaction at the counter electrode and is then transported to the working electrode where it is a reactant in the oxidization of CO to form CO_2 and electrons. The oxidation/reduction reaction involving CO_3^{2-} is given in Equation 2.7 [56].

Working Electrode: (Oxidation Reaction)
$$CO + CO_3^{2-} \rightarrow 2CO_2 + 2e^- \quad (2.7a)$$

Counter Electrode: (Reduction Reaction)
$$\frac{1}{2}O_2 + CO_2 + 2e^- \rightarrow CO_3^{2-} \quad (2.7b)$$

In this reaction, the CO_3^{2-} is generated by the reduction of O_2 at the counter electrode and is then transported to the working electrode where it oxidizes CO to form CO_2 and electrons. These are the ions and the oxidation/reduction reactions used in the operation

of the Figaro 5042 electrochemical CO sensor. The e2v sensor likely has the same or similar ions that are used in its electrolyte although no specific information is given in the sensor's datasheet.

In addition, according to the literature, electrochemical CO sensors require O_2 inside and around the sensor in order for the reduction reaction at the counter electrode to properly take place [54, 55]. The necessity of the ambient O_2 at the sensor was evaluated in this study since most of the experiments were performed in an anaerobic, N_2 environment. Also, the electrochemical sensors typically have good selectivity in the presence of interference gasses with the exception of hydrogen gas which has been demonstrated to contribute to the output signal of the electrochemical sensors, as shown by the Figaro 5042 cross sensitivity chart in Figure 2.13.

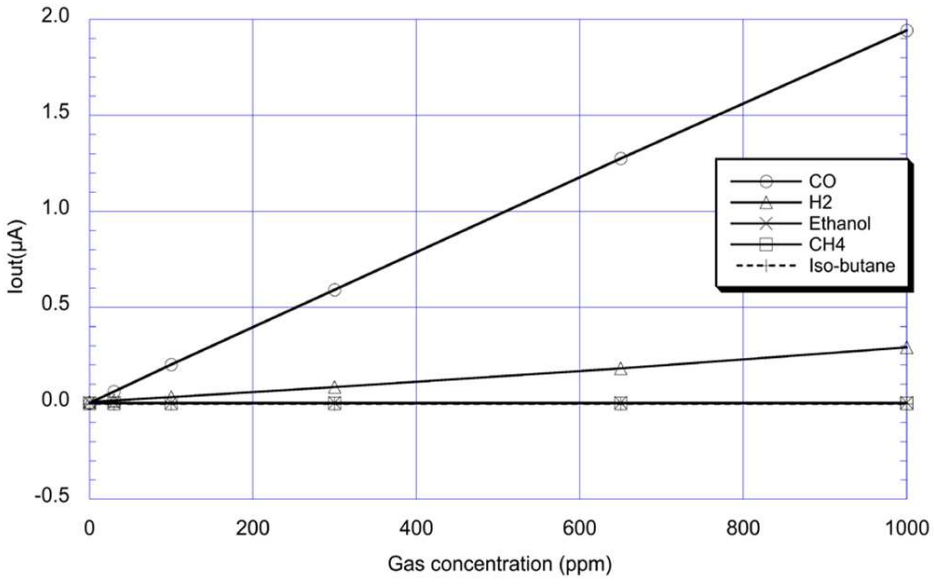

Figure 2.13: Cross sensitivity to various gases for Figaro 5042 [56].

Metal Oxide Semiconductor (MOS)

The other major technology currently used in commercially available CO sensors is MOS. MOS CO sensors are conductivity based sensors meaning that the conductivity, and inversely the resistance, of the sensing surface changes in the presence of CO. The sensing surface of the MOS sensors is made of a metal oxide, usually tin oxide (SnO_2), deposited on a semiconductor substrate [57]. When the sensor is exposed to clean air the conductivity is low, yet when the sensor is in the presence of a reducing gas such as CO the conductivity increases [52]. This increase in conductivity is due to electrons being transferred to the SnO_2 when the CO is oxidized. Also, the SnO_2 must be heated to an elevated temperature in order for the reaction to occur [58]. If the temperature is not properly controlled then the sensor will lose its ability to properly detect CO and be subject to interference from other gasses. In fact, there is one commercially available MOS CO sensor that functions as a CO and methane sensor simply by changing the temperature of the sensing surface [59]. To reduce the influence of interfering gases, most MOS CO sensors use an activated charcoal filter which filters out the unwanted gases through adsorption. Figure 2.13 shows a picture of a MOS CO sensor along with a schematic diagram of the sensor surface as well as an exploded view of the various components of a MOS CO sensor.

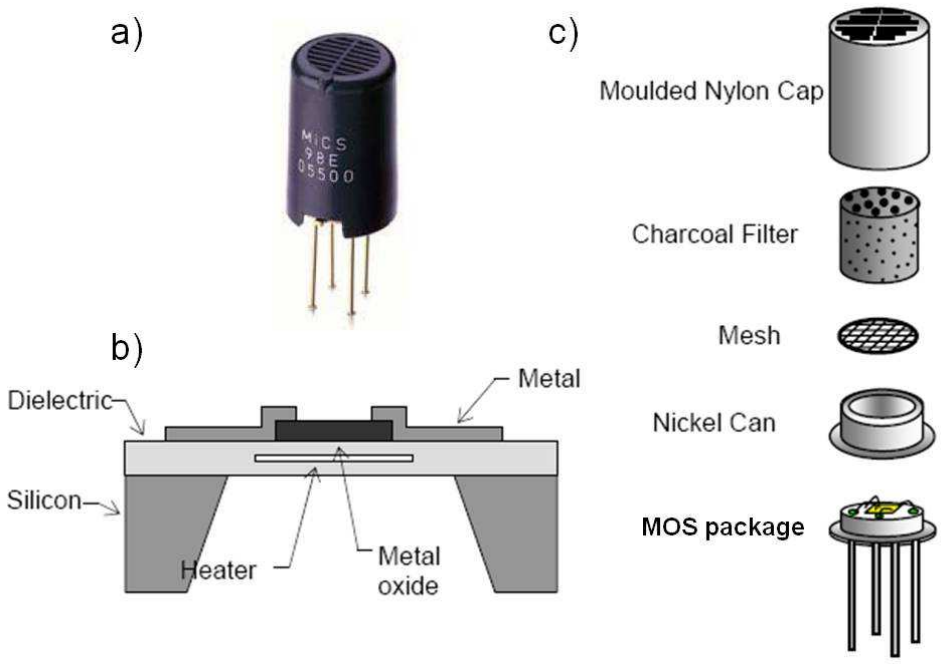

Figure 2.14: a) Picture of a typical MOS CO sensor b) Schematic diagram of the MOS CO sensor structure c) Exploded view of the components of a typical MOS CO sensor [58]

Chapter 3: Materials and Methods

Sensor Evaluation System

A laboratory apparatus was developed to evaluate the performance of commercially available CO sensors in a controlled environment. In this system, the CO concentration and the total pressure to which the sensors are exposed can be reliably varied. This laboratory apparatus, shown in Figure 3.1, consists of a control module, a sensor evaluation chamber and a Fourier Transform Infrared Spectrometer (FTIR) gas analysis chamber. The entire sensor evaluation system was plumbed with 6.35 mm (0.25 inches) outer diameter Teflon® tubing that is rated for vacuum pressures of 50.5 kPa (0.5 atm) with Swagelok® compression fittings.

a)

b)

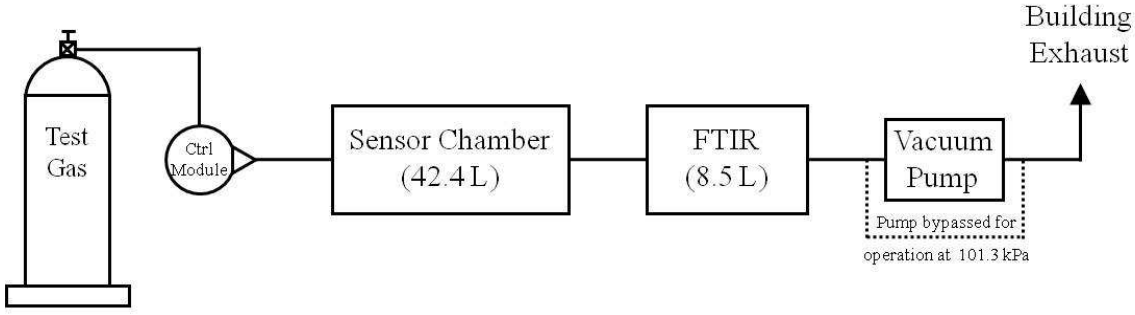

Figure 3.1: a) Picture of sensor evaluation system showing the Control Module (right), Sensor Evaluation Chamber (left, front) and the FTIR Gas Analysis Chamber (left, back). b) Block diagram of sensor evaluation system.

The control module, shown in Figure 3.2, was fitted with two Smart-Trak 2 (Sierra Instruments, Inc., Monterey, CA, USA) digital mass flow controllers (MFC). The first MFC (C100L-RD-2-OV1-SV1-PV2-V1-SO-C10-LF) had a flow rate range of 0 to 10 sccm, while the second MFC (C100L-RD-2-OV1-SV1-PV2-V1-SO-C10) was capable of controlled flow over the range of 0 to 500 sccm. Due to the relatively low maximum controlled flow of the first MFC (0 to 10 sccm), the second MFC (0 to 500 sccm) was used exclusively in this study allowing for shorter experimental run times. The 0 to 500 sccm MFC allowed for the control of the flow rate of the N_2 purge gas (NI CZ200 or NI R300, Airgas, Inc., USA) as well as the CO in N_2 test gas (Airgas, Inc., USA).

Figure 3.2: Control Module from the sensor evaluation system

The control module was also used to vary the pressure inside the sensor evaluation system. This was accomplished by adjusting the inlet-to-outlet pressure differential of a diaphragm pump (DOA-P704-AA, Gast Manufacturing, Inc., Benton, MI, USA). The control module also provided access to the valves used to direct the flow of the gases inside the sensor evaluation system.

The sensor evaluation chamber (Terra Universal, Inc., Fulerton, CA, USA) is a vacuum sealed chamber made of Acrylic with outer dimensions of 430 by 430 by 343 mm (17 by 17 by 13.5 inches) and a total internal volume of 42.4 liters (0.0424 m^3), shown in Figure 3.3. The sensor evaluation chamber was sealed with a compression

O-ring and Dow Corning® High Vacuum Grease (Dow Corning Corporation, Midland, MI, USA).

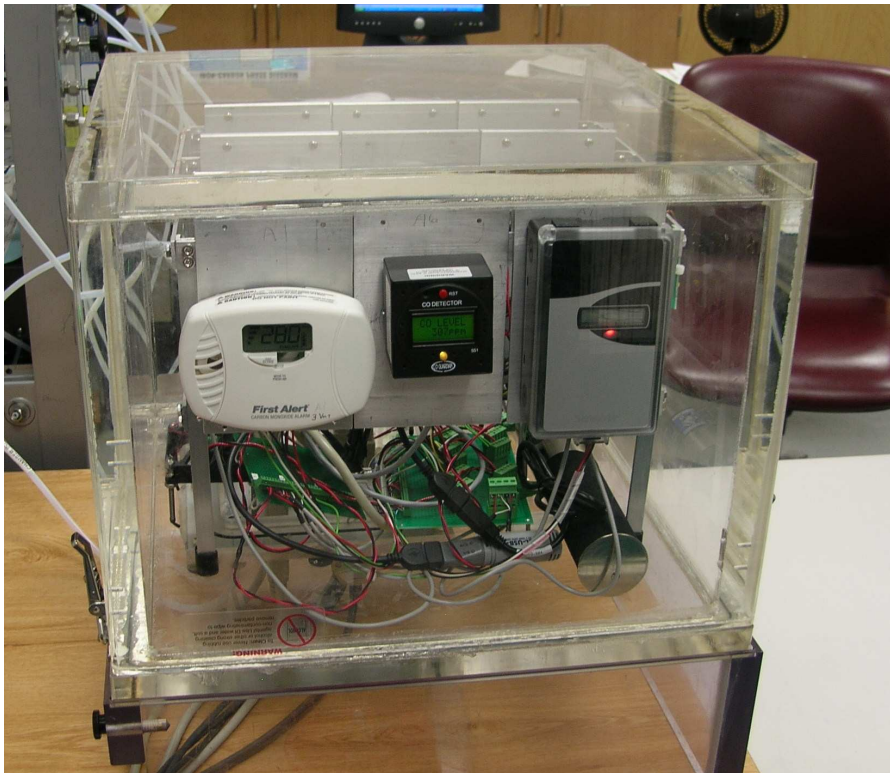

Figure 3.3: Sensor evaluation chamber from the sensor evaluation system.

The sensor evaluation chamber also exhibits a feed-through panel with dimensions of 149 by 149 mm (5 ⅞ by 5 ⅞ inches) mounted under the bottom of the chamber. This panel was sealed with a compression O-ring, Dow Corning® High Vacuum Grease and held in place by eight thumb screws. Mounted to this panel were the gas inlet and outlet, as well as five, twenty-five pin Xavac® series hermetically sealed feed-through connectors (Positronic Industries, Springfield, MO, USA). These connectors were used to pass electrical power and data acquisition signals through the base of the sensor evaluation chamber while maintaining the integrity of the vacuum seal.

The CO sensors were mounted on a multi-sensor rack which was designed and custom built by the research team. Only minor modifications were made, if necessary, to the sensors' outer packaging to facilitate the installation of electrical power, data acquisition wires, and physical mounting on the rack. Unfortunately, automatic data recording was not able to be installed for every sensor. However, these sensors conveniently provided a digitally displayed readout of their measured CO concentration on the sensor which allowed the data to be recorded manually by periodic, visual inspection.

In addition, a Spectrum GX FTIR (PerkinElmer, Inc., Shelton, CT, USA) with a M-5-22-V variable pathlength long pass gas cell (Infrared Analysis, Inc., Anaheim, CA, USA), shown in Figure 3.4, was connected to the sensor evaluation chamber to provide an additional means of verifying the CO concentration to which the CO sensors were exposed. The FTIR was operated via the Spectrum® software which was developed by PerkinElmer, Inc. The transmitted IR is measured by a fast recovery deuterated triglycine sulfate (FR-DTGC) detector. The FTIR is capable of scanning over the wavenumber range of 10,000 to 400 cm^{-1} with a spectral resolution of 64 to 0.2 cm^{-1}. The total pathlength of the variable pathlength long pass gas cell can be adjusted in increments of 2.24 meters from 2.24 to 22 meters with the optical path folded in a volume of 8.5 liters (0.0085 m^3). Quantitative CO concentrations were obtained from the FTIR spectra by analysis with QASoft® (Infrared Analysis, Inc., Anaheim, CA, USA). The FTIR operating methods that were used are discussed in detail later in this chapter.

Figure 3.4: FTIR gas analysis chamber from the sensor evaluation system.

Analytical CO Concentration Prediction Model

In order to gain a better understanding of the flow dynamics of the sensor evaluation system, a differential equation based model was developed to predict the expected concentration of CO in the sensor evaluation system at any given time during the experiment. The following assumptions were made in the development of this model:

1. All of the constituents of the gas mixture inside the system are well mixed. Two fans were placed inside the sensor evaluation chamber to ensure that this condition was met.
2. The total flow rate of test gas into the system is equal to the flow out, $F_i = F_o$.
3. The CO source is assumed to be a constant and infinite source of the test gas.

4. There is a negligible amount of CO inside the sensor evaluation system when the experiment begins, i.e., $C_{CO}(t = 0) = 0$. The system was purged with N_2 for at least eight hours prior to the start of the flow of the CO test gas to ensure that this condition was met.
5. The pressure inside the system is 101.3 kPa (1 atm).
6. The gas supply tubes have negligible volume. The actual volume of the tubes was approximated to be 0.4 L which is 0.8% of the total system volume and can, therefore, be ignored.

This model was derived by determining the mass of the test gas inside the sensor evaluation chamber at any time, $m_{chamber}(t)$, and then by dividing the mass of the test gas inside the chamber by the volume of the chamber to determine the concentration, $C_{CO}(t)$. This model was developed based on the principle that the change in the amount of the test gas in the sensor evaluation chamber, $\frac{dm_{chamber}}{dt}$, is equal to the rate of the test gas into the chamber, $\dot{m}_{in}$, minus the rate of the test gas out of the chamber, $\dot{m}_{out}$, as shown in Equation 3.1.

$$\frac{dm_{chamber}}{dt} = \dot{m}_{in} - \dot{m}_{out} \tag{3.1}$$

where:

$\frac{dm_{chamber}}{dt}$ = change in mass of test gas inside chamber over time (mg/min)

$\dot{m}_{in}$ = rate of test gas into chamber (mg/min)

$\dot{m}_{out}$ = rate of test gas out of chamber (mg/min)

The rate at which CO enters the chamber, $\dot{m}_{in}$, was calculated as the product of the CO test gas source concentration, C_s, and the rate at which this gas is flowing into the chamber, F_i, as shown in Equation 3.2a. The rate at which CO leaves the chamber, $\dot{m}_{out}$, is given by the product of the concentration of CO leaving the chamber and the flow rate of the gas leaving the chamber, F_o, as shown in Equation 3.2b.

$$\dot{m}_{in} = F_i \cdot C_s \tag{3.2a}$$

$$\dot{m}_{out} = F_o \cdot \frac{m_{chamber}(t)}{Vol_{chamber}} \tag{3.2b}$$

where:

F_i = Flow rate of CO entering chamber (cm^3/min)
F_o = Flow rate of the gas leaving chamber (cm^3/min)
C_s = CO test gas source concentration (mg/m^3)
$m_{chamber}(t)$ = Mass of CO inside chamber at time, t (mg)
$Vol_{chamber}$ = Volume of sensor evaluation chamber (m^3)

Substituting Equations 4.2a and 4.2b into Equation 3.1 yields

$$\frac{dm_{chamber}}{dt} = F_i \cdot C_s - F_o \cdot \frac{m_{chamber}(t)}{Vol_{chamber}} \tag{3.3}$$

Equation 3.3 is a linear differential equation and was easily solved by separating variables and integrating. Solving Equation 3.3 and evaluating the initial condition of $m_{chamber}(t=0)=0$ gives

$$m_{chamber}(t) = \frac{Vol_{chamber} \cdot F_i \cdot C_s}{F_o}\left[1 - e^{\frac{-F_o \cdot t}{Vol_{chamber}}}\right] \tag{3.4}$$

By applying the assumption $F_i = F_o$ to Equation 3.4and dividing both sides of the equation by $Vol_{chamber}$ yields the concentration of CO inside the chamber as a function of time, $C_{CO}(t)$, as shown in Equation 3.5.

$$C_{CO}(t) = \frac{m_{chamber}(t)}{Vol_{chamber}} = C_s\left[1 - e^{\frac{-F_o \cdot t}{Vol_{chamber}}}\right] \tag{3.5}$$

where:

$C_{CO}(t)$ = Concentration of CO inside chamber at time, t (mg/m^3)

This prediction model was tested using the 8.5 liter (0.0085 m^3) gas analysis chamber attachment to the FTIR. The results, shown in Figure 3.5, demonstrate that the model provides a good prediction of the CO concentration inside a given chamber. In this particular case, a flow rate of 500 sccm with a source concentration of 932 mg CO/m^3 (800 ppm CO) was used at a pressure of 101.3 kPa.

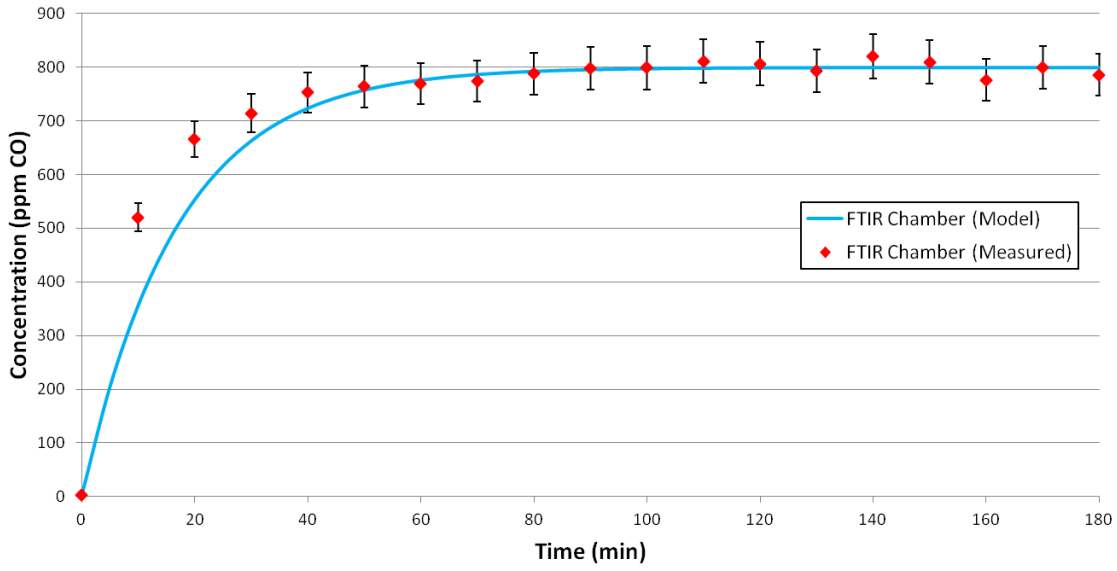

Figure 3.5: Comparison of the experimental measurements and the analytical model prediction of the CO concentration over time for a single chamber. A flow rate of 500 sccm was used in the calculation with a source CO concentration of 932 mg CO/m^3 (800 ppm CO) at a pressure of 101.3 kPa. FTIR measurements are plotted with ±5% of the measured value.

The previously described model was able to accurately predict the final, steady state CO concentrations for single chamber systems. In the case of the sensor evaluation chamber being operated in series with the FTIR gas analysis chamber, this model needed modification. A second equation was needed to describe the CO concentration in the second chamber which, in the case of these experiments, was the FTIR gas analysis chamber. This equation was developed in a similar manner as Equation 3.5 with the change in the mass of CO inside the FTIR chamber, $\frac{dm_{FTIR}}{dt}$, being equal to the rate of the CO into the chamber, $\dot{m}_{in}$, minus the rate of the test gas out of the chamber, $\dot{m}_{out}$, as shown in Equation 3.1. However, the assumption that the source concentration into the FTIR chamber is constant and infinite was no longer valid. Instead, the CO concentration flowing into the FTIR chamber is the CO concentration flowing out of the sensor evaluation chamber. With this adjustment, $\dot{m}_{in}$ and $\dot{m}_{out}$ become Equation 3.6a and Equation 3.6b, respectively.

$$\dot{m}_{in} = F_i \cdot \frac{m_{chamber}(t)}{Vol_{chamber}} \tag{3.6a}$$

$$\dot{m}_{out} = F_o \cdot \frac{m_{FTIR}(t)}{Vol_{FTIR}} \tag{3.6b}$$

where:

F_i = Flow rate of CO entering chamber (cm^3/min)
F_o = Flow rate of the gas leaving chamber (cm^3/min)
$m_{chamber}(t)$ = Mass of CO inside chamber at time, t (mg)
$m_{FTIR}(t)$ = Mass of CO inside FTIR gas analysis chamber at time, t (mg)
$Vol_{chamber}$ = Volume of sensor evaluation chamber (m^3)
Vol_{FTIR} = Volume of FTIR gas analysis chamber (m^3)

Substituting Equations 3.6a and Equation 3.6b into Equation 3.1 yields the linear differential equation shown in Equation 3.7.

$$\frac{dm_{FTIR}}{dt} = F_i \cdot \frac{m_{chamber}(t)}{Vol_{chamber}} - F_o \cdot \frac{m_{FTIR}(t)}{Vol_{FTIR}} \tag{3.7}$$

Equation 3.7 was solved and the initial condition of $m_{FTIR}(t = 0) = 0$ was applied resulting in the CO concentration inside the FTIR gas analysis chamber, $C_{FTIR}(t)$, shown in Equation 3.8.

$$C_{FTIR}(t) = \frac{m_{FTIR}(t)}{Vol_{FTIR}} = \frac{C_s}{(Vol_{chamber} - Vol_{FTIR})}\left[Vol_{chamber}\left(1 - e^{\frac{-F_o \cdot t}{Vol_{chamber}}}\right) - Vol_{FTIR}\left(1 - e^{\frac{-F_o \cdot t}{Vol_{FTIR}}}\right)\right] \tag{3.8}$$

where:

$C_{FTIR}(t)$ = Concentration of CO inside FTIR gas analysis chamber at time, t (mg/m^3)

The predicted concentrations from Equation 3.5 and Equation 3.8 are plotted in Figure 3.6. This figure shows that the concentration in the FTIR chamber lags behind that of the sensor evaluation chamber, as expected. This is due to the output of the sensor chamber being connected to the input of the FTIR chamber which results in a constantly changing input CO concentration for the FTIR.

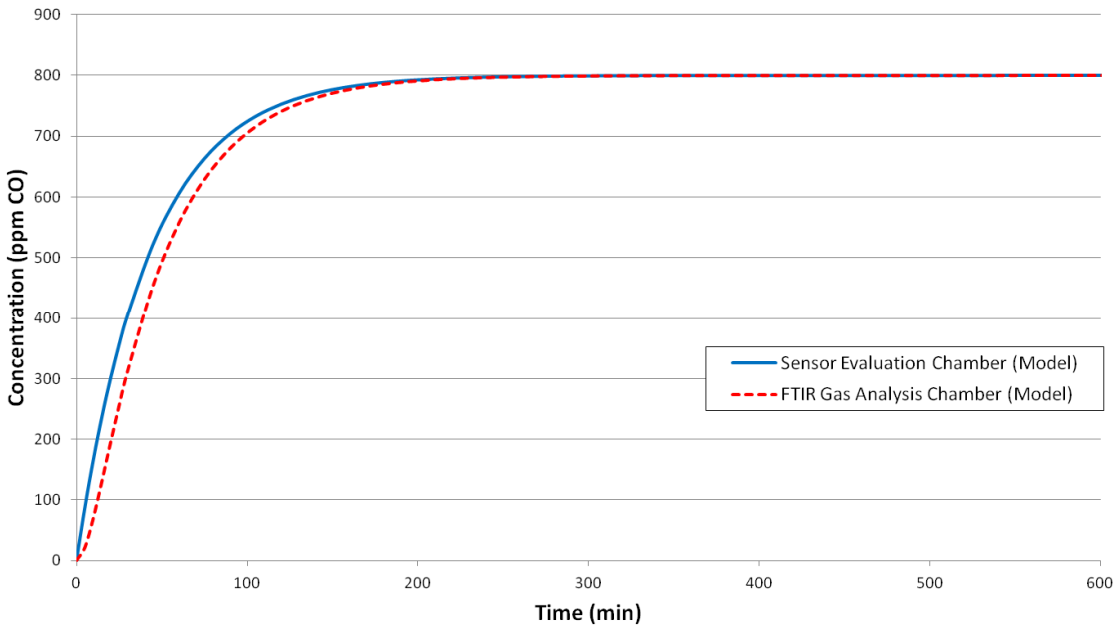

Figure 3.6: Plot of the analytical, prediction model for the sensor evaluation chamber connected in series with the FTIR gas analysis chamber. A flow rate of 500 sccm was used in the calculation with a source CO concentration of 932 mg CO/m^3 (800 ppm CO) at a pressure of 101.3 kPa (1 atm).

One of the underlying assumptions used in the development of Equation 3.5 and Equation 3.8 was that the pressure inside the sensor evaluation system was equal to 101.3 kPa (1 atm). This assumption worked well for experiments performed at sea level pressure, but it became limiting when others pressures were investigated. It was then necessary to modify Equation 3.5 and Equation 3.8 to accommodate pressures other than just 101.3 kPa (1 atm). This change was made following the work of Haney [44] where the ratio of the atmospheric pressure, P (101.3 kPa), to the pressure inside the system, P_{sys}, was multiplied by the mass flow rate out, $\dot{m}_{out}$. Thus, Equation 3.3 was modified and became Equation 3.9 and in like manner Equation 3.7 became Equation 3.10.

$$\frac{dm_{chamber}}{dt} = F_i \cdot C_s - F_o \cdot \frac{m_{chamber}(t)}{Vol_{chamber}}\left(\frac{P}{P_{sys}}\right) \tag{3.9}$$

$$\frac{dm_{FTIR}}{dt} = F_i \cdot \frac{m_{chamber}(t)}{Vol_{chamber}} - F_o \cdot \frac{m_{FTIR}(t)}{Vol_{FTIR}}\left(\frac{P}{P_{sys}}\right) \tag{3.10}$$

where:

P = Atmospheric pressure (101.3 kPa)

P_{sys} = Pressure inside the sensor evaluation system (kPa)

Solving Equation 3.9 and Equation 3.10 gives an analytical, prediction model that takes the pressure inside the system into account which is presented in Equation 3.11 and Equation 3.12.

$$C_{CO}(t) = \frac{m_{chamber}(t)}{Vol_{chamber}} = \left(\frac{C_s * P_{sys}}{P}\right)\left[1 - e^{\frac{-F_o \cdot t}{Vol_{chamber}}\left(\frac{P}{P_{sys}}\right)}\right] \tag{3.11}$$

$$C_{FTIR}(t) = \frac{m_{FTIR}(t)}{Vol_{FTIR}} =$$

$$\frac{C_s * P_{sys}}{P\left(Vol_{chamber} - Vol_{FTIR}\right)}\left[Vol_{chamber}\left(1 - e^{\frac{-F_o \cdot t}{Vol_{chamber}}\left(\frac{P}{P_{sys}}\right)}\right) - Vol_{FTIR}\left(1 - e^{\frac{-F_o \cdot t}{Vol_{FTIR}}\left(\frac{P}{P_{sys}}\right)}\right)\right] \tag{3.12}$$

The final refinement to the analytical model came when it was discovered that small amounts of air could leak into the sensor evaluation system and dilute the steady state CO concentration when the system was operated at lower pressure. For the purpose of this model, the leak was assumed to be in one location with a constant flow rate of room air into the system. The leak rate was incorporated into the analytical model by an empirically determined correction factor, as shown in Equation 3.13, which is dependent on the ratio of the leak rate to the flow rate of the CO test gas.

$$CorrectionFactor = \frac{1}{1+\frac{F_{leak}}{F_i}} \tag{3.13}$$

where:

F_{leak} = Leak rate of room air into the sensor evaluation system (cm^3/min)
F_i = Flow rate of CO entering the sensor evaluation system (cm^3/min)

The CO concentration at any time, t, for both the sensor evaluation chamber and the FTIR gas analysis chamber was determined by multiplying this factor by both Equation 3.11 and Equation 3.12. The result is shown in Equation 3.14 and Equation 3.15.

$$C_{CO}(t) = \left(\frac{1}{1+\frac{F_{leak}}{F_i}}\right)\left(\frac{C_s * P_{sys}}{P}\right)\left[1-e^{\frac{-F_o \cdot t}{Vol_{chamber}}\left(\frac{P}{P_{sys}}\right)}\right] \tag{3.14}$$

$$C_{FTIR}(t) = \left(\frac{1}{1+\frac{F_{leak}}{F_i}}\right)\frac{C_s * P_{sys}}{P(Vol_{chamber} - Vol_{FTIR})} \cdot \left[Vol_{chamber}\left(1-e^{\frac{-F_o \cdot t}{Vol_{chamber}}\left(\frac{P}{P_{sys}}\right)}\right) - Vol_{FTIR}\left(1-e^{\frac{-F_o \cdot t}{Vol_{FTIR}}\left(\frac{P}{P_{sys}}\right)}\right)\right] \tag{3.15}$$

Equation 3.14 and Equation 3.15 were used as the analytical model to determine the CO concentration at any time, t, inside the sensor evaluation chamber and the FTIR gas analysis chamber, respectively.

Experimental Procedure to Evaluate Carbon Monoxide Sensors

The performance of the CO sensors was evaluated by exposing them to various CO concentrations from purchased, premixed tanks of CO in N_2. The 0 to 500 sccm MFC was used to control the flow of the N_2 purge gas as well as the CO in N_2 test gas. A list of the CO concentrations that were used is shown in Table 3.1 while Figure 3.7 shows a block diagram depicting the flow of the CO test gas. The FTIR settings used for these experiments are provided in Table 3.2. The sensors were evaluated at a pressure of 101.3 kPa (1 atm) in this procedure. It should be noted that in this study the atmospheric pressure inside the laboratory was assumed to be 101.3 kPa (1 atm) which is the atmospheric pressure at sea level. The actual elevation of the laboratory is approximately 700 feet above sea level according to the CM0674 benchmark (Hargis Hall, Auburn University, AL, USA) placed and maintained by National Geodetic Survey. Therefore, the pressure inside the laboratory was slightly lower than 101.3 kPa, and the pressure also varied slightly due to changes in the weather.

1. System was configured for operation of the sensor evaluation chamber in series with the FTIR gas analysis chamber.
2. System was purged with N_2 (NI CZ200) at a flow rate of 500 sccm for at least eight hours.
3. Flow of the CO test gas was set to 500 sccm.
4. After seven hours the flow rate was set to 50 sccm to conserve the CO test gas.
5. Once the steady state concentration had been established (after approximately twenty-four hours) a total of eighteen steady state measurements were taken

which were divided into three sets of measurements. Each measurement set was taken at least one hour apart and contained six measurements, each taken ten minutes apart.

Table 3.1
Carbon Monoxide Concentrations for CO Sensor Experiments

Target Concentration (ppm CO)	Actual Concentration (ppm CO)†	Error†	Standard
18	18.00	± 1%	Primary
50	49.40	± 2%	Certified
100	100.0	± 1%	Primary
150	149.0	± 2%	Certified
250	251.9	± 1%	EPA Protocol

† As certified by Airgas, Inc. at 101.3 kPa (1 atm)

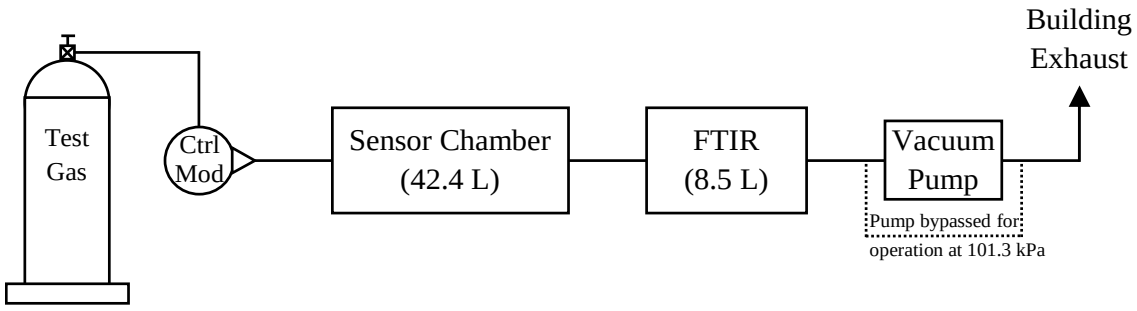

Figure 3.7: Block diagram depicting the flow of the CO test gas for the CO sensor experiments.

Table 3.2
FTIR Settings for CO Sensor Experiments

OPD Velocity	1 cm/s	
Scan Range	2300 to 2000 cm^{-1}	
Resolution	0.5 cm^{-1}	
# of Scans	4	18 ppm CO
	32	150 ppm CO
	52	50, 70, 100, 250, 800 ppm CO

Experimental Procedure to Evaluate Carbon Monoxide Sensors at Reduced Pressure

The effect of pressure on the CO sensor's performance was evaluated by reducing the total pressure inside the sensor evaluation system and observing the sensor response to various CO concentrations from purchased, premixed gas tanks of CO in N_2. The pressures for these experiments were 87.5 kPa (4,000 feet altitude equivalent) and 75.3 kPa (8,000 feet altitude equivalent), respectively. The sensors were tested at reduced pressures in an effort to evaluate the sensor's performance in an environment similar to that which would be encountered in an aircraft cabin. In addition, the CO concentration and the corresponding pressure for each test were selected randomly to avoid any procedural bias in the experimental results. The 0 to 500 sccm MFC was used to control the flow of the N_2 purge gas as well as the CO in N_2 test gas. A list of the CO concentrations that were used is shown in Table 3.1 and a block diagram depicting the flow of the CO test gas is in Figure 3.7. The FTIR settings used for these experiments are in Table 3.3.

1. System was configured for operation of the sensor evaluation chamber in series with the FTIR gas analysis chamber.
2. System pressure was set to the appropriate value. The pressure was set to either 87.5 kPa (4,000 feet altitude equivalent) or 75.3 kPa (8,000 feet altitude equivalent).
3. System was purged with N_2 (NI CZ200) at a flow rate of 500 sccm for at least eight hours.
4. Flow of the CO test gas was set to 500 sccm.

5. Once the steady state concentration had been established (after approximately seven hours) a measurement was taken every ten minutes for the next three hours for a total of eighteen measurements.

Table 3.3
FTIR Settings for CO Sensor Experiments at Reduced Pressure

OPD Velocity	1 cm/s
Scan Range	2300 to 2000 cm^{-1}
Resolution	0.5 cm^{-1}
# of Scans	52

Experimental Procedure to Evaluate the Repeatability of the Carbon Monoxide Sensors

The ability of the CO sensors to provide reliable, stable and repeatable output for the same CO test gas input was studied. Due to logistical reasons, it was decided that only those sensors which were capable of automatic data logging would be the focus of these experiments. As a result, the sensors that were evaluated in this set of experiments were the e2v, GrayWolf and all three Figaro 5042 sensors. The experiment consisted of three cycles of filling the sensor evaluation chamber with a single, known CO gas concentration and then purging the system of the CO test gas with N_2.

Additionally, the influence of O_2 on the stability and repeatability of the CO sensors was examined. A tank of pure O_2 (OX UPC300) was purchased from Airgas, Inc. and was used in these experiments. The O_2 was mixed with both the N_2 purge gas and the CO in N_2 test gas to produce a gas mixture that was 21% O_2 and 79% the purge or test gas which is comparable to the amount of O_2 in the atmosphere (21% O_2). Figure 3.8 presents a block diagram depicting the experimental setup for the

repeatability experiments, and Table 3.4 presents a list of the experimental parameters for each experiment performed. For the experiments with O_2, a rotameter style flow controller (03SA, Omega Engineering, Inc., Stamford, CT, USA) was used to control the flow of the N_2 purge gas and the CO in N_2 test gas, while the 0 to 500 sccm MFC was used to control the flow of the O_2 gas. The FTIR was not used for these experiments, and only those sensors which had automatic data logging were examined (Figaro 5042, e2v, GrayWolf).

1. System was configured for operation of the sensor evaluation chamber only.
2. System pressure was set to the appropriate value. The pressure was set to either 101.3 kPa or 75.3 kPa (8,000 feet altitude equivalent).
3. When O_2 was used in the experiment, the flow rate of O_2 (OX UPC300) was set to 133 sccm, and it ran continually for the duration of the experiment.
4. System was purged with N_2 (NI R300) at a flow rate of 500 sccm (approximately 68 mm on the 03SA rotameter) for at least eight hours.
5. The flow rate of the CO test gas was set to 500 sccm (approximately 68 mm on the 03SA rotameter), and it was run for ten hours.
6. Steps 4 and 5 were performed a total of three times.
7. System was purged with N_2 (NI R300) at a flow rate of 500 sccm (approximately 68 mm on the 03SA rotameter) for at least eight hours.

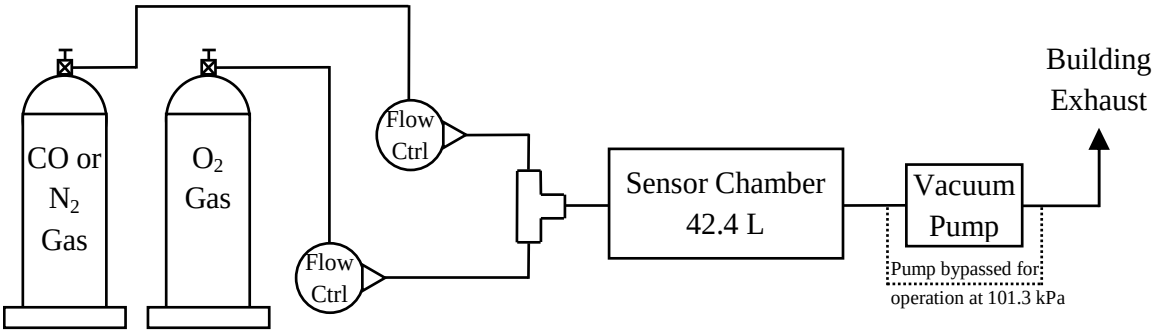

Figure 3.8: Block diagram depicting the flow of the N_2 purge gas, CO test gas and O_2 gas for the repeatability experiments with O_2.

Table 3.4
Experimental Parameters for Repeatability Experiments[†]

Source Concentration (ppm CO)[‡]	**System Pressure (kPa)**	**Oxygen**
253.6	101.3	No
253.6	101.3	Yes
49.60	101.3	Yes
49.60	75.3	Yes

[†] Experiments are listed in the order in which they were performed.
[‡] As certified by Airgas, Inc. at 101.3 kPa (1 atm)

FTIR Measurement Methods

It was obviously necessary for the FTIR to be calibrated to ensure accurate and repeatable results. All FTIR calibration experiments were conducted by acquiring a FTIR spectrum measurement from a known CO gas concentration with the FTIR. Then a quantitative CO concentration was obtained with QASoft® from the measured FTIR spectrum. There were a total of two FTIR calibration experiment sets. In each set of FTIR calibration experiments the FTIR was used to measure the seven known CO concentrations listed in Table 3.5.

Table 3.5
Carbon Monoxide Concentrations for FTIR Calibration

Target Concentration (ppm CO)	Actual Concentration (ppm CO)†	Error†	Standard
18	18.00	± 1%	Primary
50	49.40	± 2%	Certified
70	69.91	± 1%	EPA Protocol
100	100.0	± 1%	Primary
150	149.0	± 2%	Certified
250	251.9	± 1%	EPA Protocol
800	799.9	± 1%	Primary

† As certified by Airgas, Inc. at 101.3 kPa (1 atm)

Before every experiment the system was purged with N_2 to eliminate the common atmospheric gasses from the system such as CO_2 and H_2O, but even this did not completely purge these atmospheric gases out of the system. The presence of these gases could potentially negatively affect the ability of the FTIR to measure the CO spectrum, as discussed in Chapter 2. In light of this, the FTIR was operated by taking a background scan after the system was purged with N_2. Then, after the CO was flowing, a ratio scan was performed for each FTIR sample scan. The ratio scan allowed for the effects of the interfering atmospheric gases on the measurement spectrum to be eliminated by displaying only those parts of the measurement spectrum that were different from the background scan spectrum.

Experimental Procedure for FTIR Calibration Experiments

The FTIR calibration was conducted with the CO test gas flowing directly into the FTIR gas analysis chamber to isolate the FTIR and to minimize system leaks. By minimizing the system leaks the dilution of the CO test gas inside the system by the laboratory room air was also minimized. CO concentrations from purchased, premixed

tanks of CO in N_2 were used in the calibration of the FTIR. A list of the CO concentrations that were used is in Table 3.5 and a block diagram depicting the flow of the CO test gas is shown in Figure 3.9. The FTIR calibration was conducted at 101.3 kPa (1 atm) and the FTIR settings used for these experiments are in Table 3.6. A rotameter style flow controller (03SA, Omega Engineering, Inc., Stamford, CT, USA) was used to control the flow of the N_2 purge gas and the CO test gas through the FTIR gas analysis chamber.

1. The flow rate of the N_2 purge gas was set to 1000 sccm (approximately 135 mm on the 03SA rotameter).
2. After the system was purged (approximately 75 minutes) the input of the rotameter was switched to the CO test gas.
3. The flow rate of the CO test gas was set to 1000 sccm (approximately 135 mm on the 03SA rotameter).
4. Once the steady state CO concentration inside the system was reached, ten measurements of the CO test gas with the FTIR were taken.

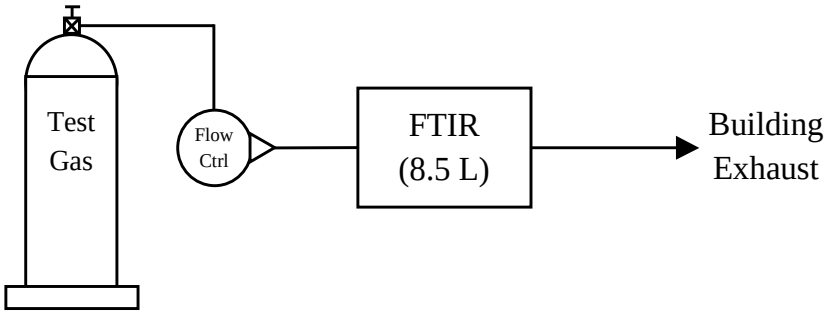

Figure 3.9: Block diagram depicting the flow of the CO test gas for the FTIR calibration experiments.

Table 3.6
FTIR Settings for FTIR Calibration Experiments

OPD Velocity	1 cm/s
Scan Range	2300 to 2000 cm^{-1}
Resolution	0.5 cm^{-1}
# of Scans	32

This procedure was performed twice for all seven CO test gases listed in Table 3.5. All of the FTIR steady state measurements were reported as the average of all the steady state measurements with plus and minus one standard deviation (1σ). From these data a FTIR calibration equation was acquired by plotting the known gas concentration of CO test gas versus the FTIR steady state measurements and determining a curve of best fit. The FTIR calibration equation enabled the FTIR measurements to be correlated with the actual test gas concentrations.

Carbon Monoxide Sensors

Commercially available CO sensors were purchased for use in this study. A total of ten individual sensors were tested from eight different manufacturers, with three of these sensors being the Figaro TGS-5042-A00. These three sensors are distinguished by their physical position inside the sensor evaluation chamber and are labeled as follows: Figaro 5042 (Top), Figaro 5042 (Mid) and Figaro 5042 (Bot). Table 3.7 lists the sensors that were examined along with technical specifications acquired from the manufacturers' datasheets and application notes for each sensor [56, 60–69]. All of the sensors were turned on and exposed to the room air for four days prior to any of the tests performed in this study.

Table 3.7
List of CO Sensors and Specifications

Manufacturer	Automation Components, Inc. (ACI)	CO Guardian LLC	e2v Technologies	Figaro USA, Inc.
Model Number	A/CP-R-D	Aero-551	EC4-2000-CO	TGS 5042-A00
Technology	Wall-mount Electrochemical	Cockpit panel-mount Electrochemical	Discrete Electrochemical	Discrete Electrochemical
Measurement Range	0 to 125 ppm (standard) 0 to 250 ppm (maximum)	10 to 999 ppm	0 to 2000 ppm	0 to 10,000 ppm
Accuracy	± 2.5% of reading			
Operating Range	-20 to 40°C (-4 to 104° F) 15 to 90% RH 0 to 99% intermittent	0 to 50°C (32 to 122° F) 10 to 90% RH	-20 to 50°C (-4 to 122° F) 15 to 90% RH	-10 to 60 °C (14 to 140 °F) 5 to 99% RH
Lifetime	2 to 3 years	5 years	2 years	
Response Time	< 60 sec for a typical 90% step change		T_{90} = < 1 min	T_{90} = < 1 min

Table 3.7
List of CO Sensors and Specifications (Continued)

Manufacturer	First Alert, Inc.	GrayWolf Sensing Solutions	Kidde	Sense Air, AB
Model Number	CO410	IQ-604	KN-COPP-B	aSENSE™ mIII
Technology	Wall-mount Electrochemical	Handheld Electrochemical	Wall-mount Electrochemical	Wall-mount Electrochemical
Measurement Range		0 to 500 ppm	11 to 999 ppm	0 to 100 ppm (standard) 100 to 500 ppm (extended)
Accuracy		± 2 ppm < 50 ppm ± 3% of reading > 50 ppm	+ 20% of reading + 15 ppm	± 10 ppm (standard) ± 20% of reading (extended)
Operating Range	4 to 38 °C (40 to 100 °F)	-15 to 70 °C (5 to 158 °F) 0 to 98% RH	4.4 to 38.7 °C (40 to 100 °F) up to 95% RH	
Lifetime	7 year limited warranty		7 years (replace)	> 5 years
Response Time		T_{90} = < 1 min		

Figaro TGS-5042-A00 is a discreet CO sensor and was operated using the manufacture's evaluation module (COM5042, Figaro USA, Inc., Arlington Heights, IL, USA). Each Figaro 5042 sensor is calibrated at the factory and shipped with the individual sensor's sensitivity printed on the outside of the sensor housing in units of picoamperes per ppm CO; Table 3.8 lists the sensitivity for each Figaro 5042 sensor tested. The output of the COM5042 module was a voltage that was then converted into the measured CO concentration. The COM5042 datasheet provided the equation, as shown in Equation 3.16, by which the output current of the sensor could be calculated from the measured output voltage of the evaluation module [65].

$$I_{out} = \frac{(V_{out} - 1)}{3.13} \tag{3.16}$$

where:

I_{out} = Sensor output current (μA)
V_{out} = Output voltage of module (V)

Equation 3.17 is then used to calculate the measured CO concentration using the result of Equation 3.16.

$$C = \frac{I_{out}}{S} \tag{3.17}$$

where:

C = Sensor measured CO concentration (ppm CO)
S = Sensitivity of individual sensor (μA/ppm CO)

Combining Equation 3.16 and Equation 3.17 gives the overall relationship between the COM5042 module output voltage and the sensor measured CO concentration, as shown in Equation 3.18.

$$C = \frac{\left(\frac{V_{out} - 1}{3.13}\right)}{S} = \frac{(V_{out} - 1)}{3.13 \cdot S} \tag{3.18}$$

Equation 3.19 provides a sample calculation of the sensor measured CO concentration for the Figaro 5042 (Top) with an output voltage of 2 V (V_{out} = 2 V).

$$C = = \frac{(V_{out} - 1)}{3.13 \cdot S} = \frac{(2 - 1)}{3.13 \cdot \left(1.682 \ x \ 10^{-3}\right)} = 190 \ \ ppm\ CO \tag{3.19}$$

Table 3.8
Sensitivity of Figaro TGS 5042 Sensors

Sensor	**Sensitivity (pA/ppm CO)**	**Sensitivity (µA/ppm CO)**
Figaro TGS 5042 (Top)	1682	1.682×10^{-3}
Figaro TGS 5042 (Mid)	1550	1.550×10^{-3}
Figaro TGS 5042 (Bot)	1659	1.659×10^{-3}

The e2v EC4-2000-CO is also a discreet CO sensor and the manufacture's evaluation kit (ECVQ-EK3, e2v Technologies, Chelmsford, Essex, England) was used to operate the sensor and to collect its data output. The e2v required calibration in order to operate properly. This calibration required two data points; one data point in a CO free environment, and the other in an environment which contained a nonzero amount of CO. The following procedure given by the manufacture was performed for this calibration:

1. Pure N_2 was applied to the e2v sensor
2. In the data acquisition software under the Electrochemical tab, the Set Zero button was pressed.
3. 149.0 ppm CO at 101.3 kPa was applied to the e2v sensor

4. After the system reached steady state (approximately seven hours) the new calibration gas concentration of 150 ppm CO was entered in the data acquisition software and the Measure Sensitivity button was pressed.

Additionally, the Kidde and the FirstAlert sensors did not display a CO concentration if the measured value was below 30 ppm CO. Therefore, readings below 30 ppm CO for these sensors were considered invalid and were not used in any curve fits or data analysis. The manufactures of these sensors intentionally designed the sensors to perform in this way in order to comply with the requirements set by Underwriters Laboratories, Inc [9].

Unit Conversion and Leak Rate Quantification

For simplicity and clarity, all of the CO concentrations, including the concentration of the CO gas tanks, were converted into and reported in units of milligrams of CO per cubic meter. This allows the concentration values to be reported explicitly as mass per volume and eliminates any confusion with attempting to determine the parts per million of CO inside the system at different total pressures. The conversion of ppm CO to mg CO/m^3 is given in Equation 3.20 and was adapted from the conversion given in the 2005 ASHRAE Handbook - *Fundamentals* [70].

$$C_{mg/m^3} = \frac{C_{ppm} P_{sys} M}{RT} \tag{3.20}$$

where:

C_{mg/m^3} = Concentration of CO (mg CO/m^3)
C_{ppm} = Concentration of CO (ppm CO)
P_{sys} = Pressure inside the system (kPa)
M = Molar mass of CO (28.0101 g/mol)
R = Universal gas constant (8.3145 m^3·Pa/mol·K)
T = Temperature of the gas (293 K)

Equation 3.21 shows an example of 149.0 ppm CO at 101.3 kPa converted into mg CO/m^3.

$$C_{mg/m^3} = \frac{C_{ppm} P_{sys} M}{RT} = \frac{(149.0\ \ ppm\ CO)(101.3\ \ kPa)\left(28.0101\ \ \frac{g}{mol}\right)}{\left(8.3145\ \ \frac{m^3 \cdot Pa}{mol \cdot K}\right)(293\ \ K)} \tag{3.21}$$

$$= 174.5\ \ \frac{mg\ \ CO}{m^3}$$

Additionally, room air leaked into the sensor evaluation system for the experiments performed at the pressures of 87.5 and 75.3 kPa, respectively, which resulted in the CO test gas concentration being diluted. In order to determine the final, steady sate concentration using the analytical model, the leak rate of room air entering the system must be known for each system pressure that was used. The leak rate of room air into the sensor evaluation system was experimentally determined by the following procedure:

1. System was configured for operation of the sensor evaluation chamber in series with the FTIR gas analysis chamber. Total volume, V, of 50.9 liters (0.0509 m^3).

2. The inlet of the sensor evaluation system was closed
3. System pressure was set to the appropriate value. The pressure was set to either 87.5 kPa (4,000 feet altitude equivalent) or 75.3 kPa (8,000 feet altitude equivalent).
4. The outlet of the sensor evaluation system was closed
5. The amount of time, Δt, it took for the pressure inside the sensor evaluation system to increase 0.65 kPa (~200 feet altitude equivalent), ΔP, was measured.
6. Equation 3.22 was used to determine the leak rate, $\dot{m}_{leak}$, of room air into the sensor evaluation system.

$$\dot{m}_{leak} = \left(\frac{\Delta P}{P_{atm}}\right)\left(\frac{V}{\Delta t}\right) \tag{3.22}$$

where:

$\dot{m}_{leak}$ = Leak rate of room air into the sensor evaluation system (sccm)
ΔP = Change in the pressure of the sensor evaluation system (0.65 kPa)
P_{atm} = Atmospheric pressure inside the room (101.3 kPa)
V = Volume of the sensor evaluation system (cm^3)
Δt = Duration over which ΔP is measured (min)

This procedure was performed three times for each pressure with the final leak rate being the average of the three individual results. A sample calculation for the determination of the leak rate at 87.5 kPa (4,000 feet altitude equivalent) is given in Equation 3.23.

$$\begin{aligned}\dot{m}_{leak} &= \left(\frac{\Delta P}{P_{atm}}\right)\left(\frac{V}{\Delta t}\right) = \left(\frac{88.15\ kPa - 87.50\ kPa}{101.3\ kPa}\right)\left(\frac{50{,}900\ cm^3}{33\ \text{min}}\right) \\ &= \left(\frac{0.65\ kPa}{101.3\ kPa}\right)\left(\frac{50{,}900\ cm^3}{33\ \text{min}}\right) = 9.9\ sccm = 10\ sccm\end{aligned} \tag{3.23}$$

Having completed this procedure the leak rate for a system pressure of 87.5 kPa was determined to be 9 sccm, and a leak rate of 15 sccm was determined for a system pressure of 75.3 kPa.

The final, steady state CO concentration for each experiment was determined by the analytical model (Equation 3.14 and Equation 3.15). The model was used to determine the steady state CO concentration to which the sensors were exposed, herein referred to as the "known gas concentration". Table 3.9 summarizes the known gas concentrations used in this study and demonstrates their relationship to the CO test gas source for the CO sensor experiments. Table 3.9 also correlates the known gas concentrations to the experimentally obtained steady state measurements of the FTIR. Table 3.10 summarizes the relationship between the known CO gas concentration and the CO test gas source for the repeatability experiments.

Table 3.9
CO Concentrations for CO Sensor Experiments

CO Test Gas Concentration (Source)			FTIR Steady State Measurements[‡] (mg CO/m^3)			Model Steady State Concentration[§] (Known Gas Concentration) (mg CO/m^3)		
Requested (ppm CO)	Actual[†] (ppm CO)	Actual (mg CO/m^3)	101.3 kPa no leak	87.5 kPa 9 sccm	75.3 kPa 15 sccm	101.3 kPa no leak	87.5 kPa 9 sccm	75.3 kPa 15 sccm
18	18.00 ± 1%	21	21 ± 3%	16 ± 4%	17 ± 4%	21	15	11
50	49.40 ± 2%	58	58 ± 2%	38 ± 2%	27 ± 3%	58	42	31
100	100.0 ± 1%	116	114 ± 1%	89 ± 1%	54 ± 2%	116	85	62
150	149.0 ± 2%	174	173 ± 1%	124 ± 1%	88 ± 1%	174	127	93
250	251.9 ± 1%	293	301 ± 1%	194 ± 1%	138 ± 1%	293	215	157

[†] As certified by Airgas, Inc. at 101.3 kPa (1 atm) with the values reported as the measured CO concentration ± the analytical uncertainty represented as a percentage of the measured value.
[‡] Values are reported as the mean value ± the standard error (1σ) represented as a percentage of the mean.
[§] Experiments were performed at 101.3 kPa (no leak), 87.5 kPa (F_{leak} = 9 sccm), and 75.3 kPa (F_{leak} = 15 sccm).

Table 3.10
CO Concentrations for Repeatability Experiments

CO Test Gas Concentration (Source)			Model Steady State Concentration‡ (Known Gas Concentration) (mg CO/m^3)		
Requested (ppm CO)	Actual (ppm CO)†	Actual (mg CO/m^3)	101.3 kPa no dilution	101.3 kPa 133 sccm	75.3 kPa 148 sccm
50	49.60 ± 2%	58	–	45	33
250	253.6 ± 1%	295	295	233	–

† As certified by Airgas, Inc. at 101.3 kPa (1 atm) with the values reported as the measured CO concentration ± the analytical uncertainty represented as a percentage of the measured value.
‡ Experiments were performed at 101.3 kPa without O_2 (no dilution), 101.3 kPa with O_2 (F_{leak} = 133 sccm), and 75.3 kPa with O_2 (F_{leak} = 15 sccm + 133 sccm = 148 sccm).

The steady state concentrations at the reduced pressures (87.5 and 75.3 kPa) were lower than the steady state sea level concentration due to the following two reasons: First, the amount of the CO test gas that can be supported inside of the system decreases as the pressure decreases according to Dalton's Law. Second, the CO test gas was diluted by the leaking of room air into the system. The following is an extended example calculation which demonstrates the process by which the known gas concentration was determined given a source concentration of 49.40 ppm CO and a system pressure of 75.3 kPa:

First, 49.40 ppm CO was converted into units of mg CO/m^3, as shown in Equation 3.24, using Equation 3.20.

$$C_{mg/m^3} = \frac{C_{ppm} P_{sys} M}{RT} = \frac{(49.40\ \ ppm\ \ CO)(75.3\ \ kPa)\left(28.0101\ \ \frac{g}{mol}\right)}{\left(8.3145\ \ \frac{m^3 \cdot Pa}{mol \cdot K}\right)(293\ \ K)} \qquad (3.24)$$

$$= 42.8\ \ \frac{mg\ \ CO}{m^3}$$

The result of Equation 3.24, $C_{mg/m^3} = 42.8\ \ \frac{mg\ CO}{m^3}$, was then used as the input concentration, Cs, into the analytical model (Equation 3.14). Given a leak rate of 15 sccm, the input and output flow rates of 500 sccm each, a system pressure of 78.3 kPa, and a chamber volume of 0.0424 m^3 the analytical model becomes Equation 3.25.

$$C_{CO}(t) = \left(\frac{1}{1+\frac{F_{leak}}{F_i}}\right)\left(\frac{C_s * P_{sys}}{P}\right)\left[1 - e^{\frac{-F_o \cdot t}{Vol_{chamber}\left(\frac{P}{P_{sys}}\right)}}\right] \qquad (3.25)$$

$$= \left(\frac{1}{1+\frac{15}{500}}\right)\left(\frac{42.8 * 75.3}{101.3}\right)\left[1 - e^{\frac{-500 \cdot t}{0.0424\left(\frac{101.3}{75.3}\right)}}\right]$$

As steady state was approached ($t \rightarrow \infty$) the exponential function in Equation 3.25 approaches zero, as shown in Equation 3.26.

$$for\ t \rightarrow \infty; \quad e^{\frac{-F_o \cdot t}{Vol_{chamber}\left(\frac{P}{P_{sys}}\right)}} = e^{\infty} = 0 \qquad (3.26)$$

Finally, Equation 3.26 was used to simplify Equation 3.25 resulting in Equation 3.27 which is equal to the known gas concentration as determined by the analytical model.

$$C_{CO}(t) = \left(\frac{1}{1+\frac{15}{500}}\right)\left(\frac{42.8*75.3}{101.3}\right) = 30.89 = 31 \ \frac{mg\ CO}{m^3} \tag{3.27}$$

Chapter 4: Results and Discussion

FTIR Calibration

Theoretically, CO should exhibit a linear relationship between the IR energy absorbed and the CO concentration following the Beer-Lambert Law (Equation 2.3), but it was difficult to observe this experimentally. Instead, the FTIR measurements obtained for CO showed nonlinear behavior as well as scatter in the steady state measurements. In fact, as the CO concentration increased the non-linearity (deviation from the Beer-Lambert Law) also increased, as shown in Figure 4.1, yet the variation from the average steady state value, presented as the 95% confidence level, showed to be independent of the concentration as seen in Table 4.1. Interestingly, it is not uncommon to observe a nonlinear relationship between the IR energy absorbed and the component's concentration at high concentrations. This was accounted for by means of calibrating the FTIR [43, 71]. The experimental uncertainty and scatter in the data points were addressed by increasing the number of measurements and by increasing the number of interferometer scans per measurement.

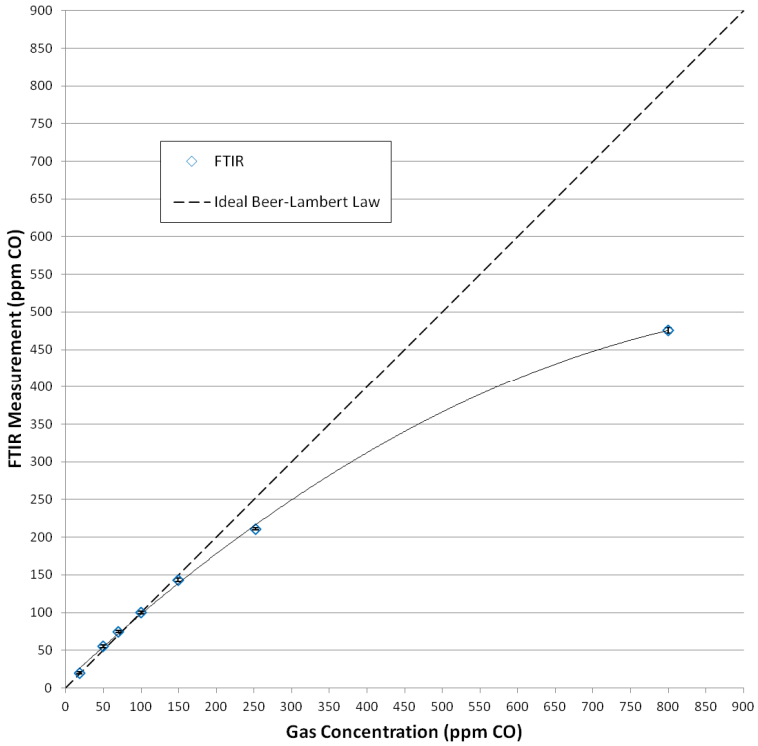

Figure 4.1: Comparison of the experimental FTIR CO measurements to the theoretical Beer-Lambert Law. The data is presented as the mean steady state value ± 1σ. The calibration was performed at 101.3 kPa (1 atm).

Table 4.1
FTIR Measurement Statistics[†‡]

CO Concentration:	18.0	49.4	69.9	100	149	252	800
Average	19.3	42.6	76.8	108	143	205	476
Confidence Level (95.5%)	3.9	2.4	3.7	2	3	4	4
Range	18.7	13.3	22.9	9	14	17	15

[†] All values are given in ppm CO
[‡] Presented data from the second FTIR calibration experiment (101.3 kPa)

The FTIR calibration was performed in order that the nonlinearity might be quantified and that its measurements would be reliably correlated to the known gas concentration of the CO test gasses. This was done per the procedures laid out in the

FTIR Measurement Methods portion of Chapter 3, and the results are presented in Figure 4.2.

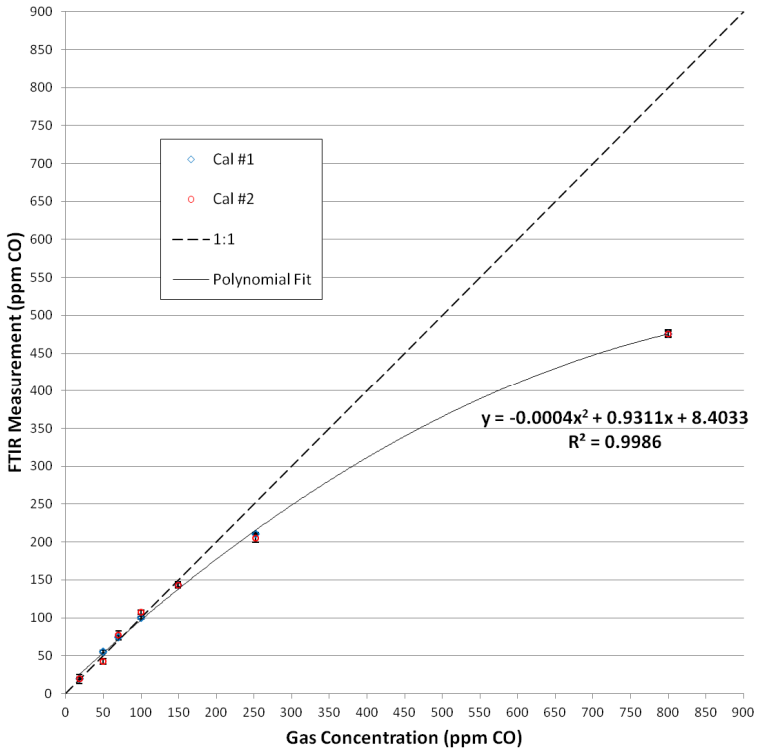

Figure 4.2: Combination of the data from both FTIR calibration experiment sets. FTIR measurements are plotted versus the known gas concentration of the CO test gas. The curve of best fit incorporates the average of all the data points from both calibrations for every concentration. The data is presented as the mean steady state value ± 1σ. The calibration was performed at 101.3 kPa (1 atm).

However, it was more convenient in later experiments for the FTIR measurements to be plotted as the independent variable, as shown in Figure 4.3. This allowed the curve of best fit to be the equation that corrected the FTIR measurements to the actual CO test gas concentrations. This equation was named the FTIR calibration equation and is presented in Equation 4.1.

$$y = 0.0019x^2 + 0.7876x + 1.6715 \quad (4.1)$$

where:

x = FTIR measurement (ppm CO)

y = Corrected FTIR measurement (ppm CO)

The FTIR calibration equation gives the concentration in units of ppm CO and which can be converted into units of mg CO/m^3 using Equation 3.20.

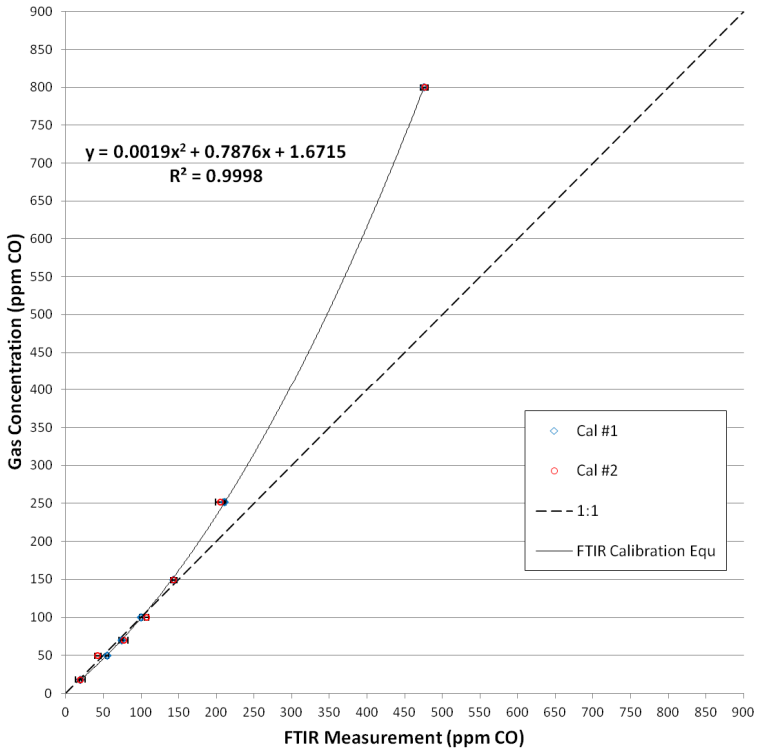

Figure 4.3: Combination of the data from both FTIR calibration experiment sets. The known concentrations of the CO test gas are plotted versus the FTIR measurements. The curve of best fit incorporates the combined data from both calibration runs and is called the FTIR calibration equation. The data is presented as the mean steady state value ± 1σ. The calibration was performed at 101.3 kPa (1 atm).

Premixed Carbon Monoxide Gas Experiments

The CO sensors listed in Table 3.7 were exposed to five CO source concentrations at three total pressures with the known CO gas concentration for each experiment listed in Table 3.9. The commercial CO sensors were evaluated for both their steady state and transient response.

Carbon Monoxide Sensor Performance

Steady State Analysis

The CO sensors were first tested with a system pressure of 101.3 kPa (1 atm). In light of the fact that most of these sensors were designed to operate in a residence or office building, an initial system pressure of 101.3 kPa was chosen in an attempt to evaluate the sensors in an environment most similar to that for which they were designed. At this pressure the sensors were exposed to CO concentrations of 21, 58, 116, 174 and 293 mg CO/m^3. Figure 4.4 plots the results from these experiments as the sensor measured CO concentration versus the known CO gas concentration. The steady state value for each sensor was determined by the mean of eighteen measurements taken when the sensor evaluation system was at a steady state CO concentration.

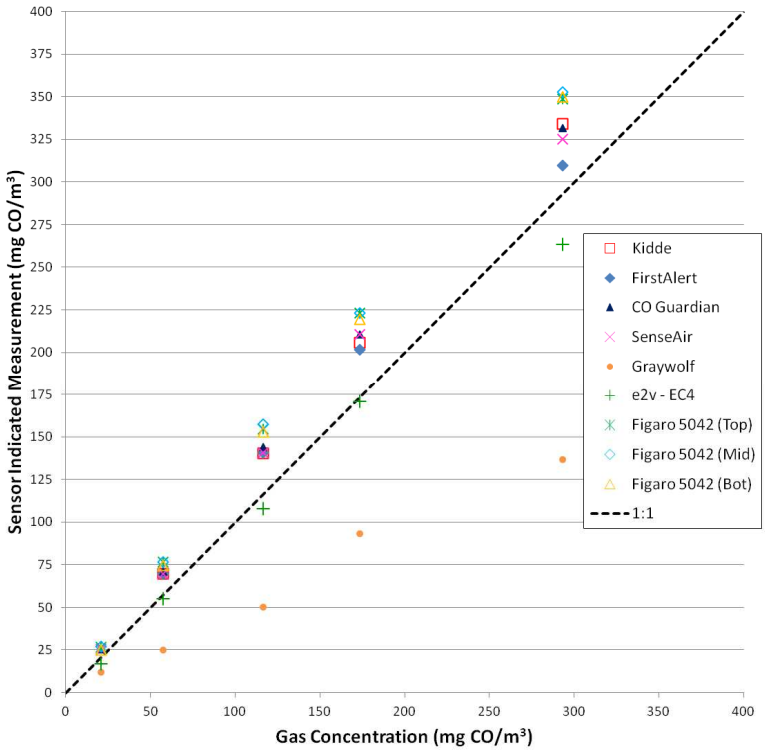

Figure 4.4: Steady state results for CO sensor evaluation at 101.3 kPa.

Figure 4.4 enables the sensor's performance to be evaluated based on the comparison of the CO concentration as measured by the sensors to the actual amount of CO to which the sensors were exposed. In the ideal case the sensors would output exactly the same CO concentration as the known gas concentration resulting in linear behavior as shown by the 1:1 line in Figure 4.4. This, however, did not happen as most of the sensors measured more CO inside the system than the actual known CO gas concentration. While this is somewhat disappointing, it is reasonable to think that the sensor manufacturer would intentionally overestimate the sensor measured CO concentration. By doing this, the manufacturer ensures that the sensor will never measure a CO concentration lower than that to which the sensor is exposed. Thus, the

possibility of the sensor not alarming when the CO concentration is at the alarm threshold is eliminated.

However, one consequence of overestimating the CO concentration is the possibility of false alarms where the sensor indicates an unsafe CO concentration but the actual CO concentration is still below the alarm threshold. False alarms are potentially very costly for commercial airline companies; therefore, the operation of any sensor that is used onboard commercial aircraft must be well understood so that the appropriate adjustments can be made, to avoid false alarms.

The GrayWolf sensor was the only sensor that consistently measured less CO inside the system than the known gas concentration. In addition, the e2v sensor was the most consistently accurate sensor for the experiments performed at 101.3 kPa. The ACI sensor's output was erratic and unusable. Throughout the experiments performed at 101.3 kPa, the ACI sensor consistently measured negative CO concentrations and displayed multiple faults and errors.

Even though the sensors generally did not accurately measure the exact amount of CO inside the system, each sensor demonstrated a linear response to an increase in the CO concentration. This suggests that these sensors could be recalibrated so that these sensors' output could be reliably correlated to the actual CO concentration.

After the sensors were evaluated at 101.3 kPa, a set of experiments were performed where the total pressure inside the sensor evaluation system was randomly alternated between 87.5 and 75.3 kPa. These two pressures were chosen because they will likely be encountered onboard a commercial airliner. 75.3 kPa (8,000 feet altitude equivalent) was chosen because it is the lowest pressure allowed onboard a commercial

aircraft at any time [10]. 87.5 kPa (4,000 feet altitude equivalent) was chosen because it corresponds to the pressure at the altitude which is halfway between sea level and 8,000 feet altitude.

The steady state results for the CO sensor experiments performed at total pressures of 87.5 and 75.3 kPa are presented in Figure 4.5 and Figure 4.6, respectively. These results show that the sensors demonstrated similar behavior at the reduced pressures as they did at 101.3 kPa. The sensors still exhibited a linear relationship between the measured CO concentration and the known gas concentration. Also, the sensors measured more CO inside the system than the known gas concentration of CO, just as they did during the 101.3 kPa experiments. Unfortunately, the GrayWolf sensor malfunctioned during the experiments at the lower pressures, as demonstrated by sensor output of 0 ppm CO for all of the experiments that were performed. In addition, the Kidde and the e2v sensors' output did not reliably stabilize during the experiments at the lower pressures, making steady state analysis at these pressures impossible. The ACI sensor's output was, again, erratic and unusable. Throughout the experiments performed at 87.5 and 75.3 kPa, respectively, the sensor consistently measured negative CO concentrations and displayed multiple faults and errors.

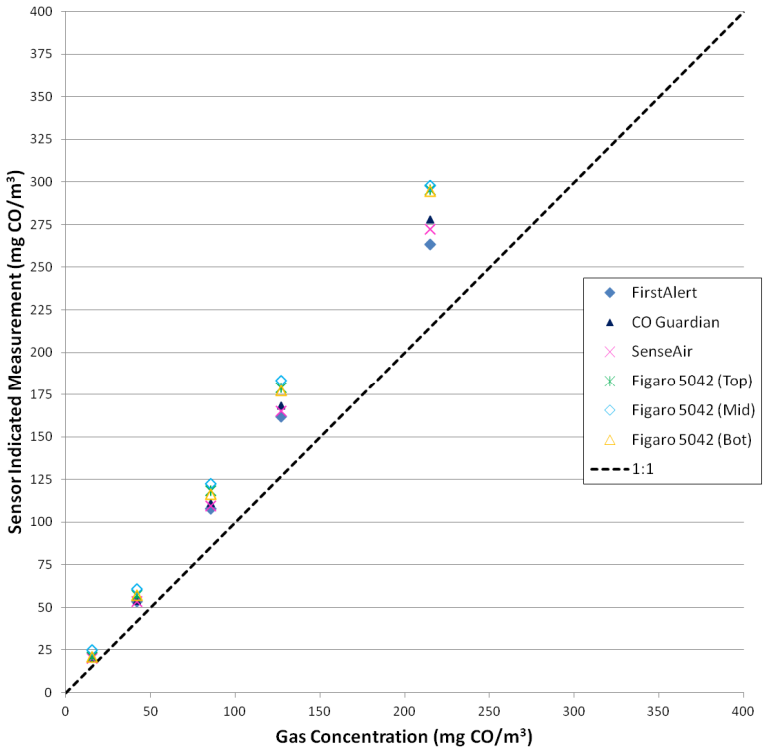

Figure 4.5: Steady state results for CO sensor evaluation at 87.5 kPa.

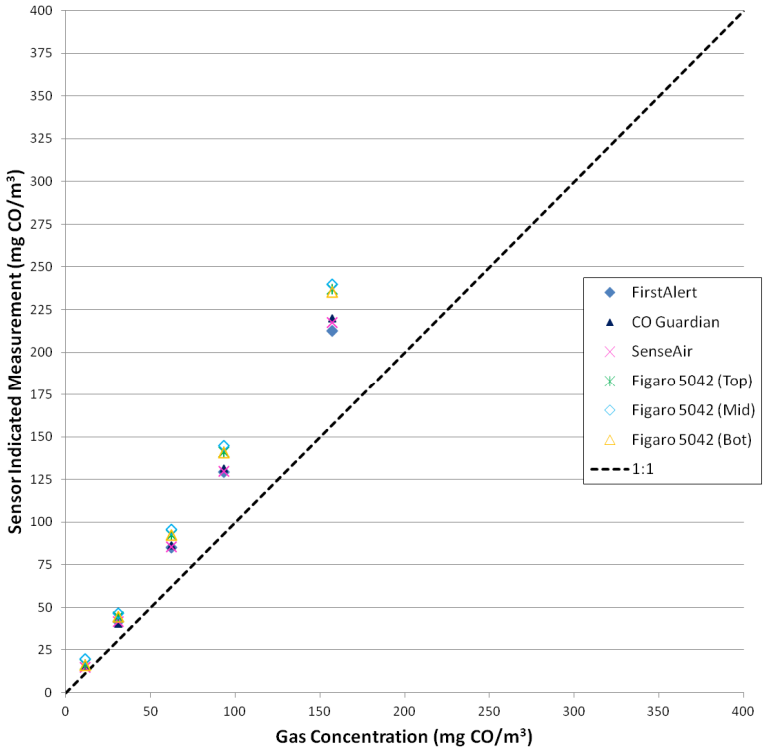

Figure 4.6: Steady state results for CO sensor evaluation at 75.3 kPa.

There was one significant difference between the sensors' response to different total pressures. As the pressure was reduced, the slope of the linear behavior of the sensors increased. This can be most clearly seen when the results from the experiments performed at all three pressures are plotted together for each individual sensor. Figure 4.7 presents a representative dataset for the top most Figaro 5042 sensor that demonstrates this behavior. The results for all of the individual sensors are presented in Appendix A. The increasing slope of the linear response to the increasing amount of CO suggests that the accuracies of the sensors decrease as the pressure decreases. However, the sensors' behavior was linear and predictable, indicating that the sensors could be calibrated to accommodate changes in total pressure.

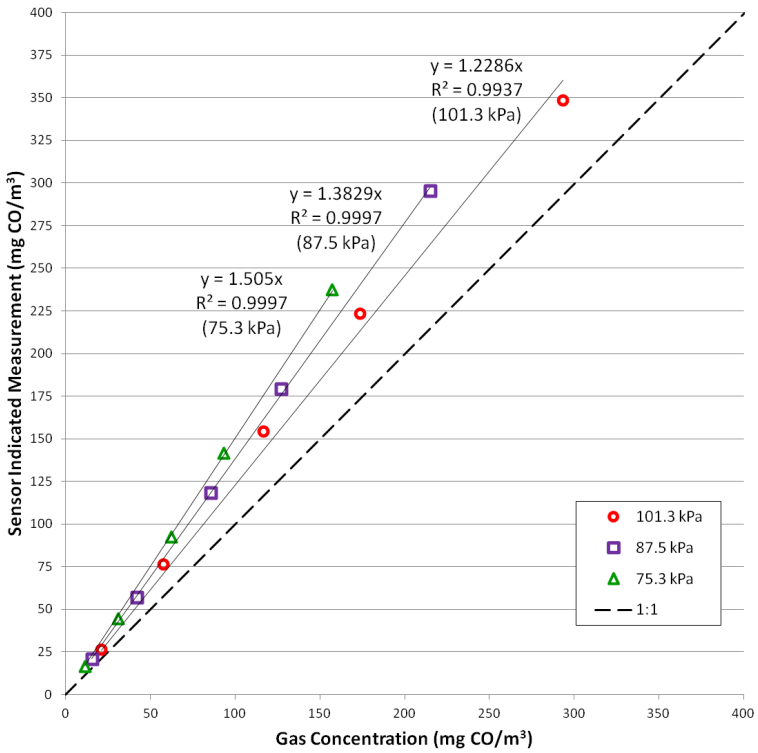

Figure 4.7: Figaro 5042 (Top) response at pressures of 101.3, 87.5 and 75.3 kPa

There was little variation in the sensors' measurements when the system was at steady state. For those sensors whose output stabilized the statistical uncertainties of the steady state, mean values were small. Table 4.2 shows the tabulated, mean steady state measurements for all of the sensors with the statistical uncertainty of each mean value for the experiments performed at 101.3 kPa. The statistical uncertainties in Table 4.2 are given as the standard error (1σ) of the mean value represented as a percentage of the mean. Table 4.2 shows that there is little change in the uncertainty of the mean steady state values of the sensors as the CO concentration increases. Appendix B contains the tabulated, mean steady state measurements acquired for each sensor at the total pressures of 101.3, 87.5 and 75.3 kPa, respectively.

Table 4.2
CO Sensor Output at 101.3 kPa[†‡]

	Carbon Monoxide Steady-State Concentration (mg CO/m^3)				
Sensors	21	58	116	174	293
ACI, A/CO-R-D	–	–	–	–	–
CO Guardian, Aero-551	25 ± 1%	71 ± 1%	144 ± 1%	211 ± 1%	331 ± 1%
e2v Tech, EC4-2000-CO	16.9 ± 0.3%	55.1 ± 0.1%	107.9 ± 0.1%	170.7 ± 0.1%	263.3 ± 0.1%
Figaro, TGS 5042 (Top)	26.7 ± 0.2%	76.5 ± 0.1%	154.5 ± 0.1%	223.4 ± 0.1%	348.7 ± 0.1%
Figaro, TGS 5042 (Mid)	26.9 ± 0.2%	76.7 ± 0.1%	157.3 ± 0.1%	223.3 ± 0.1%	352.8 ± 0.1%
Figaro, TGS 5042 (Bot)	24.9 ± 0.2%	74.6 ± 0.1%	153.1 ± 0.1%	219.4 ± 0.1%	349.8 ± 0.1%
First Alert, CO410	–	70 ± 1%	141 ± 1%	202 ± 1%	310 ± 1%
GrayWolf, IQ-610	12.1 ± 0.2%	24.9 ± 0.1%	50.3 ± 0.2%	93.4 ± 0.1%	136.9 ± 0.4%
Kidde, KN-COPP-B	–	70 ± 1%	141 ± 1%	206 ± 1%	334 ± 1%
Sense Air, aSENSE™ mIII	26 ± 1%	70 ± 1%	141 ± 1%	211 ± 1%	325 ± 1%

[†] Values reported as the mean ± the standard error (1σ) as a percentage of the mean
[‡] All mean values are given in mg CO/m^3

The sensors generally demonstrated more uncertainty in the mean steady state value at the lower CO concentrations than at the higher concentrations. This can be explained by the realization that, at the lower CO concentrations, the sensors' inherent errors and signal noises are a larger percentage of the overall sensor signal than they are at the higher concentrations. This fact results in larger variations, hence larger statistical uncertainties, in the sensors' steady state measurements for the measurements taken at lower CO concentrations when compared to the uncertainties at the higher concentrations.

Transient Analysis

The transient response of the CO sensors was also evaluated. This analysis evaluated the sensors' ability to properly measure the changing CO concentration inside the system. The sensors' transient response was analyzed in comparison to the response of the analytical model. Time constants, τ, were calculated for each sensor as well as the mathematical model using OriginPro8. In this study, τ represents the amount of time that it took for the CO concentration as measured by the sensors or as calculated by the model to reach approximately 63% of its final, steady state value. OriginPro8 was used to find a curve of best fit to the measurement versus time data for each sensor and the model. OriginPro8 was programmed to fit the experimental data to an exponential equation of the form given in Equation 4.2.

$$y = C\left[1 - \exp\left(\frac{-t}{\tau}\right)\right] \tag{4.2}$$

where:

y = CO concentration at time, t (mg CO/m^3)
C = Steady state CO concentration (mg CO/m^3)
t = duration of CO test gas flow (min)
τ = Time constant (min)

Figure 4.8 and Figure 4.9 present representative plots of the curve fits obtained from OriginPro8, while the time constants that were obtained for the experiments performed at 101.3 kPa are presented in Table 4.3. OriginPro8 also determined the standard error (1σ) of each time constant as well as the regression coefficient. This information is also presented in Table 4.3 for each time constant. Appendix C contains the time constants and regression coefficients for the experiments performed at 101.3, 87.5 and 75.3 kPa, respectively.

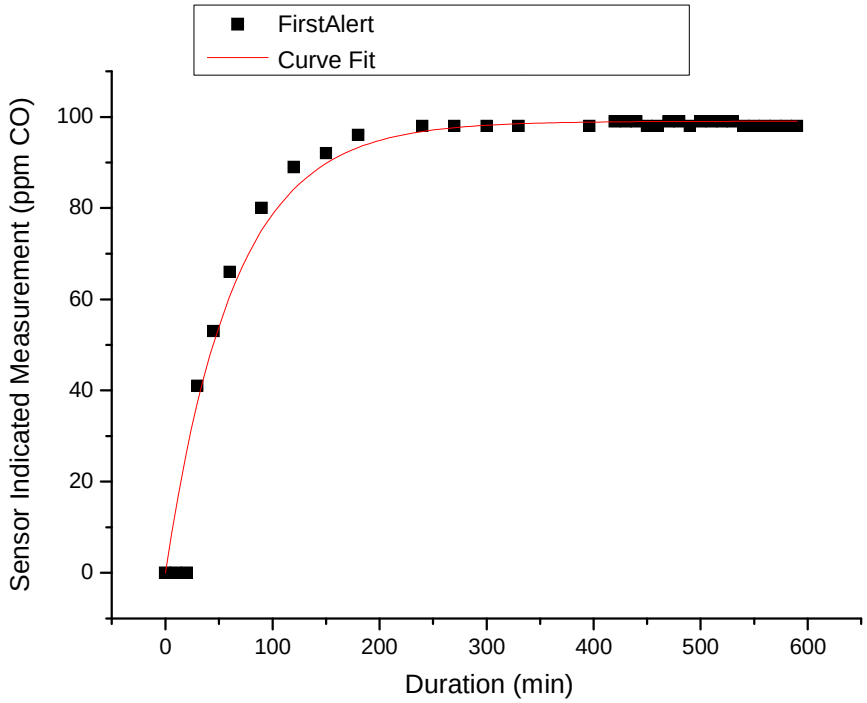

Figure 4.8: FirstAlert curve fit at 75.3 kPa and Cs = 100.0 ppm CO (116 mg CO/m^3).

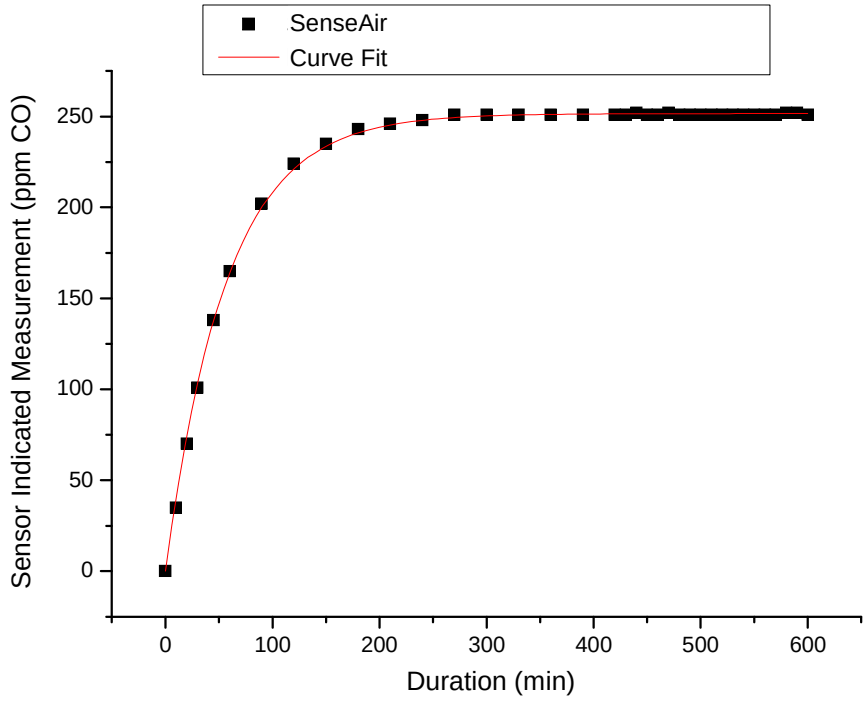

Figure 4.9: SenseAir curve fit at 75.3 kPa and Cs = 251.9 ppm CO (293 mg CO/m^3).

Table 4.3
Time Constants: 101.3 kPa[†‡]

	21.0 mg/m^3	R^2	57.5 mg/m^3	R^2	117 mg/m^3	R^2	174 mg/m^3	R^2	293 mg/m^3	R^2
Model (Sensor)	84.8 ± 0.0	1.00	84.8 ± 0.0	1.00	84.8 ± 0.0	1.00	84.8 ± 0.0	1.00	84.8 ± 0.0	1.00
Kidde	-	-	93.8 ± 7.4	0.92	84.7 ± 2.8	0.98	80.9 ± 1.6	0.99	74.1 ± 1.8	0.99
FirstAlert	-	-	80.5 ± 0.9	0.99	81.7 ± 1.4	0.99	81.8 ± 0.8	1.00	72.2 ± 2.5	0.98
CO Guard	86.5 ± 3.3	0.90	74.6 ± 1.5	0.99	76.0 ± 2.2	0.98	78.4 ± 1.3	0.99	67.3 ± 3.0	0.96
SenseAir	91 ± 1.9	0.99	77.6 ± 0.7	1.00	80.9 ± 1.1	1.00	83.8 ± 0.8	1.00	72.2 ± 2.7	0.98
GrayWolf	44.7 ± 0.2	0.90	1.8 ± 0.0	0.74	167.5 ± 4.7	0.89	149.6 ± 0.1	1.00	-	-
Fig 5042 (Top)	76.3 ± 0.1	0.99	76.3 ± 0.0	1.00	76.8 ± 0.3	0.99	75.2 ± 0.1	0.98	60.7 ± 0.9	0.88
Fig 5042 (Mid)	84.7 ± 0.1	0.99	72.9 ± 0.1	1.00	77.2 ± 0.2	0.99	76.2 ± 0.1	0.99	63.0 ± 0.7	0.92
Fig 5042 (Bot)	68.5 ± 0.1	0.98	74.8 ± 0.1	1.00	78.6 ± 0.3	0.99	77.2 ± 0.1	0.99	63.1 ± 0.7	0.91

[†] Time constants are presented in units of minutes as $\tau \pm$ the standard error (1σ)
[‡] Columns are labeled with the steady state CO concentration in units of mg CO/m^3

Table 4.3 shows that the predicted time constant for the mathematical model is similar to the time constants of the sensors. Since the time constants for the sensors are similar to that of the model, it can be concluded that the CO sensors are able to keep up with the increasing CO concentration and stabilize when the steady state concentration inside the system is reached. Table 4.3 also shows that there is no change in the transient behavior of the sensors as the known gas concentration is increased.

Appendix C contains the time constants for the experiments performed at 87.5 and 75.3 kPa, respectively. The sensors' ability to track the change of CO inside the sensor evaluation chamber was unchanged by a reduction in the total system pressure which shows that there is no change in the transient behavior of the sensors at the lower pressures.

To further illustrate the transient response of the sensors, the CO sensors' response was normalized to the analytical model, and the result was plotted versus time. Appendix D contains plots of the CO sensors' response normalized to the analytical model for all of the experiments performed at 101.3, 87.5 and 75.3 kPa. Figure 4.10 and Figure 4.11 show the transient behavior for the Figaro 5042 (Top) at 101.3 and 75.3 kPa. This data set is representative of the following sensors: FirstAlert, CO Guardian, SenseAir and all three of the Figaro sensors. Figure 4.10 and Figure 4.11 show that the Figaro 5042 (Top) has a quick response time when compared to the chamber filling response and that the transient response does not change with pressure or concentration.

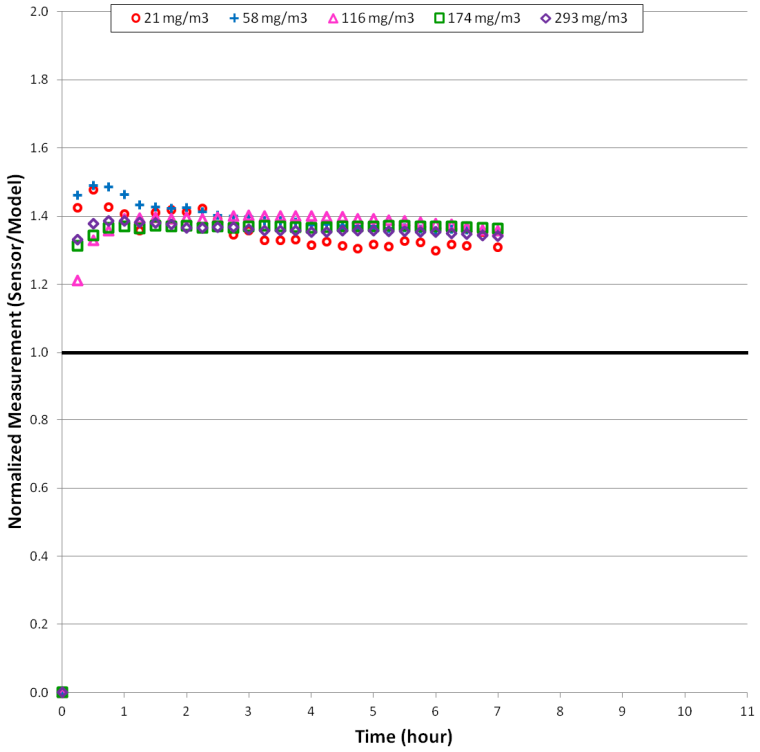

Figure 4.10: Figaro 5042 (Top) transient response for CO concentrations at 101.3 kPa.

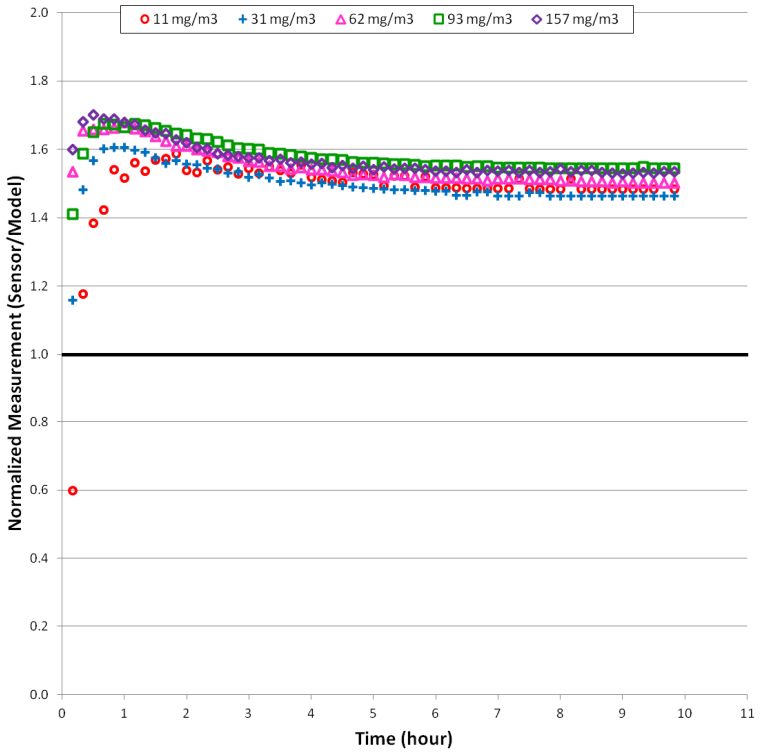

Figure 4.11: Figaro 5042 (Top) transient response for CO concentrations at 75.3 kPa.

In contrast, there were three sensors that exhibited unexpected behavior. As was mentioned previously, the GrayWolf sensor malfunctioned during the experiments at 87.5 and 75.3 kPa, therefore, transient analysis was unable to be performed for the GrayWolf sensor at these pressures. The Kidde sensor performed as expected at 101.3 kPa, and it demonstrated the ability to stabilize when the system had achieved steady state, as shown in Figure 4.12; however, the Kidde sensor demonstrated difficulty stabilizing at the lower pressures as shown in Figure 4.13. This seemed to be due to the fact that the sensor overshot the known gas concentration. The overshoot behavior of the Kidde sensor appeared to increase as the pressure decreased and the CO concentration increased.

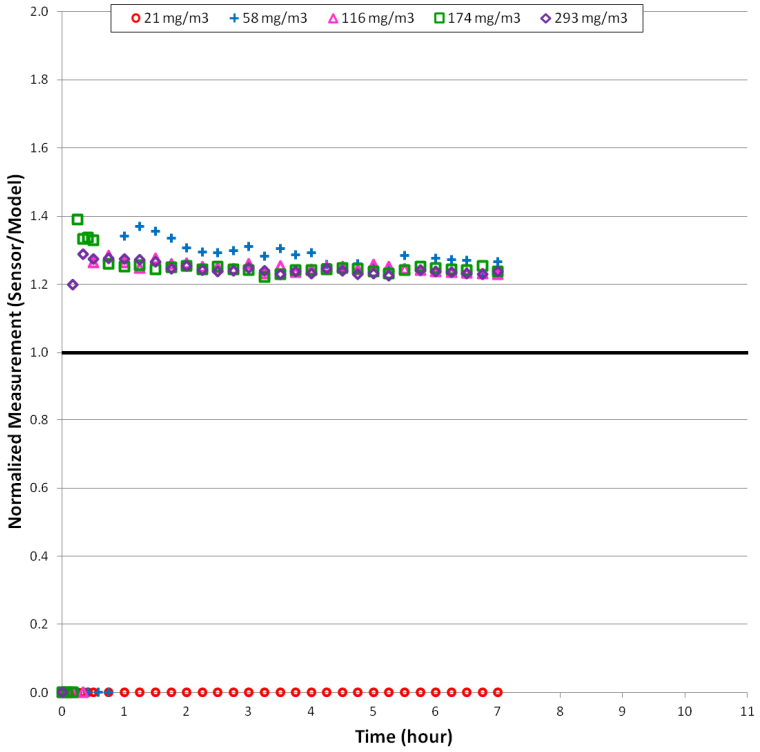

Figure 4.12: Kidde transient response for CO concentrations at 101.3 kPa.

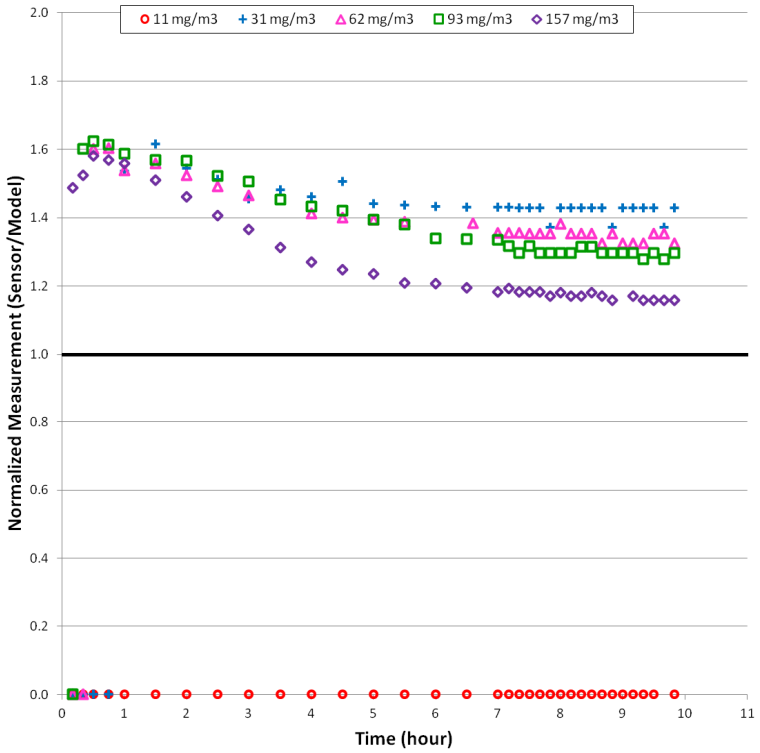

Figure 4.13: Kidde transient response for CO concentrations at 75.3 kPa.

Figure 4.14 presents the normalized transient data for the e2v sensor response at 101.3 kPa. The e2v sensor had a slow response time at the low concentration of 21 mg CO/m^3, but, at the high concentration of 293 mg CO/m^3 (251.9 ppm CO), the e2v sensor responded much faster, which indicates that its response time is dependent on the CO concentration. The e2v sensor demonstrated similar behavior at 75.3 kPa as it did at 101.3 kPa, as shown in Figure 4.15, by responding slowly at the low concentration and responding significantly faster at the high concentration. It should be noted that the experiments performed at 101.3 kPa had a duration of greater than twenty-four hours. The e2v sensor did eventually stabilize to a constant concentration over this time; however, this response time is too long considering that the duration of an average commercial airline flight is 1.5 hours [72]. When the e2v output did stabilize, it was the sensor that was in the best agreement with the analytical model.

The ACI sensor's output was unusable for transient analysis due to the sensor consistently measuring negative CO concentrations and displaying multiple faults and errors for the experiments performed at the pressures of 101.3, 87.5 and 75.3 kPa, respectively.

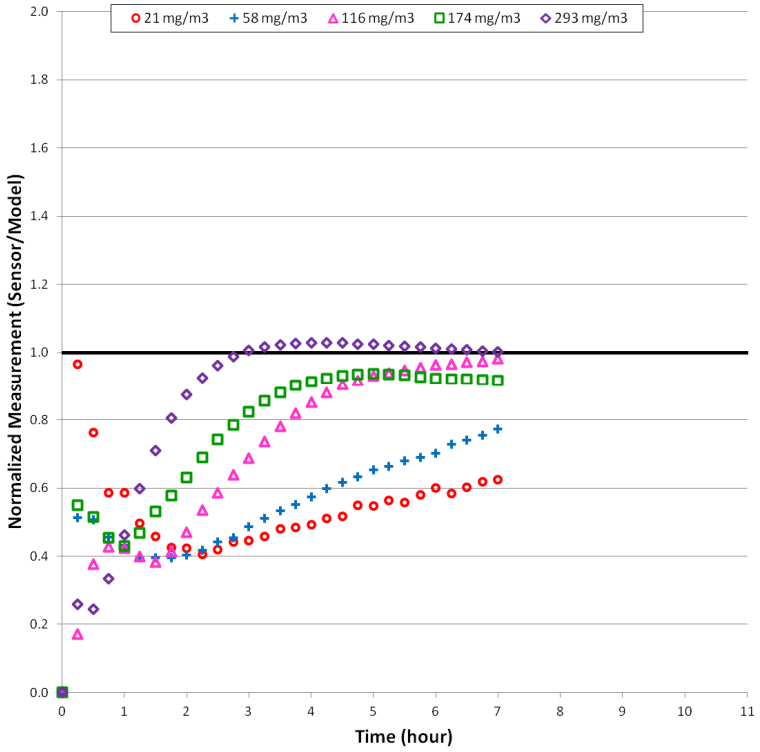

Figure 4.14: e2v transient response for CO concentrations at 101.3 kPa.

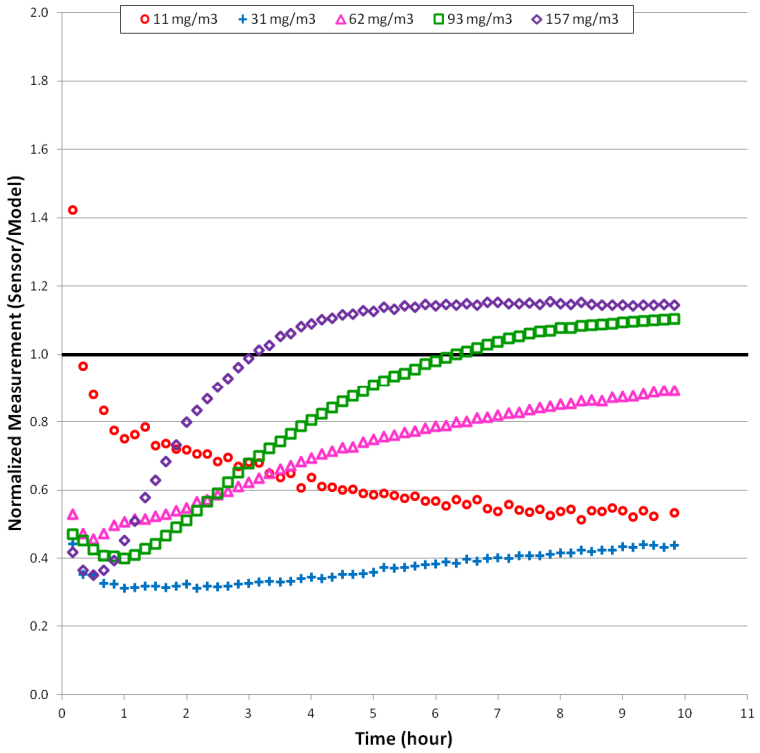

Figure 4.15: e2v transient response for CO concentrations at 75.3 kPa.

Repeatability Experiments

A set of experiments was performed to evaluate the stability and repeatability of select CO sensors' output. The first experiment was performed at a pressure of 101.3 kPa and had a steady state CO concentration of 295 mg CO/m^3 with the results presented in Figure 4.16. The overall observation from this experiment was that the sensors exhibited erratic second order responses over the course of the three cycles, as shown in Figure 4.16. The Figaro 5042 sensors exhibited what appeared to be signal overshoot from which it recovered faster with each subsequent cycle. Also, while being purged with N_2 during the second and third cycles, the Figaro 5042 demonstrated undershoot by indicating a negative CO concentration. This behavior was more exaggerated in the third cycle as compared to the second, but the signal output eventually returned to approximately 0 mg CO/m^3 in both cases. Overall, the GrayWolf responded slowly to the presence of CO; however, its response time increased as the number of cycles increased. The performance of the e2v was the most consistent sensor, but its final steady state output decreased with each cycle. In addition, the e2v did not exhibit a first order response to the rising CO concentration. Rather it demonstrated an inflection point from concave up to concave down somewhere along its CO concentration profile for all three cycles.

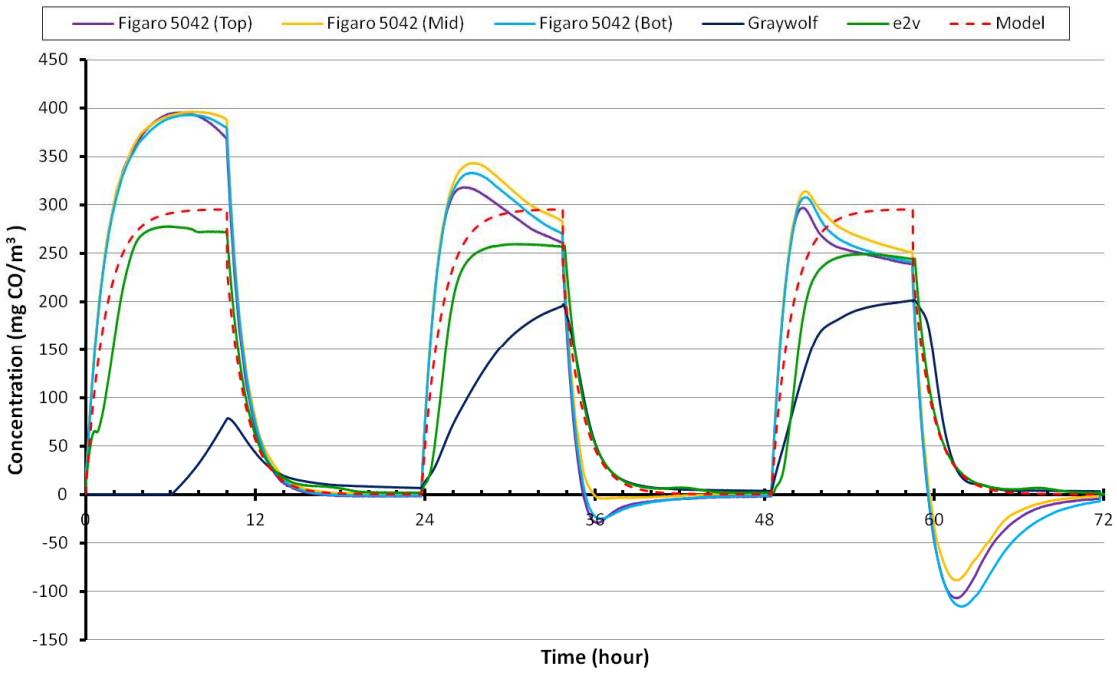

Figure 4.16: CO sensor results for repeatability experiment performed without O_2 in the gas mixture at 101.3 kPa with a steady state concentration of 295 mg CO/m^3.

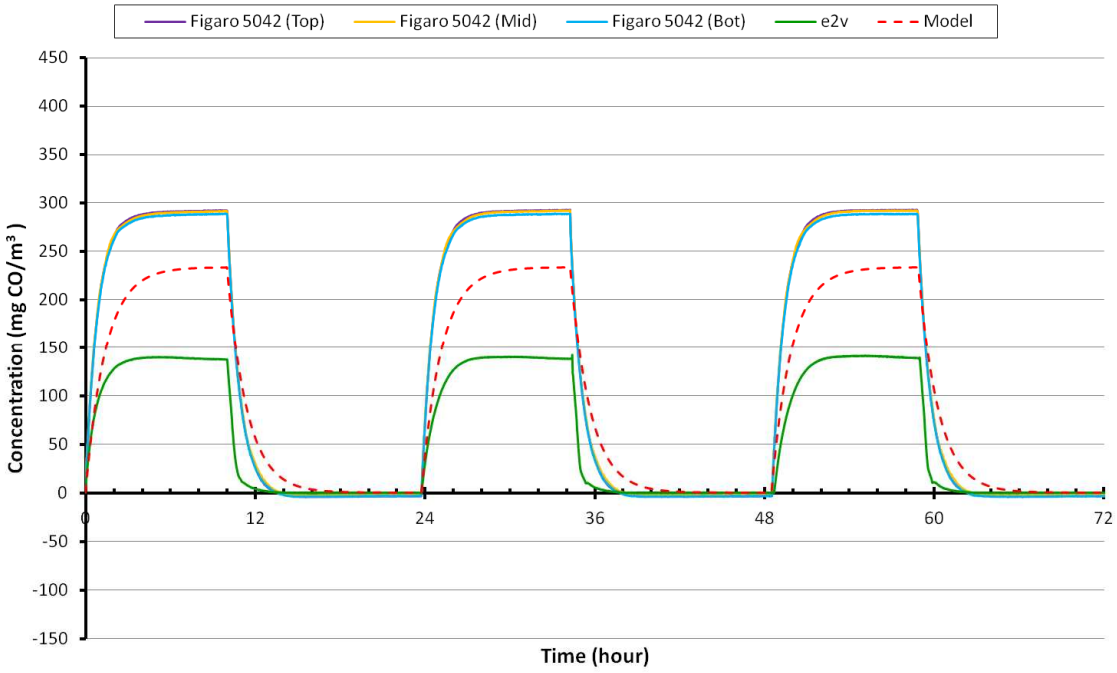

Figure 4.17: CO sensor results for repeatability experiment performed with 21% O_2 in the gas mixture at 101.3 kPa with a steady state concentration of 233 mg CO/m^3.

References in the literature indicate a need for ambient O_2 during the operation of electrochemical CO sensors [54, 55]. Additional experiments were performed with the addition of O_2 to the gas mixture. The first experiment with the addition of O_2 repeated the 293 mg CO/m^3 at 101.3 kPa experiment. Pure O_2 was added to the N_2 purge gas and the CO in N_2 test gas so that the final gas mixture was 21% O_2. The known gas concentration was diluted to 233 mg CO/m^3, as shown in Table 3.10, due to the mixing with O_2 for the repeated experiment which was also taken into account in the analytical model.

Figure 4.17 presents the results of the repeated experiment with the addition of 21% O_2 to the gas mixture with a known CO gas concentration of 233 mg CO/m^3 at a pressure of 101.3 kPa. These results show a stark contrast to the experimental results without O_2. With the addition of O_2, the Figaro 5042 sensors exhibited stable, repeatable steady state output without any overshoot or undershoot. The e2v sensor demonstrated a first order response to an increase in the CO concentration with stable, repeatable steady state output. The e2v steady state values were the same for all three cycles and, thus, did not decrease with each cycle as they did in the experiment without O_2. The e2v sensor's output was significantly lower than the predicted model which could be the result of its calibration being in an O_2 free environment. Unfortunately, the GrayWolf sensor malfunctioned and never responded to any of the CO inside the sensor evaluation system during this experiment.

Overall, there was a significant improvement in the sensors' response with the addition of 21% O_2 to the gas mixture. One possible explanation for the poor results of the Figaro 5042 sensors in the experiment without 21% O_2 is that the O_2 was used up in

the oxidation reaction at the counter electrode, shown in Equation 2.4b. Once the O_2 was used up the sensors could no longer maintain normal operation and the output current, and subsequently the measured CO concentration, began to decrease. This behavior became more exaggerated with each CO cycle since the amount of available O_2 decreased with each successive cycle. The same explanation can be given for the poor output of the e2v sensor.

In addition, during the N_2 purge of the second and third cycles the Figaro 5042 sensors demonstrated a negative measured CO concentration. This negative measured CO concentration indicated that the sensors' output current began to flow in the opposite direction from the current flow during normal operation. Since there was very little O_2 present at the sensors, the chemical reaction at the counter electrode in Equation 2.4b began to operate in the reverse direction in an attempt to reach equilibrium which generated O_2 and electrons. Then, these electrons flowed backward to the working electrode and, thus, a negative current was generated which resulted in the Figaro 5042 sensors indicating a negative CO concentration measurement.

The sensors were additionally tested in the 21% O_2 gas mixture at a pressure of 101.3 kPa and then later 75.3 kPa, to evaluate the combined effect of pressure and ambient O_2 on the sensors' performance. For these experiments a source concentration of 58 mg CO/m^3 was used and resulted in a known CO gas concentration of 45 mg CO/m^3 for the 101.3 kPa experiment and a known gas concentration of 33 mg CO/m^3 for the experiment performed at 75.3 kPa, as shown in Table 3.10. Prior to the 101.3 kPa experiment the e2v sensor was calibrated in the 21% O_2 gas mixture at a pressure of 101.3 kPa with a known gas concentration of 137 mg CO/m^3.

The results of the experiments performed with a source concentration of 58 mg CO/m^3 at pressures of 101.3 and 75.3 kPa are presented in Figure 4.18 and Figure 4.19, respectively. These results show that the Figaro 5042 sensors exhibited first order, stable, repeatable steady state output without any overshoot or undershoot for both pressures tested. The Figaro 5042 sensors' output was slightly negative after all of the CO had been removed from the sensor evaluation system by the N_2 purge. This, however, can be corrected by adjusting the sensors' output voltage to measure a zero CO concentration when the sensor is not exposed to any CO. Unfortunately, the GrayWolf sensor malfunctioned and never responded to any of the CO inside the sensor evaluation system during the experiments performed at 101.3 and 75.3 kPa.

The e2v sensor demonstrated a first order response to an increase in the CO concentration for the experiments performed at both pressures of 101.3 and 75.3 kPa. While the e2v sensor showed no overshoot, its steady state output drifted significantly, while the Figaro 5042 sensors did not drift at all. This indicates that the e2v sensor is more affected by the presence of O_2 than the Figaro 5042 sensors.

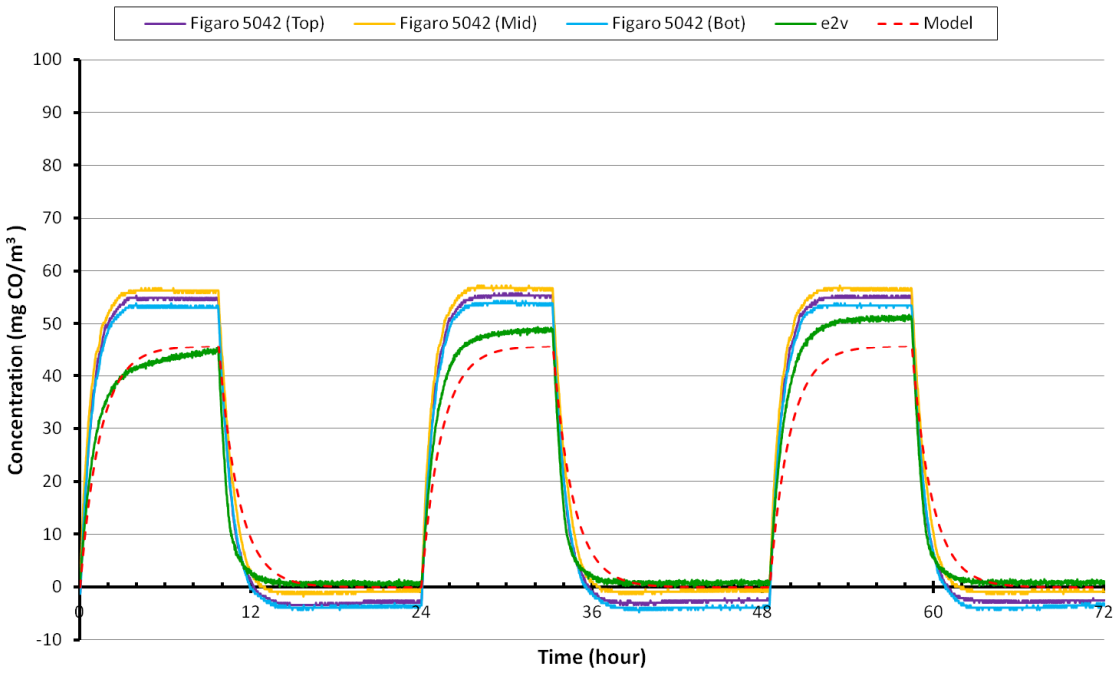

Figure 4.18: CO sensor results for repeatability experiment performed with 21% O_2 in the gas mixture at 101.3 kPa with a steady state concentration of 45 mg CO/m^3.

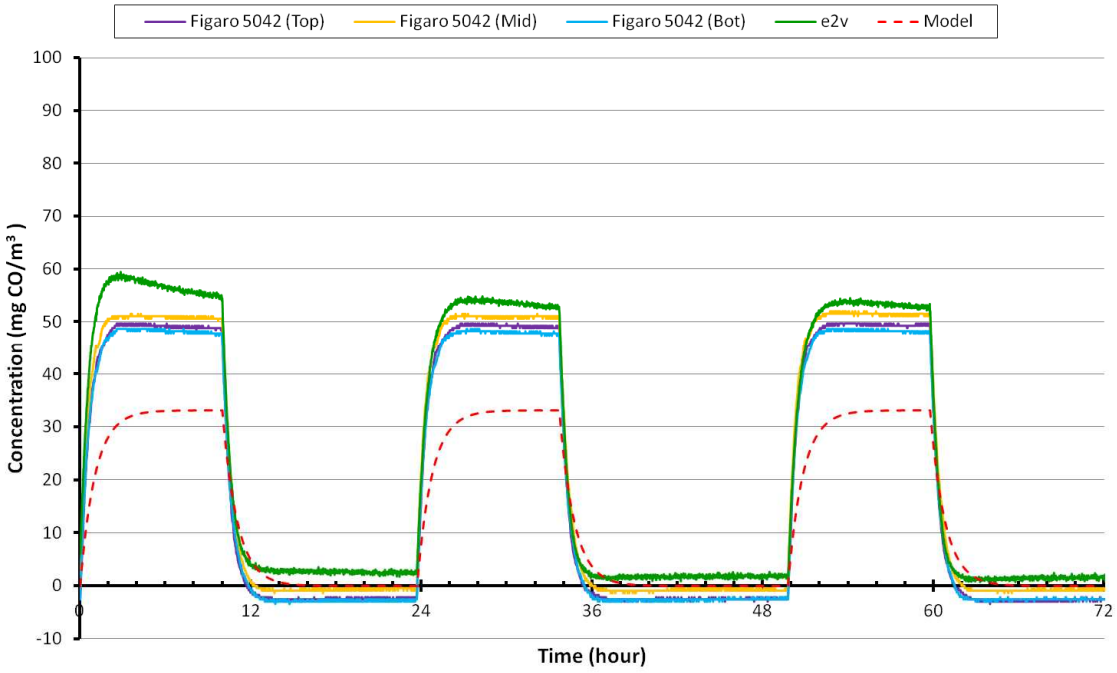

Figure 4.19: CO sensor results for repeatability experiment performed with 21% O_2 in the gas mixture at 75.3 kPa with a steady state concentration of 33 mg CO/m^3.

There are three main aspects in which the e2v and the Figaro 5042 sensors are different which likely contribute to their different responses in the O_2 and CO gas mixtures; the schematics of both the Figaro 5402 and the e2v sensors are in Figure 4.20 and Figure 4.21, respectively. The first difference between the two sensors is the way that O_2 diffuses into the sensor. For the e2v sensor the O_2 gas primarily diffuses through the capillary diffusion barrier, although some O_2 diffuses through the sensor housing [54]. The Figaro 5042 datasheet does not explicitly describe how O_2 enters the sensor package although the datasheet does say that O_2 does enter the sensor. The most likely path by which O_2 would enter the sensor is by diffusion through the gas inlet and the charcoal filter or between the gasket and the outer can of the sensor. These aspects of the physical design of the two sensors will have different effects on each sensor's ability to resupply the O_2 needed for the oxidation reaction at the counter electrode.

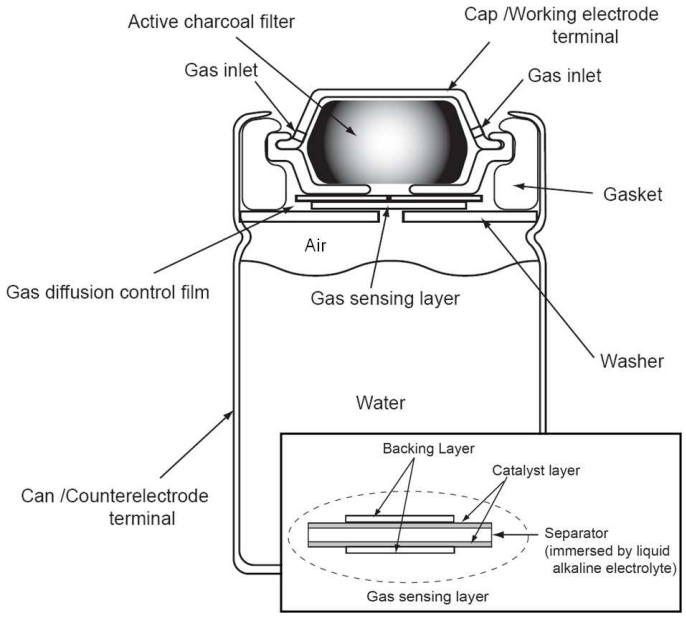

Figure 4.20: Schematic drawing of the Figaro TGS 5042-A00 [56].

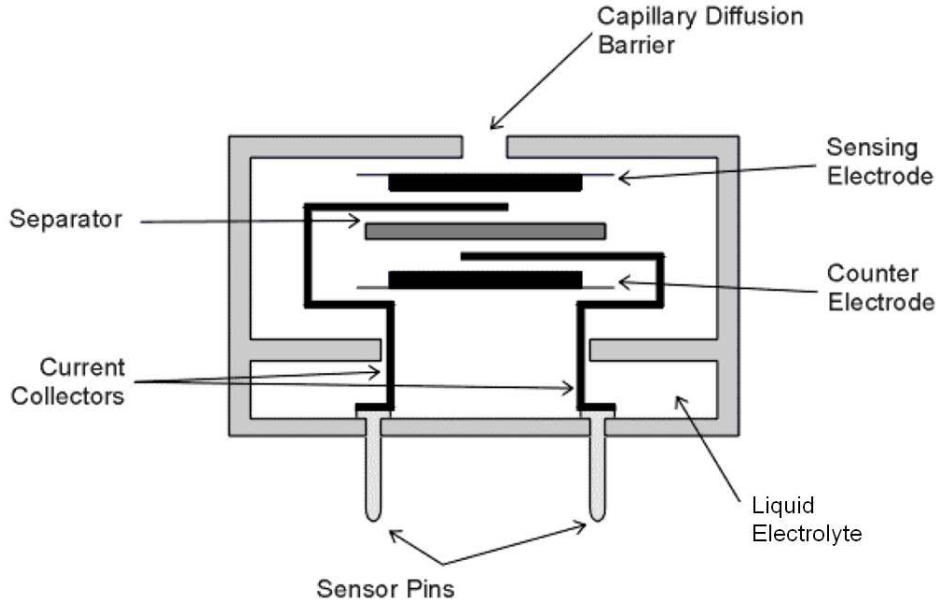

Figure 4.21: Schematic drawing of the e2v EC4-2000-CO [54].

The second difference between the e2v and the Figaro 5042 sensors involves where the O_2 is stored inside the sensor and how that affects the sensor's ability to replenish the O_2 at the counter electrode. The O_2 inside the e2v sensor is dissolved in a

liquid electrolyte while the O_2 inside the Figaro 5042 sensor is in the gas phase surrounded by H_2O. For the Figaro 5042 sensors, when the O_2 at the counter electrode is depleted the remaining O_2 in the gas phase is able to diffuse quickly to replace the O_2. In contrast, the O_2 in the e2v sensor is dissolved in the liquid electrolyte and diffuses much slower making it more difficult for the sensor to maintain an adequate amount of O_2 at the counter electrode. This phenomenon likely contributes to the drift of the e2v sensor's output and, therefore, makes it difficult for the sensor to properly measure the steady state CO concentration.

The third difference between the e2v and the Figaro 5042 sensors is how the working and counter electrodes are physically positioned inside each sensor. For the e2v sensor, both the working and the counter electrodes are immersed in the liquid electrolyte which contains dissolved O_2. In contrast, the O_2 inside the Figaro 5042 sensors is present only at the counter electrode. When the O_2 concentration inside each sensor changes, the sensor's output could be different due to the physical difference in the location of the electrodes in each sensor and their access to the O_2 inside. All of these three factors contribute to the ability of the sensor to properly measure the CO concentration and are likely contributors to the different measured outputs between the e2v and the Figaro 5042 sensors.

Chapter 5: Summary and Conclusions

The performance of commercially available CO sensors was evaluated and analyzed under environmental conditions similar to those inside a commercial airline cabin. The sensors were operated in a sealed chamber where the total pressure and the CO concentration could be controlled. The CO test gas was supplied by purchased, premixed tanks of CO in N_2. The steady state and the transient response of the sensors to various CO concentrations and pressures were analyzed. In addition, the repeatability of the sensors was evaluated in gas mixtures that contained O_2 and those that did not contain O_2.

This study discovered that the CO sensors usually overestimated the amount of the CO inside the system while exhibiting a linear response to an increase in the CO concentration. This means that the sensors must be calibrated so that their output reflects the actual amount of CO to which they are exposed. In addition, it was discovered that the linear response of the sensors changes based on the total pressure in which the sensor is operating. This means that the sensor must also be calibrated to correct for the effects of pressure on its ability to detect the correct amount of CO to which it is exposed.

Further, it was demonstrated that O_2 has a significant influence on the output of electrochemical CO sensors. Without O_2 in the gas mixture, the sensors' output was characterized by a second order response with overshoot and undershoot. However, with the addition of 21% O_2 to the gas mixture, the sensors' output exhibited a first order

response that was stable and repeatable with no overshoot or undershoot. This means that the CO sensors should not be operated in an O_2 free environment. It is acknowledged that this conclusion is potentially irrelevant if the sensors are operated in an environment that is conducive for human occupation; however, this conclusion should certainly be considered if the sensors are operated in an environment devoid of O_2 or where the O_2 concentration varies.

Chapter 6: Recommendations for Future Work

The entire set of CO sensor experiments in this study was performed with a gas mixture of CO in N_2, yet the repeatability experiments demonstrated a significant improvement in the sensors' performance with the addition of O_2 to the gas mixture. As a result, it is recommended that all future CO sensor experiments be performed with approximately 21% O_2 in the gas mixture. In addition, it is recommended that the CO sensor experiments be repeated with this new gas mixture, and the results should be compared to the CO sensor experiments performed without O_2. It would be interesting to investigate if the slope of the sensors' linear behavior still increases as the pressure decreases, as it does in the experiments without O_2 (Figure 4.7), and to investigate the effect of O_2 on the sensors' transient response.

It is also recommended that the electrochemical sensors' response to CO in the absence of O_2 be further evaluated. In addition, how O_2 enters and is stored by each sensor should also be studied further. This would allow for understanding of how much O_2 is needed for the sensors to operate normally, as well as the effect on the sensors' output due to variations in the amount of O_2. If the electrochemical sensors' response is dependent on variations in the amount of O_2 then this must be taken into account if the sensors are operated onboard aircraft.

In this study, a known CO gas concentration was cycled through the system three times which provided a general understanding of the repeatability behavior of the

sensors. To further evaluate the sensors' response to a change in the CO concentration, it is recommended that a series of tests be performed where the steady state CO concentration is systematically incremented and decremented at a constant pressure. This will provide a more extensive understanding of the dependence of the sensors' response based on the previous concentrations to which they were exposed. It is also recommended that this set of experiments be performed not only at sea level pressure but also at the lower pressures experienced onboard commercial aircraft.

This study focused on electrochemical CO sensors, yet there are many CO sensors that operate using the MOS technology. It is recommended for future work that MOS CO sensors be tested in the same manner as the electrochemical sensors in this study were tested. It is further recommended that both the electrochemical and the MOS sensors be physically dismantled in a systematic manner in an effort to better understand how they operate.

References

[1] Bureau of Transportation Statistics, “Bureau of Transportation Statistics T-100 Market Data,” *Airline Passenger Statistical Data*, Mar-2012. [Online]. Available: http://www.transtats.bts.gov/Data_Elements.aspx?Data=1. [Accessed: 12-Mar-2012].

[2] R. Babbitt, “FAA Aerospace Forecast: Fiscal Years 2010-2030,” Federal Aviation Administration, Forecast, 2010.

[3] WCNC - TV, Inc., “Plane with Sick Passengers Had Air Contamination Before,” 20-Jan-2010.

[4] Cable News Network, “De-icing solution sends air crew members to hospital,” 24-Dec-2008.

[5] J. Ravitz, “Toxic plane air sickens flight attendant, suit says,” *Cable News Network*, 03-Jul-2009.

[6] J. Gold, “Boeing suit settlement stirs jetliner air safety debate: Documents show firm long concerned about health risks of rare fume events,” *MicroSoft National Broadcasting Company*, 06-Oct-2011.

[7] A. J. Neer, J. R. Andress, R. L. Haney, R. A. Overfelt, B. C. Prorok, J. W. Fergus, and L. C. Mathison, “Preliminary Investigation into Thermal Degradation Behavior of Mobil Jet Oil II,” presented at the International Conference on Environmental Systems, Portland, Oregon, 2011.

[8] A. J. Neer, “Development of a Laboratory Apparatus to Study the Thermal Degradation Behavior of Commercial Jet Engine Oils,” Auburn University.

[9] Underwriters Laboratories INC., *UL2034: Single and Multiple Station Carbon Monoxide Alarms*, 2nd ed. 1996.

[10] 14 C.F.R. 25, 2011.

[11] M. Sinnett, “787 No-Bleed Systems: Saving Fuel and Enhancing Operational Efficiencies,” *AERO Magazine*, vol. 28, no. 4, pp. 6–11, 2007.

[12] E. H. Hunt, D. H. Reid, D. R. Space, and F. E. Tilton, “Commercial airliner environmental control system–engineering aspects of cabin air quality,” in *Aerospace Medical Association annual meeting*, 1995.

[13] E. H. Hunt and D. R. Space, “The airplane cabin environment: Issues pertaining to flight attendant comfort,” The Boeing Company, 1994.

[14] N. L. Nagda and M. D. Koontz, “Measurement of Cabin Air Quality Aboard Commerical Airliners,” *Atmospheric Environment*, vol. 26A, no. 12, pp. 2203–2210, 1992.

[15] C. W. Spicer, M. J. Murphy, M. W. Holdren, J. D. Myers, I. C. MacGregor, C. Holloman, R. R. James, K. Tucker, and R. Zaborski, “Relate air quality and other factors to comfort and health symptoms reported by passengers and crew on commercial transport aircraft (Part I), ASHRAE Project 1262-TRP, American

Society for Heating, Refrigerating and Air Conditioning Engineers," 1262-TRP, 2004.
[16] C. Thibeault, "Cabin air quality," *Aviation Space and Environmental Medicine*, vol. 68, pp. 80–82, 1997.
[17] "AUS20040323.pdf," Federal Aviation Administration, Service Difficulty Report AUS20040323, Jul. 2004.
[18] "COMA0460639.pdf," Federal Aviation Administration, Service Difficulty Report COMA0460639, Nov. 2004.
[19] "DL76S050068.pdf," Federal Aviation Administration, Service Difficulty Report DL76S050068, Feb. 2005.
[20] "UALA2010102603959.pdf," Federal Aviation Administration, Service Difficulty Report UALA2010102603959, Oct. 2010.
[21] "C2XA10RI136.pdf," Federal Aviation Administration, Service Difficulty Report C2XA10RI136, Nov. 2010.
[22] "DALA1158840964.pdf," Federal Aviation Administration, Service Difficulty Report DALA1158840964, Oct. 2011.
[23] C. van Netten, "Air Quality and Health Effects Associated with the Operation of BAe 146-200 Aircraft," *Applied Occupational and Environmental Hygiene*, vol. 13, no. 10, pp. 733–739, Oct. 1998.
[24] C. van Netten, "Aircraft Air Quality Incidents, Symptoms, Exposures and Possible Solutions," in *Reports in Safety and Environmental Science*, Imperial College, London, 2005, pp. 243–253.
[25] R. Harrison, J. Murawski, E. McNeely, J. Guerriero, and D. Milton, "Exposure to Aircraft Bleed Air Contaminants among Airline Workders: A Guide for Health Care Providers," Federal Aviation Administration, Reference, Apr. 2009.
[26] S. Nassauer, "Up in the Air: New Worries About 'Fume Event' on Planes," *The Wall Street Journal*, 30-Jul-2009.
[27] E. Whelan, C. Lawson, B. Grajewski, M. Petersen, L. Pinkerton, E. Ward, and T. Schnorr, "Prevalence of respiratory symptoms among female flight attendants and teachers," *Occupational and environmental medicine*, vol. 60, no. 12, pp. 929–934, 2003.
[28] S. T. Omaye, "Metabolic modulation of carbon monoxide toxicity," *Toxicology*, vol. 180, no. 2, pp. 139–150, 2002.
[29] J. A. Raub, M. Mathieu-Nolf, N. B. Hampson, and S. R. Thom, "Carbon monoxide poisoning–a public health perspective," *Toxicology*, vol. 145, no. 1, pp. 1–14, 2000.
[30] C. R. Mackerer, M. L. Barth, A. J. Krueger, B. Chawla, and T. A. Roy, "Comparison of neurotoxic effects and potential risks from oral administration or ingestion of tricresyl phosphate and jet engine oil containing tricresyl phosphate," *Journal of Toxicology and Environmental Health, Part A: Current Issues*, vol. 57, no. 5, pp. 293–328, 1999.
[31] C. Winder and S. Michaelis, "Crew effects from toxic exposures on aircraft," *Air Quality in Airplane Cabins and Similar Enclosed Spaces*, pp. 229–248, 2005.
[32] C. van Netten, "Analysis of two jet engine lubricating oils and a hydraulic fluid: Their pyrolytic breakdown products and their implication on aircraft air quality," in *Air Quality and Comfort in Airliner Cabins*, 2000, pp. 61–75.

[33] C. van Netter and V. Leung, “Comparison of the constituents of two jet engine lubricating oils and their volatile pyrolytic degradation products,” *Journal of Occupational and Environmental Hygiene*, vol. 15, no. 3, pp. 277–283, 2000.
[34] A. F. Sedda and G. Rossi, “Death scene evaluation in a case of fatal accidental carbon monoxide toxicity,” *Forensic science international*, vol. 164, no. 2–3, pp. 164–167, 2006.
[35] J. A. Raub and V. A. Benignus, “Carbon monoxide and the nervous system,” *Neuroscience & Biobehavioral Reviews*, vol. 26, no. 8, pp. 925–940, 2002.
[36] K. L. Meert, S. M. Heidemann, and A. P. Sarnaik, “Outcome of children with carbon monoxide poisoning treated with normobaric oxygen,” *The Journal of trauma*, vol. 44, no. 1, p. 149, 1998.
[37] L. Levasseur, M. Galliot-Guilley, F. Richter, J. M. Scherrmann, and Baud, “Effects of mode of inhalation of carbon monoxide and of normobaric oxygen administration on carbon monoxide elimination from the blood,” *Human & Experimental Toxicology*, vol. 15, no. 11, pp. 898–903, Nov. 1996.
[38] L. K. Weaver, R. O. Hopkins, K. J. Chan, S. Churchill, C. G. Elliott, T. P. Clemmer, J. F. Orme Jr, F. O. Thomas, and A. H. Morris, “Hyperbaric oxygen for acute carbon monoxide poisoning,” *New England Journal of Medicine*, vol. 347, no. 14, pp. 1057–1067, 2002.
[39] D. Elkarrat, J. C. Raphael, J. M. Korach, M. C. Jars-Guincestre, C. Chastang, C. Harboun, and P. Gajdos, “Acute carbon monoxide intoxication and hyperbaric oxygen in pregnancy,” *Intensive Care Med*, vol. 17, no. 5, pp. 289–292, 1991.
[40] N. A. Buckley, G. K. Isbister, B. Stokes, and D. N. Juurlink, “Hyperbaric oxygen for carbon monoxide poisoning: a systematic review and critical analysis of the evidence,” *Toxicol Rev*, vol. 24, no. 2, pp. 75–92, 2005.
[41] C. D. Scheinkestel, M. Bailey, P. S. Myles, K. Jones, D. J. Cooper, I. L. Millar, and D. V. Tuxen, “Hyperbaric or normobaric oxygen for acute carbon monoxide poisoning: a randomised controlled clinical trial,” *Med J Aust*, vol. 170, no. 5, pp. 203–210, 1999.
[42] K. Nakamoto, *Infrared and Raman Spectra of Inorganic and Coordination Compounds, Theory and Applications in Inorganic Chemistry*, Part A. Wiley-Interscience, 2009.
[43] B. C. Smith, *Fundamentals of Fourier Transform Infrared Spectroscopy*, 1st ed. CRC Press, 1995.
[44] R. L. Haney, “Principal Component Analysis for Enhancement of Infrared Spectra Monitoring,” Auburn University, 2012.
[45] P. Griffiths and J. A. D. Haseth, *Fourier Transform Infrared Spectrometry*, 2nd ed. Wiley-Interscience, 2007.
[46] B. H. Stuart, B. George, and P. McIntyre, *Modern Infrared Spectroscopy*, 2nd ed. John Wiley & Sons, 1996.
[47] H. Dubost and L. Abouaf-Marguin, “Infrared Spectra of Carbon Monoxide Trapped in Solid Argon. Double-Doping Experiments with H2O, N3, AND N2,” *Chemical Physics Letters*, vol. 17, no. 2, pp. 269–273, Nov. 1972.
[48] A. H. Nielsen and R. J. Lagemann, “The Infrared Spectrum and Molecular Constants of C14O2,” *The Journal of Chemical Physics*, vol. 22, no. 1, p. 36, 1954.

[49] W. S. Benedict, N. Gailar, and E. K. Plyler, “Rotation-Vibration Spectra of Deuterated Water Vapor,” *The Journal of Chemical Physics*, vol. 24, no. 6, p. 1139, 1956.
[50] P. M. Eller and M. E. Cassinelli, *Niosh Manual of Analytical Methods*. DIANE Publishing, 1994.
[51] L. A. Gundel, T. W. Kirchstetter, M. Spears, and D. P. Sullivan, “Aircraft Cabin Environmental Quality Sensors,” Lawrence Berkeley National Laboratory, Berkeley, CA, Final Report, 2010.
[52] L. Boettern, “Chapter 7: How Sensors Work,” Brandt Instruments, Inc., Jan. 2000.
[53] C. C. Liu, *Electrochemical sensors*. The Biomedical Engineering Handbook. Boca Raton, FL: CRC Press, 1995.
[54] e2v Technologies, “Introduction to Electrochemical Gas Sensors.” application note, Feb-2007.
[55] Alphasense, Ltd., “How Electrochemical Gas Sensors Work.” application note AAN 104.
[56] Figaro USA, Inc., “Technical Information for TGS5042.” TGS-5042 datasheet, Oct-2011.
[57] J. Chou, *Hazardous Gas Monitors*. The McGraw-Hill Companies, Inc. and SciTech Publishing, Inc., 1999.
[58] e2v Technologies, “MiCS Application Note 3: Using MiCS-5525 for CO Detection.” MiCS-5525 application note, 2009.
[59] Figaro USA, Inc., “TGS 3870 Product Information.” TGS-3870 datasheet, 2004.
[60] Automation Components, Inc., “ACI Product Data A/CO Series.” A/CO-R-D datasheet, 2007.
[61] CO Guardian LLC, “User’s Manual For Model Aero-551.” Aero-551 user’s manual, 2006.
[62] e2v Technologies, “EC4-2000-CO Carbon Monoxide Electrochemical Sensor.” EC4-2000-CO datasheet, 2009.
[63] e2v Technologies, “ECVQ-EK3: Electrochemical and Pellistor Gas Sensor Evaluation Kit.” EVCQ-EK3 datasheet, Aug-2010.
[64] Figaro USA, Inc., “Application Notes for TGS5042.” TGS-5042 application note, 2010.
[65] Figaro USA, Inc., “COM 5042: Evaluation Module for TGS 5042.” COM5042 datasheet.
[66] First Alert, Inc., “First Alert CO615 User Manual.” CO615 user’s manual, 2006.
[67] Graywolf Sensing Solutions, “DirectSense IAQ: Indoor Air Quality Monitors.” IQ-604 datasheet, 2009.
[68] Kidde Residential and Commercial, “Carbon Monoxide Alarm: Battery Operated with Digital Display.” 900-0146 datasheet.
[69] SenseAir, “aSENSE m III CO/CO2 sensor & ventilation controller.” aSENSE m III datasheet.
[70] ASHRAE, *Ashrae Handbook: Fundamentals; SI Edition*. Ashrae, 2005.
[71] H. Günzler and H.-U. Gremlich, *IR Spectroscopy: An Introduction*. Wiley VCH, 2002.

[72] Bureau of Transportation Statistics, “Bureau of Transportation Statistics T-100 Market Data,” *Airline Passenger Statistical Data*, Apr-2012. [Online]. Available: http://www.bts.gov/xml/air_traffic/src/index.xml#MonthlySystem. [Accessed: 10-Apr-2012].

Appendix A: Individual Sensors' Response

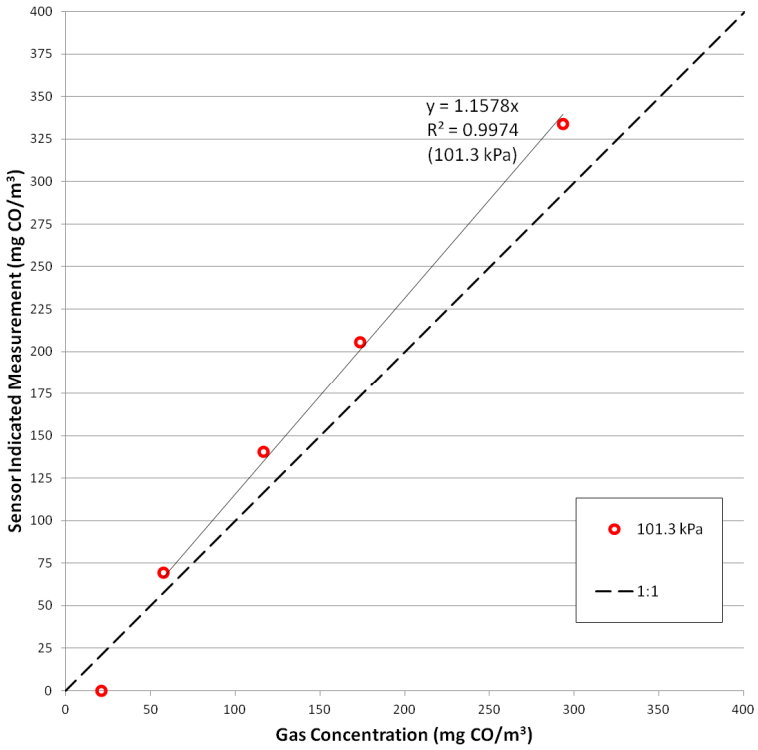

Figure A.1: Kidde response at a pressure of 101.3 kPa.

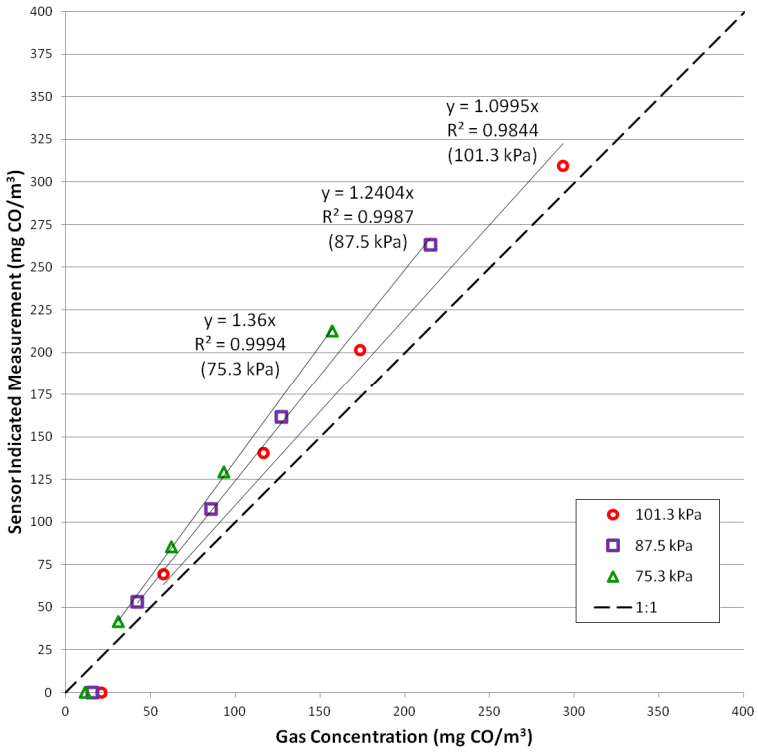

Figure A.2: FirstAlert response at pressures of 101.3, 87.5 and 75.3 kPa

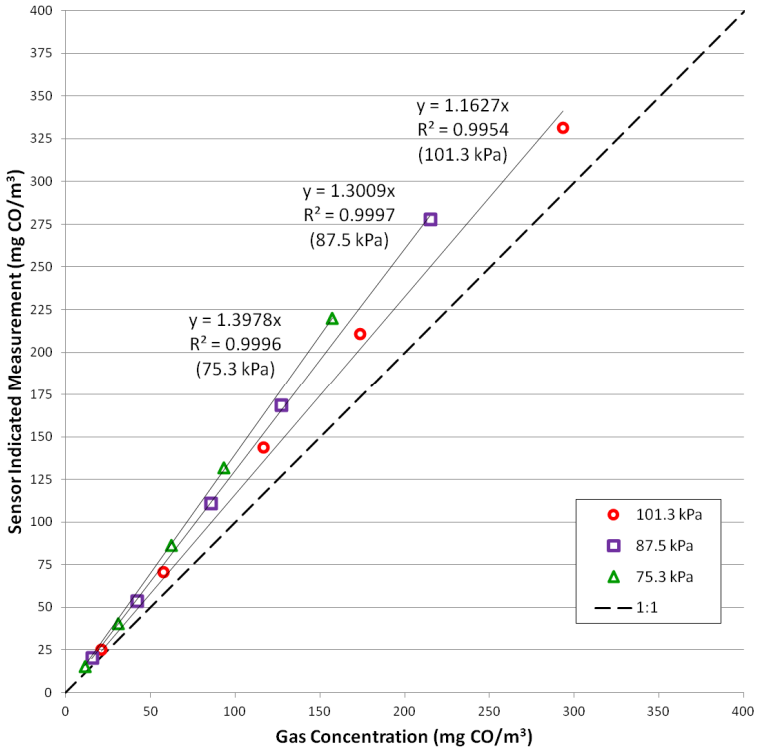

Figure A.3: CO Guardian response at pressures of 101.3, 87.5 and 75.3 kPa

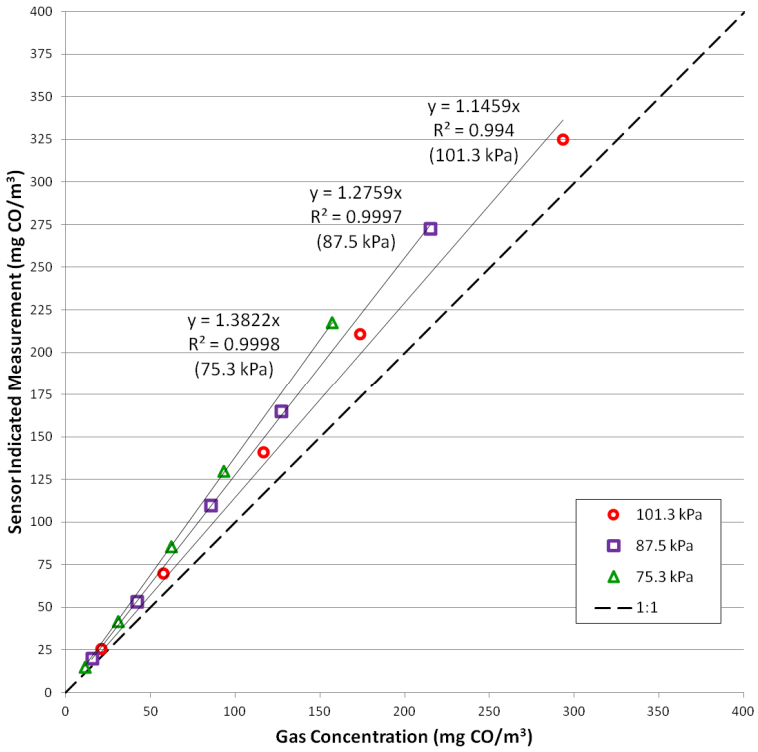

Figure A.4: SenseAir response at pressures of 101.3, 87.5 and 75.3 kPa

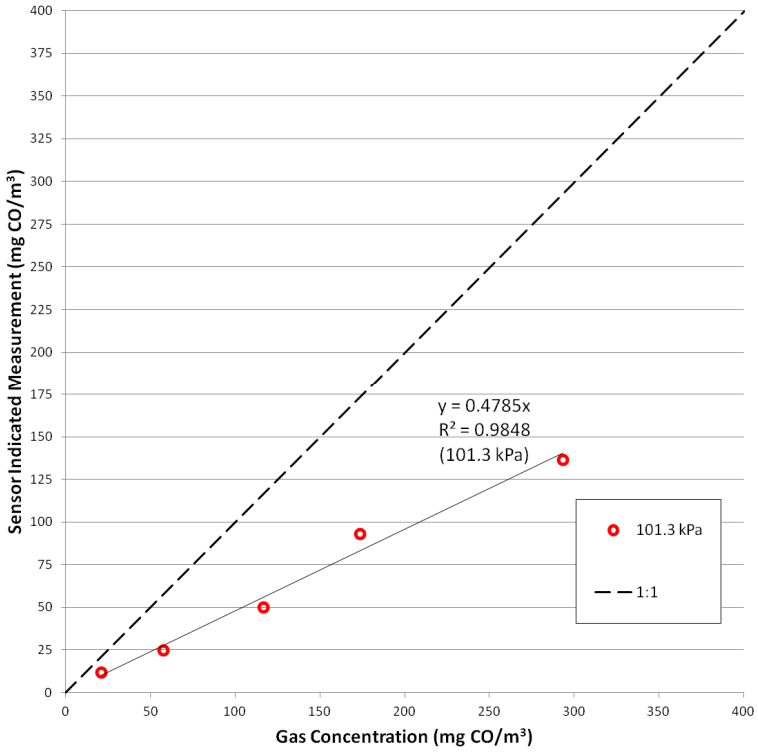

Figure A.5: GrayWolf response at a pressure of 101.3 kPa

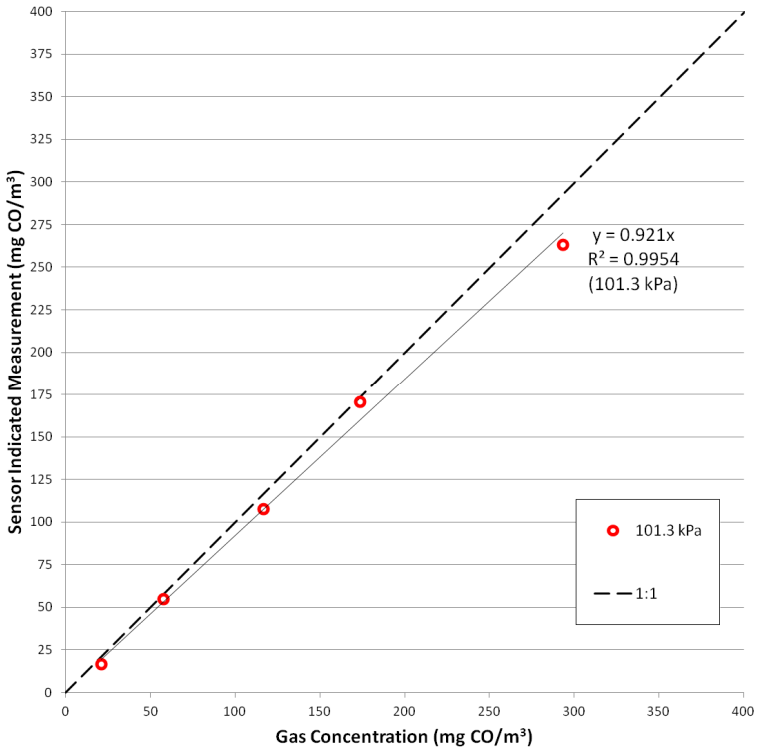

Figure A.6: e2v EC4-2000-CO response at pressures of 101.3, 87.5 and 75.3 kPa

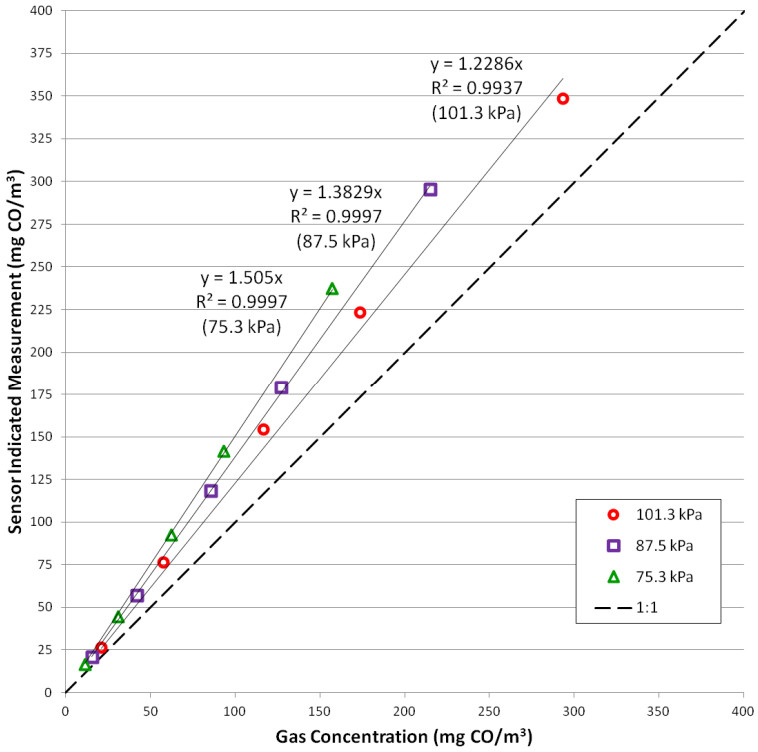

Figure A.7: Figaro 5042 (Top) response at pressures of 101.3, 87.5 and 75.3 kPa

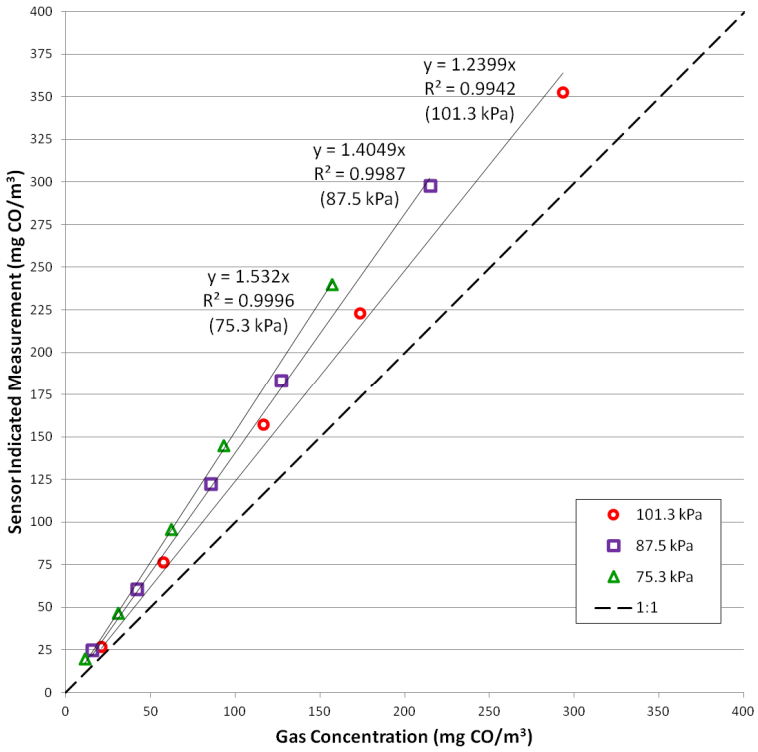

Figure A.8: Figaro 5042 (Mid) response at pressures of 101.3, 87.5 and 75.3 kPa

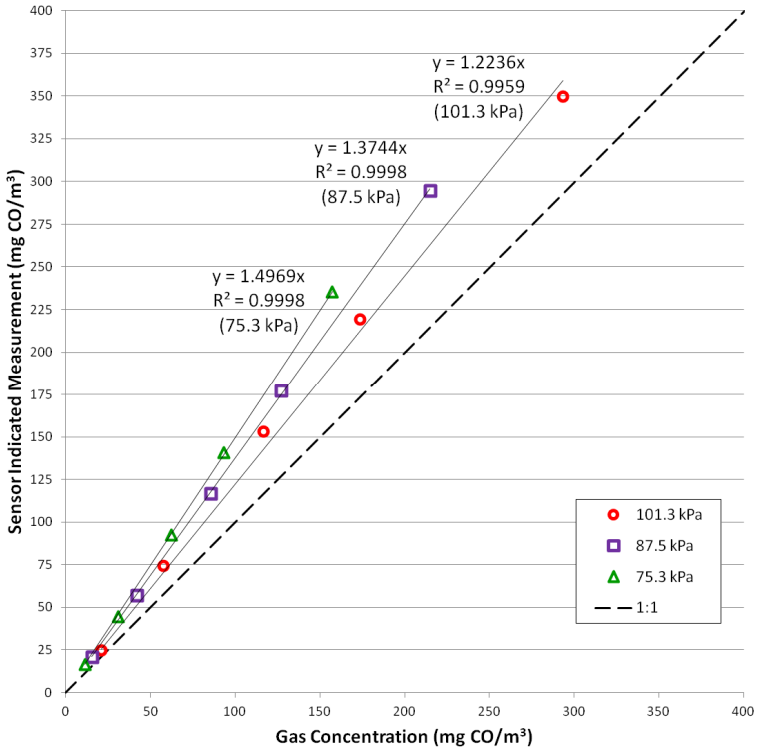

Figure A.9: Figaro 5042 (Bot) response at pressures of 101.3, 87.5 and 75.3 kPa

Appendix B: Steady State CO Sensor Output

Table B.1
CO Sensor Output at 101.3 kPa[†‡]

	Carbon Monoxide Steady-State Concentration (mg CO/m^3)				
Sensors	21	58	116	174	293
ACI, A/CO-R-D	–	–	–	–	–
CO Guardian, Aero-551	25 ± 1%	71 ± 1%	144 ± 1%	211 ± 1%	331 ± 1%
e2v Tech, EC4-2000-CO	16.9 ± 0.3%	55.1 ± 0.1%	107.9 ± 0.1%	170.7 ± 0.1%	263.3 ± 0.1%
Figaro, TGS 5042 (Top)	26.7 ± 0.2%	76.5 ± 0.1%	154.5 ± 0.1%	223.4 ± 0.1%	348.7 ± 0.1%
Figaro, TGS 5042 (Mid)	26.9 ± 0.2%	76.7 ± 0.1%	157.3 ± 0.1%	223.3 ± 0.1%	352.8 ± 0.1%
Figaro, TGS 5042 (Bot)	24.9 ± 0.2%	74.6 ± 0.1%	153.1 ± 0.1%	219.4 ± 0.1%	349.8 ± 0.1%
First Alert, CO410	–	70 ± 1%	141 ± 1%	202 ± 1%	310 ± 1%
GrayWolf, IQ-610	12.1 ± 0.2%	24.9 ± 0.1%	50.3 ± 0.2%	93.4 ± 0.1%	136.9 ± 0.4%
Kidde, KN-COPP-B	–	70 ± 1%	141 ± 1%	206 ± 1%	334 ± 1%
Sense Air, aSENSE™ mIII	26 ± 1%	70 ± 1%	141 ± 1%	211 ± 1%	325 ± 1%

[†] Values reported as the mean ± the standard error (1σ) as a percentage of the mean
[‡] All mean values are given in mg CO/m^3

Table B.2
CO Sensor Output at 87.5 kPa[†‡]

	Carbon Monoxide Steady-State Concentration (mg CO/m^3)[§]				
Sensors	15	42	85	127	215
ACI, A/CO-R-D	–	–	–	–	–
CO Guardian, Aero-551	21 ± 2%	54 ± 1%	111 ± 1%	169 ± 1%	278 ± 1%
e2v Tech, EC4-2000-CO	7.0 ± 0.5%	22.7 ± 0.6%	75.8 ± 0.7%	129.6 ± 0.4%	217.7 ± 0.1%
Figaro, TGS 5042 (Top)	20.8 ± 0.3%	57.0 ± 0.1%	118.5 ± 0.1%	179.1 ± 0.1%	295.6 ± 0.1%
Figaro, TGS 5042 (Mid)	25.1 ± 0.1%	60.6 ± 0.1%	122.4 ± 0.1%	183.3 ± 0.1%	297.9 ± 0.1%
Figaro, TGS 5042 (Bot)	20.9 ± 0.2%	56.9 ± 0.1%	116.6 ± 0.2%	177.3 ± 0.1%	294.6 ± 0.1%
First Alert, CO410	–	53 ± 1%	108 ± 1%	162 ± 1%	263 ± 1%
GrayWolf, IQ-610	–	–	–	–	–
Kidde, KN-COPP-B	–	44 ± 1%	106 ± 1%	150 ± 1%	192 ± 1%
Sense Air, aSENSE™ mIII	20 ± 1%	53 ± 1%	110 ± 1%	165 ± 1%	273 ± 1%

[†] Values reported as the mean ± the standard error (1σ) as a percentage of the mean
[‡] All mean values are given in mg CO/m^3
[§] Assumes a leak rate of 9 sccm

Table B.3
CO Sensor Output at 75.3 kPa[†‡]

	Carbon Monoxide Steady-State Concentration (mg CO/m^3)[§]				
Sensors	11	31	62	93	157
ACI, A/CO-R-D	–	–	–	–	–
CO Guardian, Aero-551	15 ± 3%	41 ± 1%	86 ± 1%	132 ± 1%	220 ± 1%
e2v Tech, EC4-2000-CO	5.9 ± 0.5%	12.7 ± 0.8%	52.8 ± 0.7%	98.7 ± 0.5%	177 ± 0.1%
Figaro, TGS 5042 (Top)	16.4 ± 0.2%	44.4 ± 0.1%	92.5 ± 0.1%	141.2 ± 0.1%	237.2 ± 0.1%
Figaro, TGS 5042 (Mid)	19.7 ± 0.2%	46.4 ± 0.1%	95.6 ± 0.1%	144.7 ± 0.1%	240.0 ± 0.1%
Figaro, TGS 5042 (Bot)	16.2 ± 0.2%	44.5 ± 0.1%	92.5 ± 0.1%	140.8 ± 0.1%	235.5 ± 0.1%
First Alert, CO410	–	42 ± 1%	85 ± 1%	129 ± 1%	212 ± 1%
GrayWolf, IQ-610	–	–	–	–	–
Kidde, KN-COPP-B	–	43 ± 1%	83 ± 1%	119 ± 1%	181 ± 1%
Sense Air, aSENSE™ mIII	15 ± 1%	42 ± 1%	85 ± 1%	130 ± 1%	218 ± 1%

[†] Values reported as the mean ± the standard error (1σ) as a percentage of the mean
[‡] All mean values are given in mg CO/m^3
[§] Assumes a leak rate of 15 sccm

Appendix C: CO Sensors' Time Constants

NO DATA PRESENTED ON THIS PAGE

Table C.1
Time Constants: 101.3 kPa[†‡]

	21.0 mg/m^3	R^2	57.5 mg/m^3	R^2	117 mg/m^3	R^2	174 mg/m^3	R^2	293 mg/m^3	R^2
Model (Sensor)	84.8 ± 0.0	1.00	84.8 ± 0.0	1.00	84.8 ± 0.0	1.00	84.8 ± 0.0	1.00	84.8 ± 0.0	1.00
Kidde	–	–	93.8 ± 7.4	0.92	84.7 ± 2.8	0.98	80.9 ± 1.6	0.99	74.1 ± 1.8	0.99
FirstAlert	–	–	80.5 ± 0.9	0.99	81.7 ± 1.4	0.99	81.8 ± 0.8	1.00	72.2 ± 2.5	0.98
CO Guard	86.5 ± 3.3	0.90	74.6 ± 1.5	0.99	76.0 ± 2.2	0.98	78.4 ± 1.3	0.99	67.3 ± 3.0	0.96
SenseAir	91 ± 1.9	0.99	77.6 ± 0.7	1.00	80.9 ± 1.1	1.00	83.8 ± 0.8	1.00	72.2 ± 2.7	0.98
GrayWolf	44.7 ± 0.2	0.90	–	–	167.5 ± 4.7	0.89	149.6 ± 0.1	1.00	–	–
Fig 5042 (Top)	76.3 ± 0.1	0.99	76.3 ± 0.0	1.00	76.8 ± 0.3	0.99	75.2 ± 0.1	0.98	60.7 ± 0.9	0.88
Fig 5042 (Mid)	84.7 ± 0.1	0.99	72.9 ± 0.1	1.00	77.2 ± 0.2	0.99	76.2 ± 0.1	0.99	63.0 ± 0.7	0.92
Fig 5042 (Bot)	68.5 ± 0.1	0.98	74.8 ± 0.1	1.00	78.6 ± 0.3	0.99	77.2 ± 0.1	0.99	63.1 ± 0.7	0.91

[†] Time constants are presented in units of minutes as $\tau \pm$ the standard error (1σ)
[‡] Columns are labeled with the steady state CO concentration in units of mg CO/m^3

Table C.2
Time Constants: 87.5 kPa[†‡]

	15.4 mg/m^3	R^2	42.2 mg/m^3	R^2	85.4 mg/m^3	R^2	127 mg/m^3	R^2	215 mg/m^3	R^2
Model (Sensor)	73.3 ± 0.0	1.00	73.3 ± 0.0	1.00	73.3 ± 0.0	1.00	73.3 ± 0.0	1.00	73.3 ± 0.0	1.00
FirstAlert	–	–	66.8 ± 0.8	0.99	67.6 ± 0.5	1.00	68.1 ± 0.6	1.00	65.8 ± 0.5	1.00
CO Guard	68.1 ± 9.0	0.66	63.7 ± 2.3	0.98	63.2 ± 1.2	1.00	64.8 ± 1.2	1.00	62.5 ± 0.6	1.00
SenseAir	76.0 ± 2.3.	0.99	66.7 ± 0.9	1.00	70.2 ± 0.6	1.00	68.9 ± 0.8	1.00	66.8 ± 0.5	1.00
Fig 5042 (Top)	71.5 ± 0.4	0.99	65.0 ± 0.2	1.00	67.0 ± 0.1	1.00	66.1 ± 0.2	1.00	63.1 ± 0.1	1.00
Fig 5042 (Mid)	66.1 ± 0.1	1.00	63.5 ± 0.2	1.00	66.5 ± 0.1	1.00	66.3 ± 0.1	1.00	62.3 ± 0.1	1.00
Fig 5042 (Bot)	75.8 ± 0.4	0.99	64.9 ± 0.2	1.00	66.4 ± 0.2	1.00	65.9 ± 0.1	1.00	63.8 ± 0.1	1.00

[†] Time constants are presented in units of minutes as $\tau \pm$ the standard error (1σ)
[‡] Columns are labeled with the steady state CO concentration in units of mg CO/m^3

Table C.3
Time Constants: 75.3 kPa[†‡]

	11.2 mg/m^3	R^2	30.9 mg/m^3	R^2	62.5 mg/m^3	R^2	93.1 mg/m^3	R^2	158 mg/m^3	R^2
Model (Sensor)	63.0 ± 0.0	1.00	63.0 ± 0.0	1.00	63.0 ± 0.0	1.00	63.0 ± 0.0	1.00	63.0 ± 0.0	1.00
FirstAlert	–	–	55.7 ± 1.5	0.96	63.4 ± 4.9	0.96	57.1 ± 0.5	1.00	56.1 ± 0.7	1.00
CO Guard	41.7 ± 8.2	0.28	53.5 ± 2.8	0.95	56.1 ± 1.2	1.00	54.2 ± 0.9	1.00	52.9 ± 0.6	1.00
SenseAir	59.4 ± 2.7	0.98	56.8 ± 1.1	1.00	56.6 ± 0.8	1.00	57.4 ± 0.7	1.00	56.9 ± 0.5	1.00
Fig 5042 (Top)	60.5 ± 0.4	0.99	54.5 ± 0.2	1.00	53.1 ± 0.1	1.00	54.8 ± 0.2	1.00	53.9 ± 0.1	1.00
Fig 5042 (Mid)	54.7 ± 0.2	1.00	50.6 ± 0.1	1.00	53.1 ± 0.1	1.00	55.0 ± 0.1	1.00	54.1 ± 0.1	1.00
Fig 5042 (Bot)	63.2 ± 0.4	0.99	55.3 ± 0.2	1.00	54.0 ± 0.1	1.00	55.5 ± 0.2	1.00	54.0 ± 0.1	1.00

[†] Time constants are presented in units of minutes as $\tau \pm$ the standard error (1σ)
[‡] Columns are labeled with the steady state CO concentration in units of mg CO/m^3

Appendix D: CO Sensors' Response Normalized to the Analytical Model

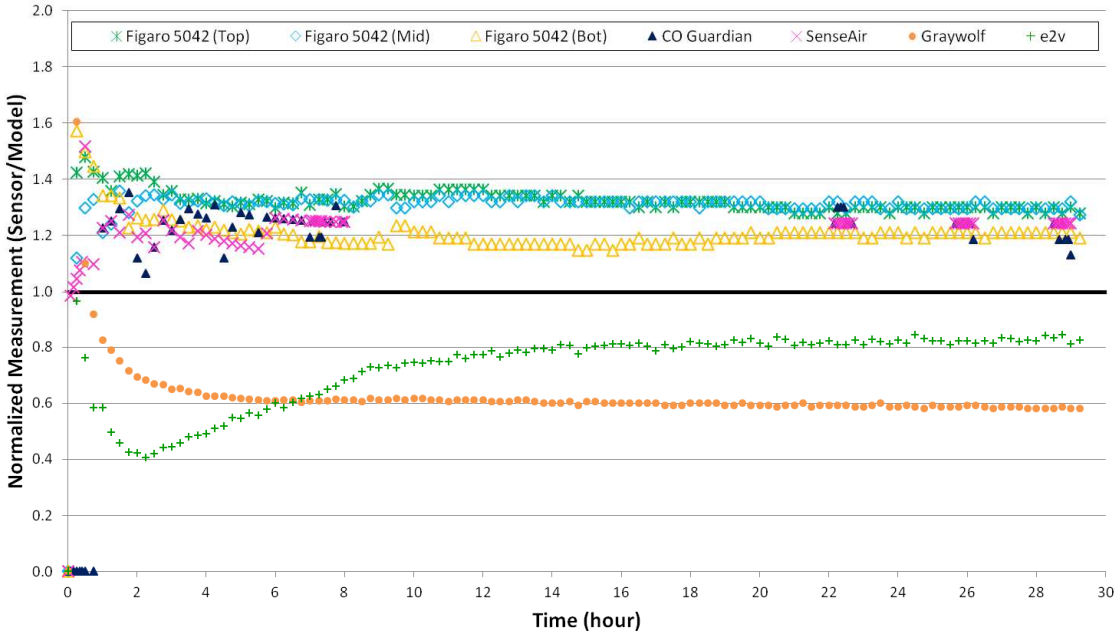

Figure D.1: Sensor measurement normalized to the analytical model versus time for a steady state concentration of 21 mg CO/m^3 at a pressure of 101.3 kPa. The flow rate was reduced from 500 to 50 sccm at t = 7 hr to conserve the test gas.

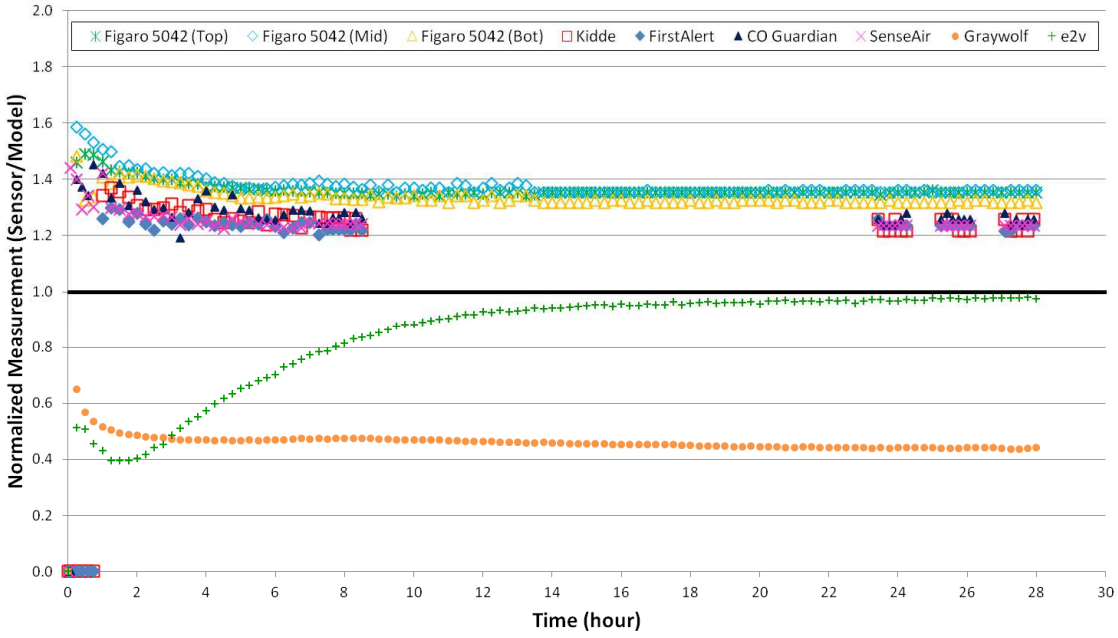

Figure D.2: Sensor measurement normalized to the analytical model versus time for a steady state concentration of 58 mg CO/m^3 at a pressure of 101.3 kPa. The flow rate was reduced from 500 to 50 sccm at t = 7.5 hr to conserve the test gas.

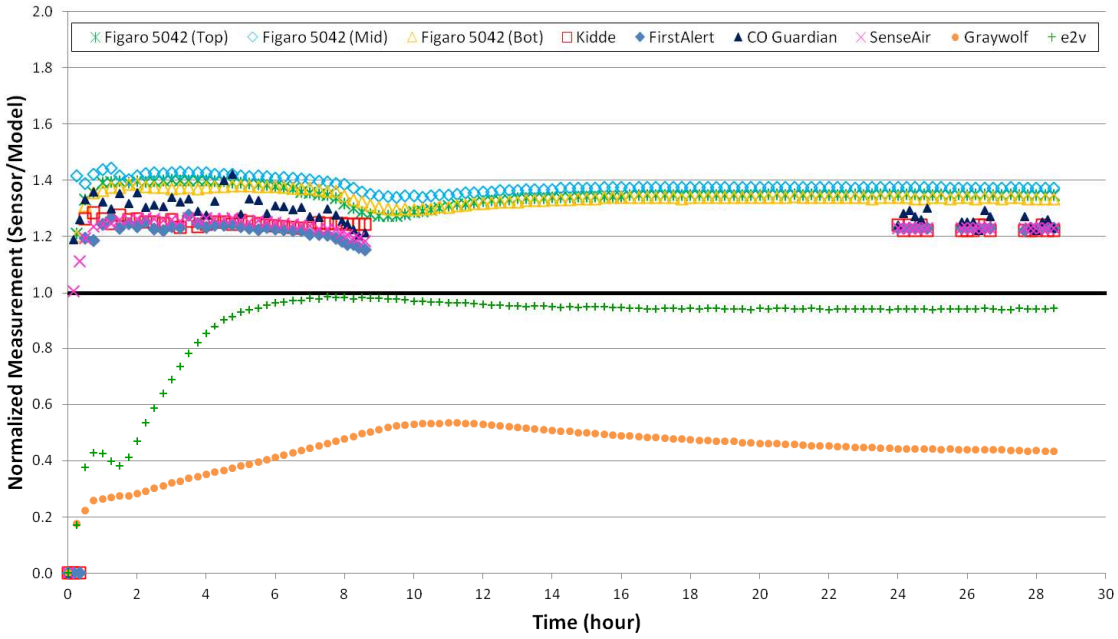

Figure D.3: Sensor measurement normalized to the analytical model versus time for a steady state concentration of 116 mg CO/m^3 at a pressure of 101.3 kPa. The flow rate was reduced from 500 to 50 sccm at t = 7.75 hr to conserve the test gas.

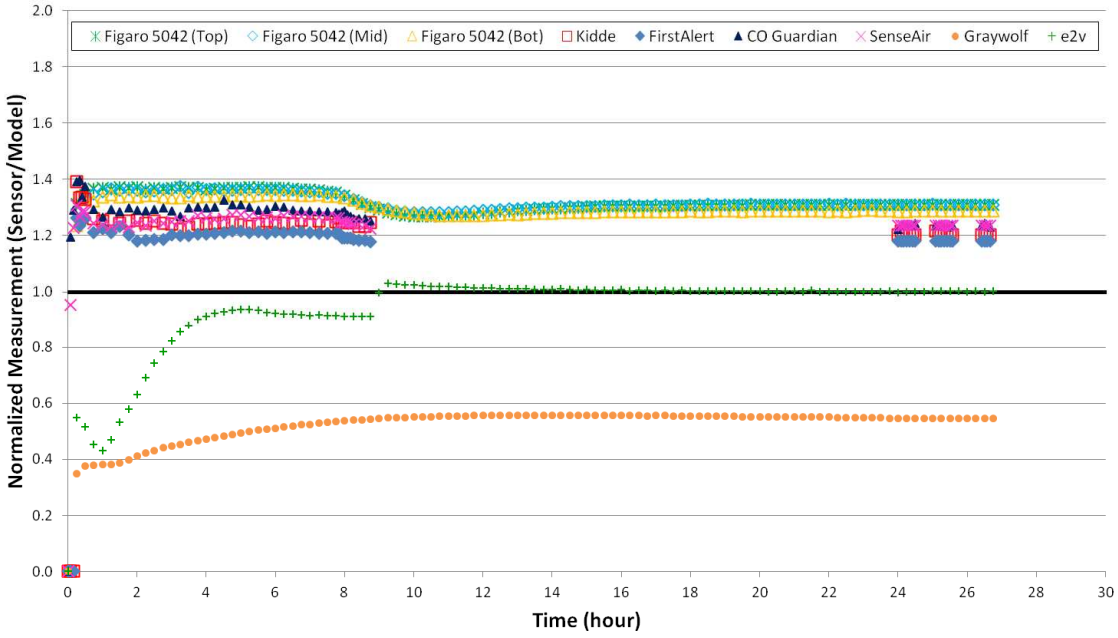

Figure D.4: Sensor measurement normalized to the analytical model versus time for a steady state concentration of 174 mg CO/m^3 at a pressure of 101.3 kPa. The flow rate was reduced from 500 to 50 sccm at t = 7.3 hr to conserve the test gas.

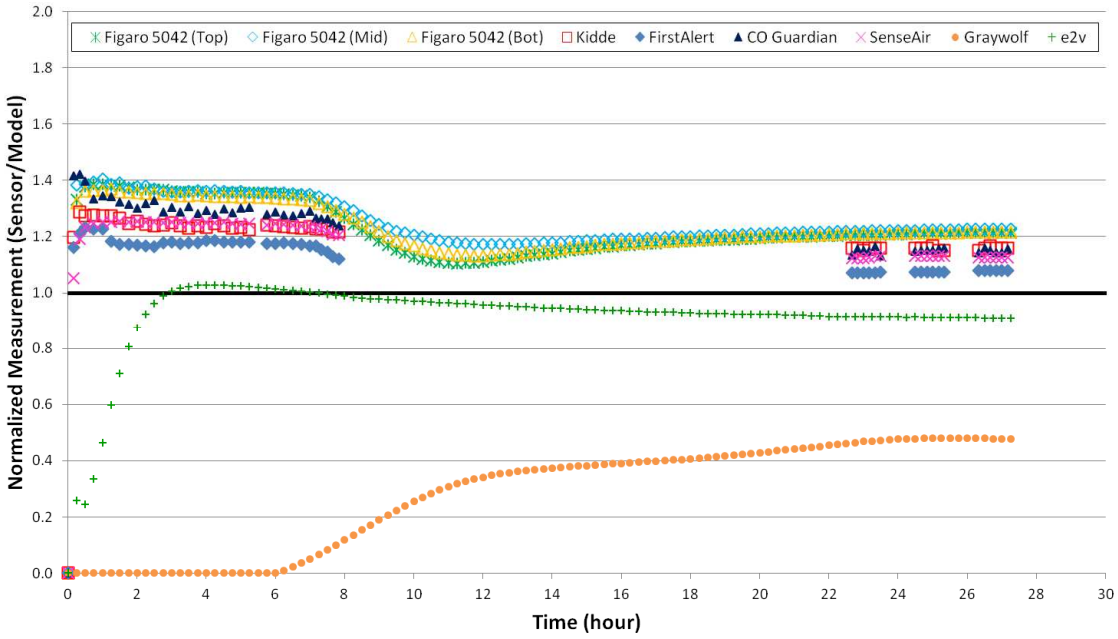

Figure D.5: Sensor measurement normalized to the analytical model versus time for a steady state concentration of 293 mg CO/m^3 at a pressure of 101.3 kPa. The flow rate was reduced from 500 to 50 sccm at t = 7 hr to conserve the test gas.

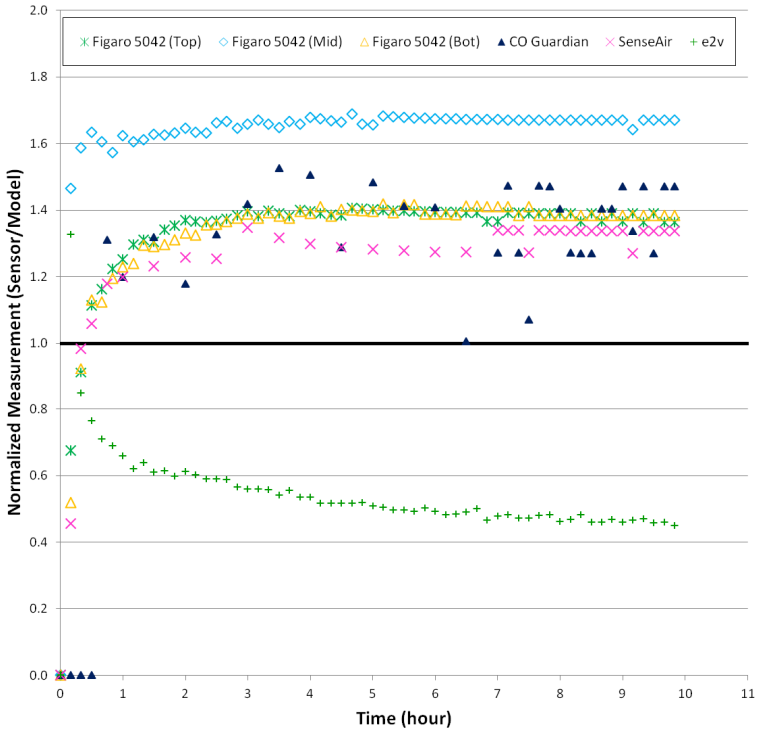

Figure D.6: Sensor measurement normalized to the analytical model versus time for a steady state concentration of 15 mg CO/m^3 at a pressure of 87.5 kPa.

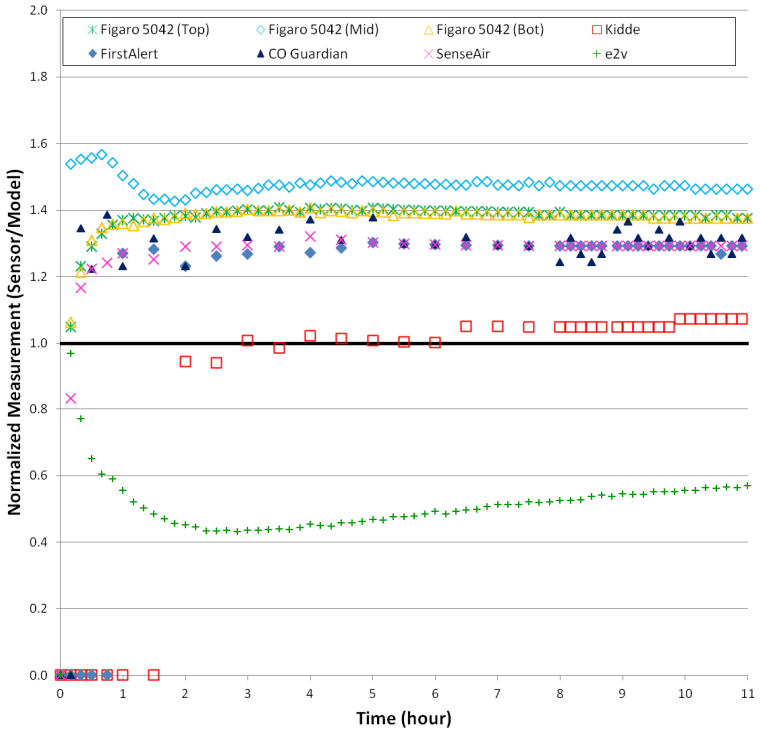

Figure D.7: Sensor measurement normalized to the analytical model versus time for a steady state concentration of 42 mg CO/m^3 at a pressure of 87.5 kPa.

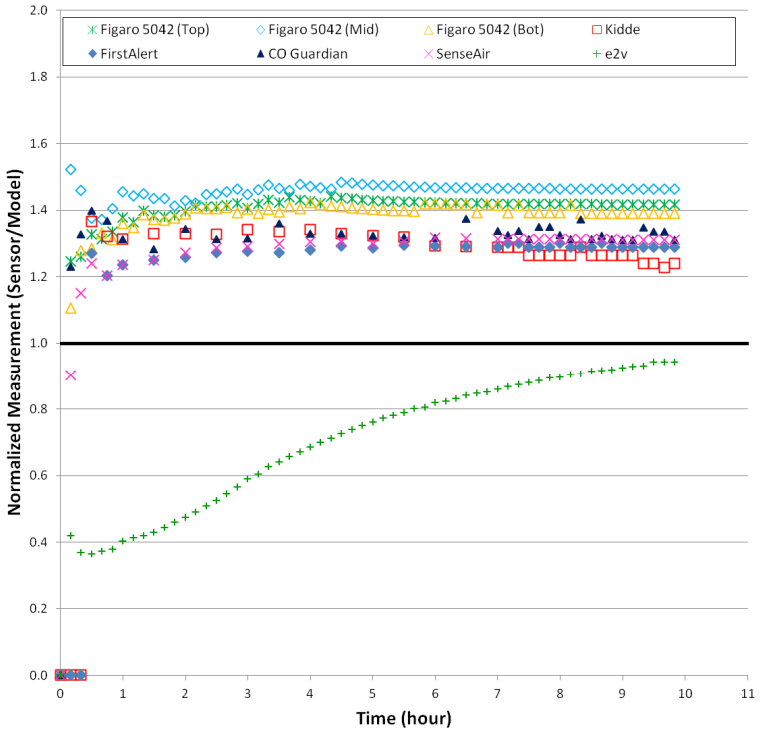

Figure D.8: Sensor measurement normalized to the analytical model versus time for a steady state concentration of 85 mg CO/m^3 at a pressure of 87.5 kPa.

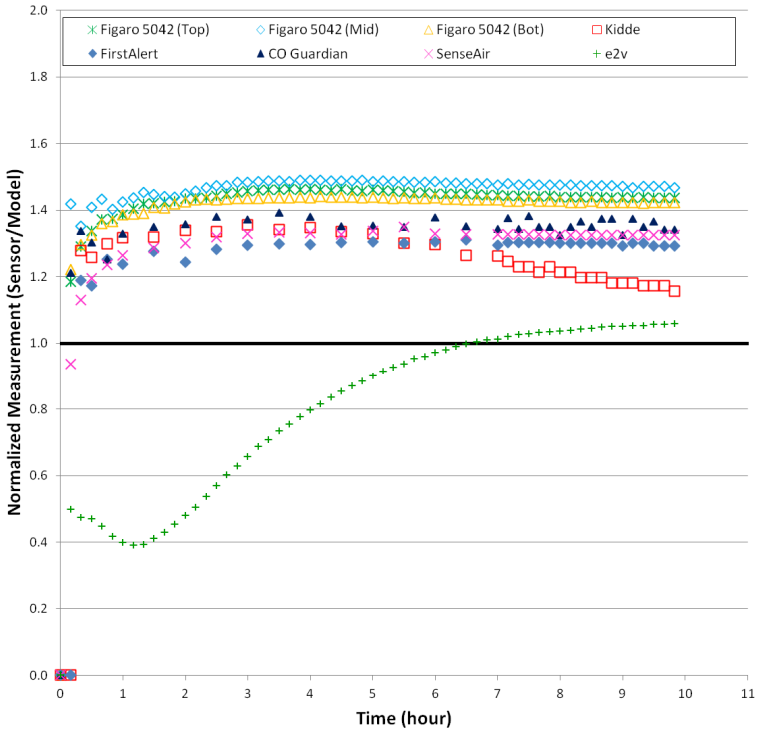

Figure D.9: Sensor measurement normalized to the analytical model versus time for a steady state concentration of 127 mg CO/m^3 at a pressure of 87.5 kPa.

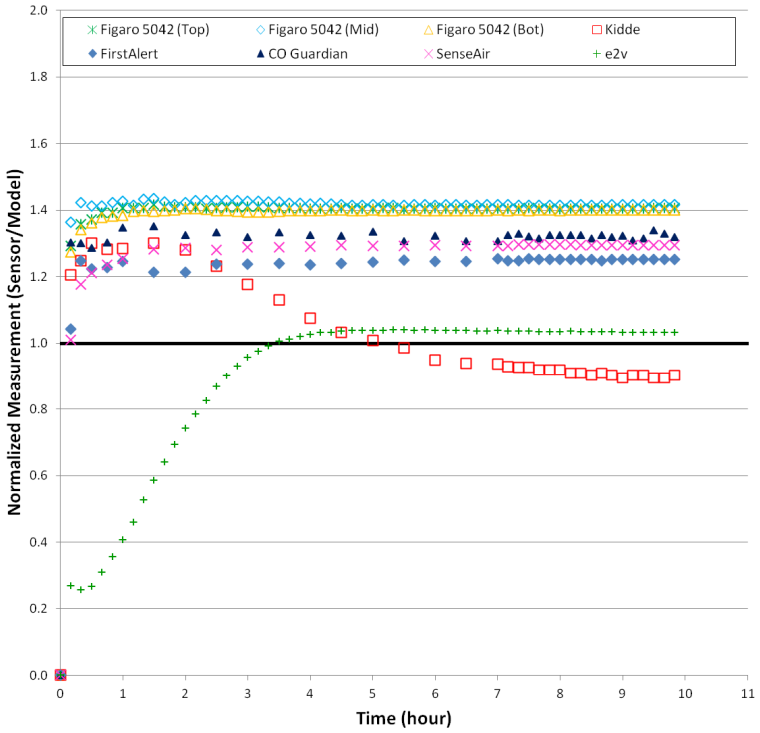

Figure D.10: Sensor measurement normalized to the analytical model versus time for a steady state concentration of 215 mg CO/m^3 at a pressure of 87.5 kPa.

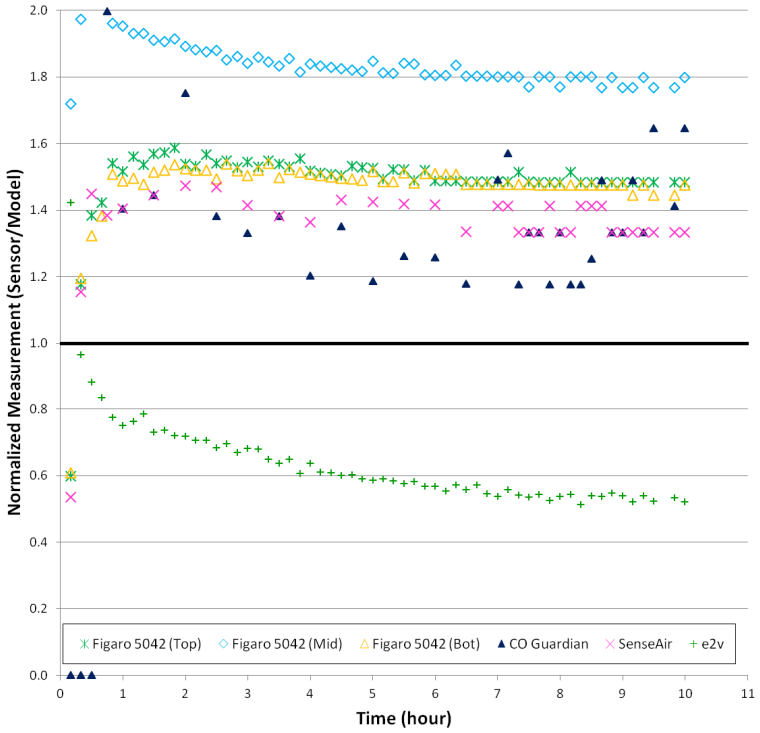

Figure D.11: Sensor measurement normalized to the analytical model versus time for a steady state concentration of 11 mg CO/m^3 at a pressure of 75.3 kPa.

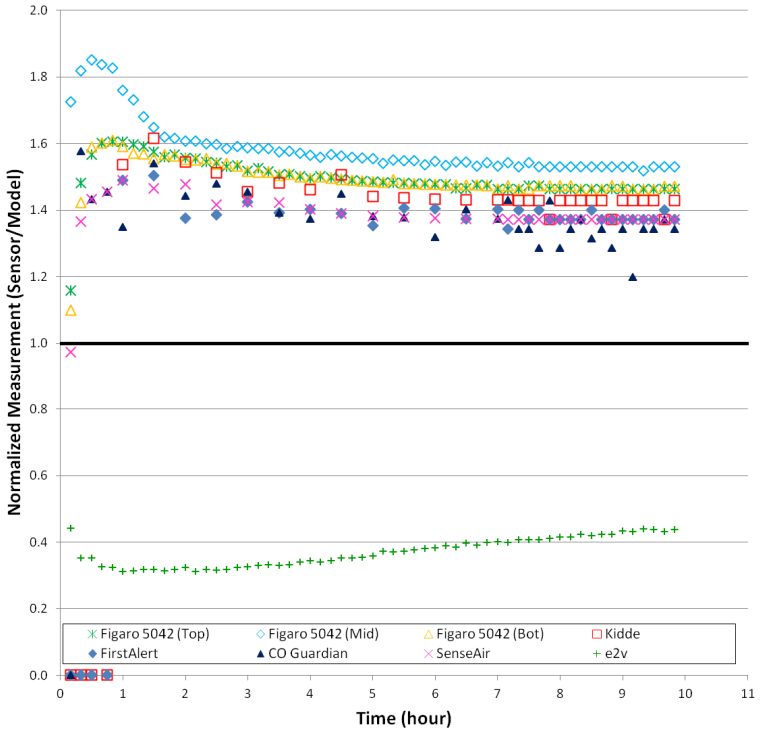

Figure D.12: Sensor measurement normalized to the analytical model versus time for a steady state concentration of 31 mg CO/m^3 at a pressure of 75.3 kPa.

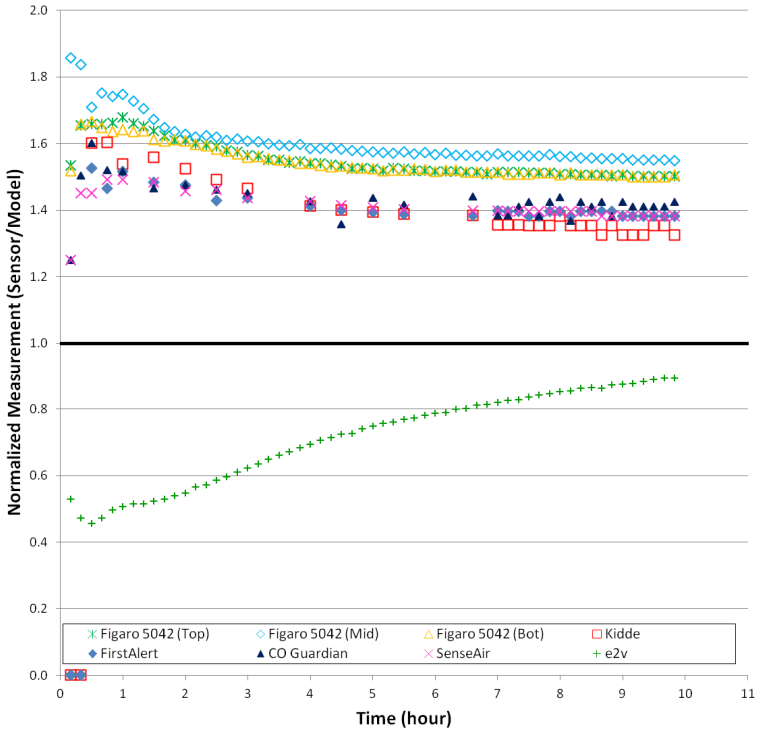

Figure D.13: Sensor measurement normalized to the analytical model versus time for a steady state concentration of 62 mg CO/m^3 at a pressure of 75.3 kPa.

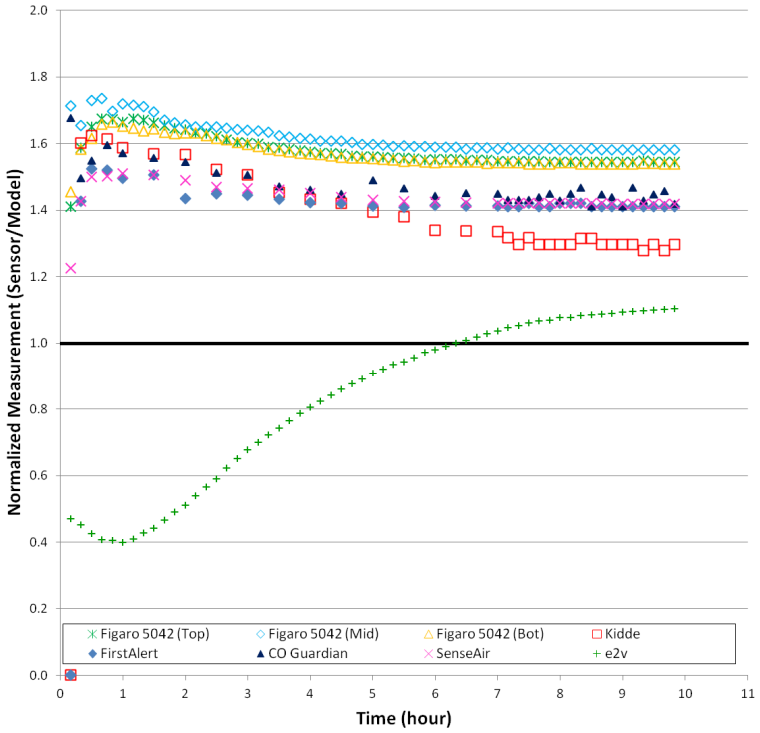

Figure D.14: Sensor measurement normalized to the analytical model versus time for a steady state concentration of 93 mg CO/m^3 at a pressure of 75.3 kPa.

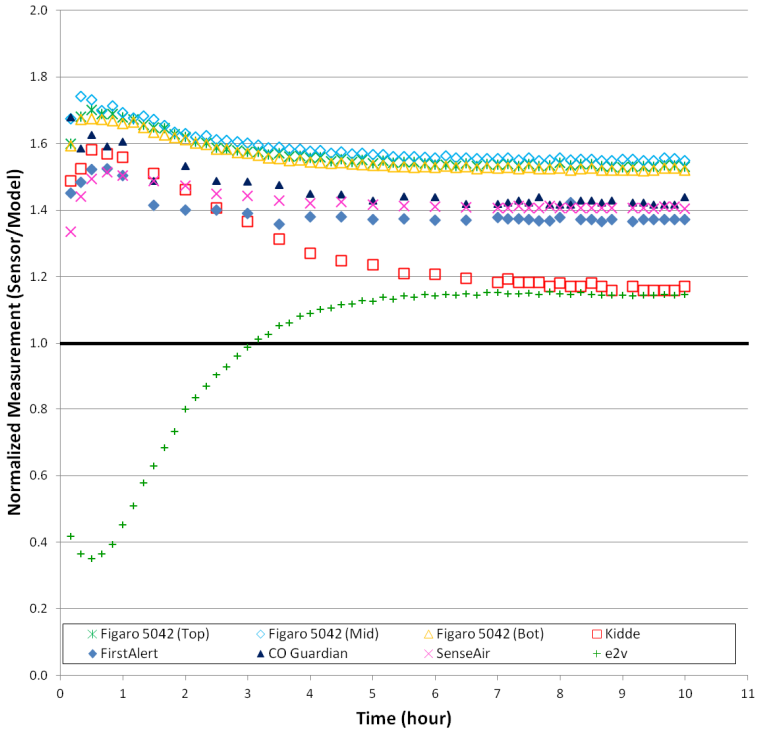

Figure D.15: Sensor measurement normalized to the analytical model versus time for a steady state concentration of 157 mg CO/m^3 at a pressure of 75.3 kPa.